Elsevier Editorial System(tm) for Nuclear Inst. and Methods in Physics Research, A
Manuscript Draft

Manuscript Number: NIMA-D-14-01003R1

Title: The COMPASS Setup for Physics with Hadron Beams

Article Type: Full Length Article

Section/Category: High Energy and Nuclear Physics Detectors

Keywords: fixed target experiment, hadron spectroscopy, silicon microstrip detectors , GEM detector, drift chambers, RICH detector, calorimetry, front-end electronics, data acquisition, data reconstruction,Monte-Carlo simulation

Corresponding Author: Dr. Andrea Bressan, PhD

Corresponding Author's Institution: University of Trieste

First Author: Andrea Bressan, PhD

Order of Authors: Andrea Bressan, PhD

Abstract: The main characteristics of the COMPASS experimental setup for physics with hadron beams are described. This setup was designed to perform exclusive measurements of processes with several charged and/or neutral particles in the final state. Making use of a large part of the apparatus that was previously built for spin structure studies with a muon beam, it also features a new target system as well as new or upgraded detectors. The hadron setup is able to operateat the high incident hadron flux available at CERN. It is characterised by large angular and momentum coverages, large and nearly flat acceptances, and good two and three-particle mass resolutions. In 2008 and 2009 it was successfully used with positive and negative hadron beams and with liquid hydrogen and solid nuclear targets. This article describes the new and upgraded detectors and auxiliary equipment, outlines the reconstruction procedures used, and summarises the general performance of the setup.

The COMPASS Setup for Physics with Hadron Beams

Ph. Abbon[v], C. Adolph[h], R. Akhunzyanov[g], Yu. Alexandrov[o,8], M.G. Alexeev[aa], G.D. Alexeev[g], A. Amoroso[aa,ac], V. Andrieux[v], V. Anosov[g], A. Austregesilo[j,q], B. Badełek[ae], F. Balestra[aa,ac], J. Barth[d], G. Baum[a], R. Beck[c], Y. Bedfer[v], A. Berlin[b], J. Bernhard[m], K. Bicker[j,q], E. R. Bielert[j], J. Bieling[d], R. Birsa[y], J. Bisplinghoff[c], M. Bodlak[s], M. Boer[v], P. Bordalo[l,1], F. Bradamante[x,y], C. Braun[h], A. Bressan[x,y,*], M. Büchele[i], E. Burtin[v], L. Capozza[v], P. Ciliberti[x,y], M. Chiosso[aa,ac], S.U. Chung[q,2], A. Cicuttin[z,y], M. Colantoni[ac], D. Cotte[j], M.L. Crespo[z,y], Q. Curiel[v], T. Dafni[v], S. Dalla Torre[y], S.S. Dasgupta[f], S. Dasgupta[y], O.Yu. Denisov[ac], D. Desforge[v], A.M. Dinkelbach[q], S.V. Donskov[u], N. Doshita[ag], V. Duic[x], W. Dünnweber[p], D. Durand[v], M. Dziewiecki[af], A. Efremov[g], C. Elia[x,y], P.D. Eversheim[c], W. Eyrich[h], M. Faessler[p], A. Ferrero[v], M. Finger[s], M. Finger jr.[s], H. Fischer[i], C. Franco[l], N. du Fresne von Hohenesche[m,j], J.M. Friedrich[q], V. Frolov[j], L. Gatignon[j], F. Gautheron[b], O.P. Gavrichtchouk[g], S. Gerassimov[o,q], R. Geyer[p], A. Giganon[v], I. Gnesi[aa,ac], B. Gobbo[y], S. Goertz[d], M. Gorzellik[i], S. Grabmüller[q], A. Grasso[aa,ac], M. Gregori[y], B. Grube[q], T. Grussenmeyer[i], A. Guskov[g], F. Haas[q], D. von Harrach[m], D. Hahne[d], R. Hashimoto[ag], F.H. Heinsius[i], F. Herrmann[i], F. Hinterberger[c], Ch. Höppner[q], N. Horikawa[r,3], N. d'Hose[v], S. Huber[q], S. Ishimoto[ag,4], A. Ivanov[g], Yu. Ivanshin[g], T. Iwata[ag], R. Jahn[c], V. Jary[t], P. Jasinski[m], P. Jörg[i], R. Joosten[c], E. Kabuß[m], B. Ketzer[q,5], G.V. Khaustov[u], Yu.A. Khokhlov[u,6], Yu. Kisselev[g], F. Klein[d], K. Klimaszewski[ad], J.H. Koivuniemi[b], V.N. Kolosov[u], K. Kondo[ag], K. Königsmann[i], I. Konorov[o,q], V.F. Konstantinov[u], A.M. Kotzinian[aa,ac], O. Kouznetsov[g], M. Krämer[q], Z.V. Kroumchtein[g], N. Kuchinski[g], R. Kuhn[q], F. Kunne[v,**], K. Kurek[ad], R.P. Kurjata[af], A.A. Lednev[u], A. Lehmann[h], M. Levillain[v], S. Levorato[y], J. Lichtenstadt[w], A. Maggiora[ac], A. Magnon[v], N. Makke[x,y], G.K. Mallot[j], C. Marchand[v], J. Marroncle[v], A. Martin[x,y], J. Marzec[af], J. Matousek[s], H. Matsuda[ag], T. Matsuda[n], G. Menon[y], G. Meshcheryakov[g], W. Meyer[b], T. Michigami[ag], Yu.V. Mikhailov[u], Y. Miyachi[ag], M.A. Moinester[w], A. Nagaytsev[g], T. Nagel[q], F. Nerling[m], S. Neubert[q], D. Neyret[v], V.I. Nikolaenko[u], J. Novy[t], W.-D. Nowak[i], A.S. Nunes[l], A.G. Olshevsky[g], I. Orlov[g], M. Ostrick[m], R. Panknin[d], D. Panzieri[ab,ac], B. Parsamyan[aa,ac], S. Paul[q], G. Pesaro[x,y], V. Pesaro[j],

[*]Corresponding author. Tel: +41-22-76-76248
[**]Corresponding author. Tel: +41-22-76-76248
Email addresses: Andrea.Bressan@cern.ch (A. Bressan), Fabienne.Kunne@cern.ch (F. Kunne)
[1]Also at Instituto Superior Técnico, Universidade de Lisboa, Lisbon, Portugal
[2]Also at Department of Physics, Pusan National University, Busan 609-735, Republic of Korea and at Physics Department, Brookhaven National Laboratory, Upton, NY 11973, U.S.A.
[3]Also at Chubu University, Kasugai, Aichi, 487-8501 Japan
[4]Also at KEK, 1-1 Oho, Tsukuba, Ibaraki, 305-0801 Japan
[5]Present address: Universität Bonn, Helmholtz-Institut für Strahlen- und Kernphysik, 53115 Bonn, Germany
[6]Also at Moscow Institute of Physics and Technology, Moscow Region, 141700, Russia
[7]present address: RWTH Aachen University, III. Physikalisches Institut, 52056 Aachen, Germany
[8]deceased

D.V. Peshekhonov[g], C. Pires[l], S. Platchkov[v], J. Pochodzalla[m], V.A. Polyakov[u], J. Pretz[d,7], M. Quaresma[l], C. Quintans[l], S. Ramos[l,1], C. Regali[i], G. Reicherz[b], J-M. Reymond[v], E. Rocco[j], N.S. Rossiyskaya[g], J.-Y. Rousse[v], D.I. Ryabchikov[u], A. Rychter[af], A. Samartsev[g], V.D. Samoylenko[u], A. Sandacz[ad], S. Sarkar[f], I.A. Savin[g], G. Sbrizzai[x,y], P. Schiavon[x,y], C. Schill[i], T. Schlüter[p], K. Schmidt[i], H. Schmieden[d], K. Schönning[j], S. Schopferer[i], M. Schott[j], O.Yu. Shevchenko[g,8], L. Silva[l], L. Sinha[f], S. Sirtl[i], M. Slunecka[g], S. Sosio[aa,ac], F. Sozzi[y], A. Srnka[e], L. Steiger[y], M. Stolarski[l], M. Sulc[k], R. Sulej[ad], H. Suzuki[ag,3], A. Szabelski[ad], T. Szameitat[i], P. Sznajder[ad], S. Takekawa[aa,ac], G. Terça[l], J. ter Wolbeek[i], S. Tessaro[y], F. Tessarotto[y], F. Thibaud[v], V. Tskhay[o], S. Uhl[q], I. Uman[p], M. Virius[t], L. Wang[b], T. Weisrock[m], Q. Weitzel[q], M. Wilfert[m], R. Windmolders[d], H. Wollny[v], K. Zaremba[af], M. Zavertyaev[o], E. Zemlyanichkina[g], M. Ziembicki[af], A. Zink[h]

[a] *Universität Bielefeld, Fakultät für Physik, 33501 Bielefeld, Germany*
[b] *Universität Bochum, Institut für Experimentalphysik, 44780 Bochum, Germany*
[c] *Universität Bonn, Helmholtz-Institut für Strahlen- und Kernphysik, 53115 Bonn, Germany*
[d] *Universität Bonn, Physikalisches Institut, 53115 Bonn, Germany*
[e] *Institute of Scientific Instruments, AS CR, 61264 Brno, Czech Republic*
[f] *Matrivani Institute of Experimental Research & Education, Calcutta-700 030, India*
[g] *Joint Institute for Nuclear Research, 141980 Dubna, Moscow region, Russia*
[h] *Universität Erlangen–Nürnberg, Physikalisches Institut, 91054 Erlangen, Germany*
[i] *Universität Freiburg, Physikalisches Institut, 79104 Freiburg, Germany*
[j] *CERN, 1211 Geneva 23, Switzerland*
[k] *Technical University in Liberec, 46117 Liberec, Czech Republic*
[l] *LIP, 1000-149 Lisbon, Portugal*
[m] *Universität Mainz, Institut für Kernphysik, 55099 Mainz, Germany*
[n] *University of Miyazaki, Miyazaki 889-2192, Japan*
[o] *Lebedev Physical Institute, 119991 Moscow, Russia*
[p] *Ludwig-Maximilians-Universität München, Department für Physik, 80799 Munich, Germany*
[q] *Technische Universität München, Physik Department, 85748 Garching, Germany*
[r] *Nagoya University, 464 Nagoya, Japan*
[s] *Charles University in Prague, Faculty of Mathematics and Physics, 18000 Prague, Czech Republic*
[t] *Czech Technical University in Prague, 16636 Prague, Czech Republic*
[u] *State Scientific Center Institute for High Energy Physics of National Research Center 'Kurchatov Institute', 142281 Protvino, Russia*
[v] *CEA IRFU/SPhN Saclay, 91191 Gif-sur-Yvette, France*
[w] *Tel Aviv University, School of Physics and Astronomy, 69978 Tel Aviv, Israel*
[x] *University of Trieste, Department of Physics, 34127 Trieste, Italy*
[y] *Trieste Section of INFN, 34127 Trieste, Italy*
[z] *Abdus Salam ICTP, 34151 Trieste, Italy*
[aa] *University of Turin, Department of Physics, 10125 Turin, Italy*
[ab] *University of Eastern Piedmont, 15100 Alessandria, Italy*
[ac] *Torino Section of INFN, 10125 Turin, Italy*
[ad] *National Centre for Nuclear Research, 00-681 Warsaw, Poland*
[ae] *University of Warsaw, Faculty of Physics, 00-681 Warsaw, Poland*
[af] *Warsaw University of Technology, Institute of Radioelectronics, 00-665 Warsaw, Poland*
[ag] *Yamagata University, Yamagata, 992-8510 Japan*

Abstract

The main characteristics of the COMPASS experimental setup for physics with hadron beams are described. This setup was designed to perform exclusive measurements of processes with several charged and/or neutral particles in the final state. Making use of a large part of the apparatus that was previously built for spin structure studies with a muon beam, it also features a new target system as well as new or upgraded detectors. The hadron setup is able to operate at the high incident hadron flux available at CERN. It is characterised by large angular and momentum coverages, large and nearly flat acceptances, and good two and three-particle mass resolutions. In 2008 and 2009 it was successfully used with positive and negative hadron beams and with liquid hydrogen and solid nuclear targets. This article describes the new and upgraded detectors and auxiliary equipment, outlines the reconstruction procedures used, and summarises the general performance of the setup.

Keywords: fixed target experiment, hadron spectroscopy, silicon microstrip detectors, GEM detector, drift chambers, RICH detector, calorimetry, front-end electronics, data acquisition, data reconstruction, Monte-Carlo simulation
PACS 13.85.-t, 07.05.Fb, 07.05.Hd, 07.05.Kf, 29.25.Pj, 29.30.-h, 29.40.Cs, 29.40.Gx, 29.40.Ka, 29.40.Mc, 29.40.Vj, 29.40.Wk, 29.27.Fh, 29.85.Ca

---

Contents

1. Introduction

The goal of the COMPASS experiment at CERN is a better understanding of the structure and dynamics of hadrons. At the relevant length scales of $\sim 10^{-15}\,\mathrm{m}$ the strong coupling constant α_s approaches unity, which is the domain of non-perturbative Quantum Chromodynamics (QCD). Using a $160-200\,\mathrm{GeV}/c$ muon beam, COMPASS studies the nucleon spin structure by deep inelastic scattering off a polarised ^{6}LiD or NH_3 target [1]. Experiments with hadron beams of $190\,\mathrm{GeV}/c$, which started in 2008, aim at precision spectroscopy of light mesons and baryons with masses up to $3\,\mathrm{GeV}/c^2$, the identification and systematic study of possible exotic configurations with gluonic degrees of freedom or multi-quark systems, as well as the study of processes governed by chiral dynamics and tests of predictions of chiral perturbation theory.

These experiments require a state-of-the-art spectrometer with high acceptance and high resolution for charged and neutral particles in order to perform exclusive measurements of multi-particle final states over a wide kinematic range. Three different mechanisms contribute to the production of a system X, as shown in Fig. 1: diffractive dissociation and central production, which can be described to proceed via the exchange of one or two Reggeons $\mathbb{R}$, respectively, between beam hadron and target nucleus N, and photo-production in the Coulomb field of a nucleus at very low values of momentum transfer. In all these processes the final-state particles are emitted mostly in forward direction, which requires an excellent angular resolution of the spectrometer very close to and even within the beam envelope. For the interpretation of the data using partial-wave analysis (PWA) tools, a large and uniform acceptance over the whole kinematic domain under study is mandatory.

The relative contributions of the above-mentioned processes to a data sample can be varied by applying different trigger conditions and by adjusting kinematic selection criteria in the analysis. At intermediate-to-large values of momentum transfer, the cross section for reactions mediated by Pomerons, i.e. Reggeons with vacuum quantum numbers, is large, of the order of $1-2\,\mathrm{mb}$. The contribution of individual partial waves, however, may be several orders of magnitude smaller, thus requiring the collection of large data sets. Of particular interest are states X that do not fit into the naive constituent quark model but are allowed by QCD, like glueballs or hybrids which carry gluonic degrees of freedom, or multi-quark systems. States with gluonic degrees of freedom are generally believed to be enhanced in reactions in which Pomerons are exchanged. A small but significant contribution of a spin-exotic partial wave with non-

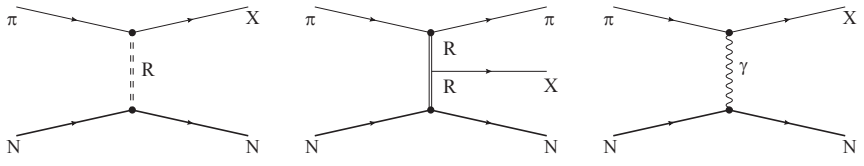

Figure 1: Production mechanisms employed in COMPASS for (left) diffractive dissociation, (middle) central production, (right) photo-production by quasi-real photons γ, with π denoting the beam particle (can be also p, K), and N the target nucleon or nucleus.

$q\overline{q}'$ quantum numbers $J^{PC} = 1^{-+}$, consistent with the $\pi_1(1600)$, was confirmed by COMPASS using data taken in 2004 [2]. However, an unambiguous understanding of the underlying structure of this and many other light-hadron states requires experiments with higher statistical accuracy, employing different production mechanisms and observation of the same system X in different decay channels. At very small values of momentum transfer, the cross section is dominated by Primakoff reactions, i.e. Coulomb scattering of pions or kaons off quasi-real photons emitted from a nuclear target. The dynamics of the scattering of a beam π into $\pi\gamma$, $\pi^-\pi^0$, 3π, etc., at low-energy, i.e. from threshold up to a few pion masses, is predicted by chiral perturbation theory (ChPT). COMPASS can thus scrutinise ChPT predictions of chiral dynamics [3] and of fundamental low-energy parameters such as the polarisabilities of mesons.

Compared to previous experiments, the main advantages of the COMPASS setup are the possibility to study reactions with different projectiles in high-intensity beams with up to $10^7\,\mathrm{part./s}$ and to reconstruct final states containing both neutral and charged particles. Different charges and types of beam particles, e.g. $\pi^\pm$, $\mathrm{K}^\pm$, and (anti)protons, can be selected by tuning the COMPASS beam line and by tagging them with differential Cherenkov counters. The possibility to switch between pion and muon beams of the same momentum is a unique asset for the measurement of pion polarisabilities at COMPASS, where the systematic error of the measurement can be significantly reduced through regular reference measurements with incident muons, i.e. point-like particles. As target material either liquid hydrogen or various solid-state nuclear targets are used. A recoil proton detector (RPD) is installed around the target to ensure the exclusivity of the final state. A set of double-sided silicon microstrip detectors positioned upstream and downstream of the target is used to reconstruct the interaction vertex and the angles of the outgoing particles. Here, the required angular resolution is dictated by Primakoff reactions, where pions or muons scattered by angles of a few hundred $\mu\mathrm{rad}$ have to be detected. A high momentum resolution for charged particles is provided by a two-stage magnetic spectrometer. For the tracking in the beam region new pixelised Gas Electron Multiplier (GEM) detectors with a minimised material budget along the beam were built, in replacement of the thicker scintillating fibre detectors. For the tracking at small angles, the existing Micromegas trackers were adapted to the hadron beam conditions. A major upgrade of the Ring-Imaging Cherenkov (RICH) counter was carried out, which largely improved the performance of particle identification at high rates. Photons are detected in two electromagnetic calorimeters, which have been optimised for stability and uniformity in order to achieve good resolution. Several new trigger elements were built and implemented into the trigger system.

The present paper describes the modifications and upgrades of the experimental setup required for the hadron programme of COMPASS. Some of these upgrades were already realised for the nucleon spin programme after 2005. After a brief overview of the layout of the spectrometer in Section 2, the beam line and associated detectors are described in Section 3 and the target region in Section 4. The newly installed tracking detectors are discussed in Section 5. Section 6 deals with the systems used for particle identification, namely the RICH counter and the two electromagnetic calorimeters. The various trigger systems are explained in Section 7 and the data acquisition in Section 8. The algorithms for event reconstruction and the performance of individual detector components are summarised in Section 9, while the global spectrometer performance

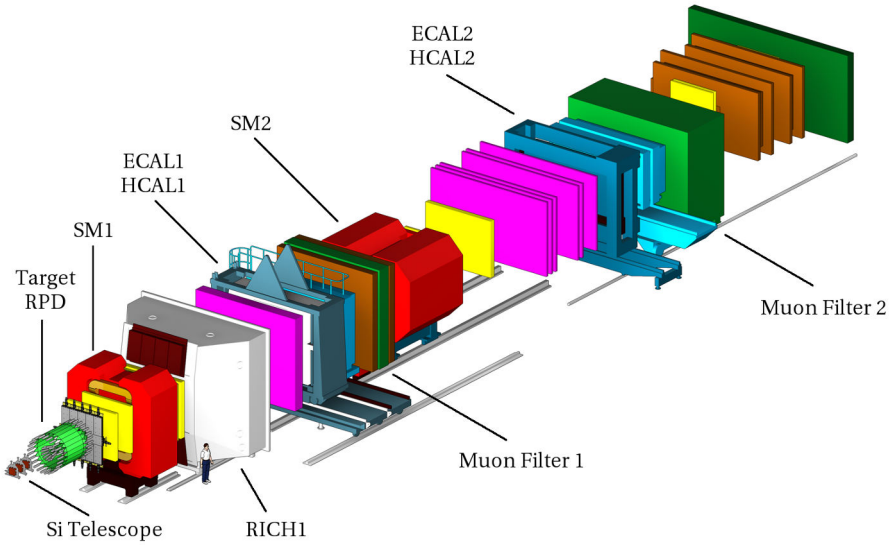

Figure 2: Three-dimensional view of the COMPASS setup for measurements with hadron beams. The beam comes from the left side. The upstream part of the setup (beam line) is not shown here. The different colours indicate different detector types.

and Monte Carlo simulations of the apparatus are discussed in Section 10.

Throughout this paper, the following kinematic variables will be used: the squared four-momentum transfer from the incident beam particle to the recoiling target nucleus $t = (p_{\mathrm{beam}} - p_X)^2$; the reduced squared 4-momentum transfer $t' = |t| - |t|_{\mathrm{min}}$ to the recoiling target nucleon beyond the kinematic minimum $|t|_{\mathrm{min}}$; the Gottfried-Jackson angle θ_{GJ}, defined as the polar angle of the three-momentum of the isobar (i.e. di-pion) from the decay of X, and the corresponding azimuthal Treiman-Young angle ϕ_{TY}. These two angles are calculated in the centre-of-momentum frame of X with the z-axis along the beam direction and the y-axis perpendicular to the production plane, formed by the momentum vectors of target and recoil particles.

2. Layout of the Spectrometer

The main features of the COMPASS experimental setup and most of the detectors as used until 2004 are described in Ref. [1]. In this section a short overview of the apparatus is given, with particular emphasis on detectors that are either specific to the data taking with hadron beams in 2008 and 2009, or were added to the setup after 2005 to be used in both muon and hadron programmes.

The COMPASS setup can be divided into four parts along the beam, starting with the beam line section and the detectors that identify the incoming beam particles. It is followed by the target region, which is specific for each of the COMPASS physics

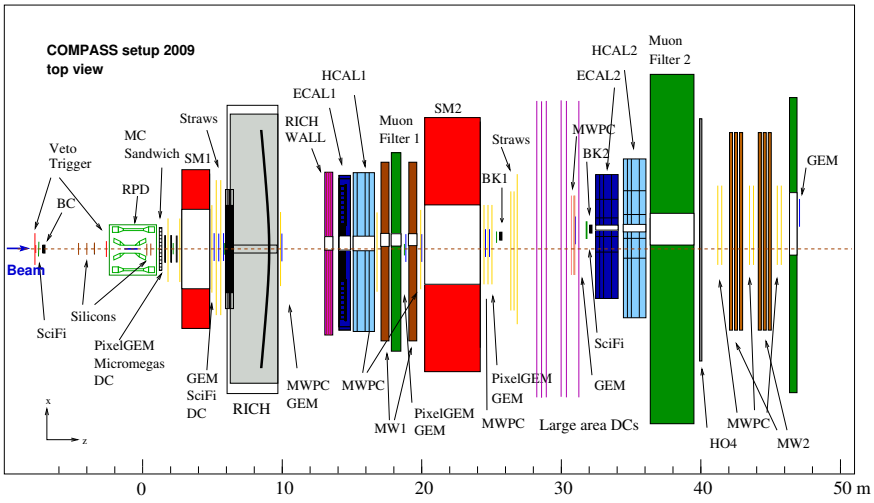

Figure 3: Top view of the COMPASS setup for data taking with hadron beams. The labels indicate the various detectors, as referenced throughout this paper. The vertical scale is only indicative of the relative detector sizes. The colour code follows that of Fig. 2.

programmes. It comprises the target and the detectors located in its near vicinity. The third part, called Large Angle Spectrometer (LAS) includes the first dipole magnet, SM1, the tracking detectors around it, and the RICH-1 counter. The fourth part, called Small Angle Spectrometer (SAS), occupies the downstream part of the setup. It is built around the SM2 dipole magnet and includes several tracking detectors. Both LAS and SAS comprise a pair of electromagnetic and hadron calorimeters, and a muon filter. Figures 2 and 3 show the three-dimensional and top views of the COMPASS setup, respectively.

2.1. Beam line

The COMPASS setup is located at the end of the M2 beam line of the CERN SPS accelerator. The M2 beam line can be tuned for beams of different particles, including secondary hadron beams and tertiary muon or electron beams. Hadron and muon beams can be either of negative or positive charge. Switching between beams takes typically thirty minutes.

During data taking with hadron beams only the trajectory of the incident beam particle is measured. The Beam Momentum Station (BMS), which is used for the determination of the incident momentum during measurements with a muon beam, is moved out of the beam in order to minimise the material budget along the beam path. However, the muon beam is also used during Primakoff measurements in order to complement the data taken with pions. The BMS is then moved back into the beam line. Downstream of the BMS location, two differential Cherenkov counters identify the hadrons (pions, kaons, or protons) that are present in the hadron beam.

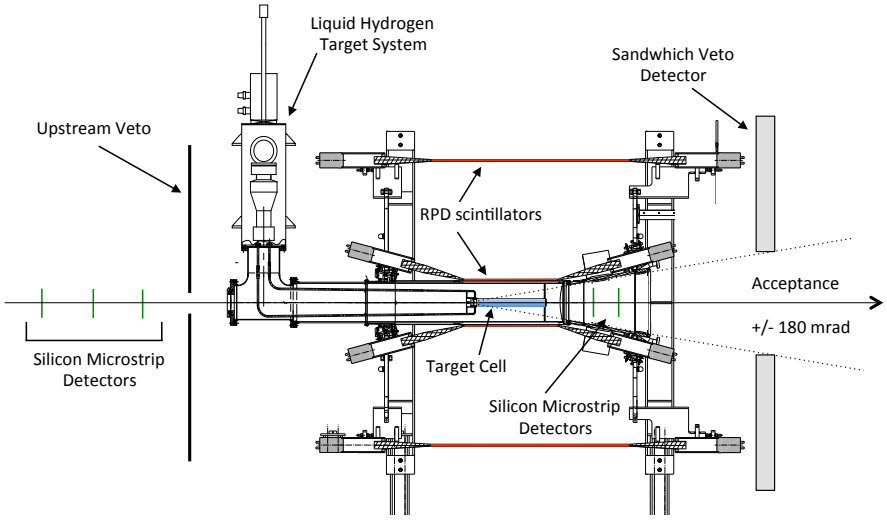

Figure 4: Side view of the target region with the liquid hydrogen target system.

2.2. Target region

Most of the data with hadron beams were collected using a liquid hydrogen target. The target region comprises the target itself and the detectors around it (Fig. 4). The target is surrounded by a time-of-flight detector that is called Recoil Proton Detector (RPD). Measuring the recoil protons from the target, this detector ensures the exclusivity of the processes under investigation. The RPD covers the momentum transfer range down to $|t| = 0.07\,\mathrm{GeV}^2/c^2$. Three silicon stations operating at a temperature of 200 K are mounted upstream of the target. Together with a scintillating fibre counter, these detectors determine the trajectory of the beam particle before it enters the target. Two other silicon stations are located immediately downstream of the target, inside the RPD. A scintillator/iron sampling detector, called Sandwich Veto, is installed downstream of the RPD. Used as part of the trigger, this detector vetoes particles detected outside of the LAS acceptance. A dedicated Multiplicity Counter (MC) is positioned downstream of the RPD, behind the Sandwich Veto. This counter, which measures the number of charged particles in the final state, extends the momentum transfer range towards values smaller than $|t| = 0.07\,\mathrm{GeV}^2/c^2$.

The liquid hydrogen target can be easily removed and replaced with a specially designed solid-target holder. Up to 16 solid targets with different atomic numbers and different thicknesses can be mounted on the holder and used simultaneously during data taking.

2.3. Large angle spectrometer

The large angle spectrometer includes the detectors located both upstream and downstream of the SM1 magnet. The LAS tracking detectors measure scattered particles with polar angles of up to 180 mrad. In the region near the beam, a PixelGEM detector with low material budget was installed in replacement of the thicker scintillating fibre counter (SciFi) previously used with the muon beam. The design of the Micromegas detectors that are located upstream of SM1 was modified in order to minimise their discharge rate in the hadron beam. A new large-size drift chamber, DC4, is installed downstream of the SM1 magnet, in order to improve the resolution of the tracking at large angles. A major upgrade of the RICH-1 counter was accomplished [4], which considerably improves its performance. The central region of RICH-1 was instrumented with multi-anode photomultipliers, in replacement of the previously used CsI photodetectors. A new analog readout with a reduced dead time was implemented in its peripheral region. The tracking downstream of RICH-1 was supplemented with an additional drift-tube detector, called Rich Wall (RW). A new electromagnetic calorimeter, ECAL1, was added to the LAS setup. ECAL1 extends the coverage of ECAL2 for detection of photons and electrons to larger angles. Its position was chosen with the aim of achieving a continuous angular coverage for both ECAL1 and ECAL2. Installed since 2006, DC4, ECAL1, RICH-1 and RW are part of the apparatus that is common to both hadron and muon physics programmes.

2.4. Small angle spectrometer

The SAS detectors are essentially identical to the detectors used during the data taking with muon beam [1]. In order to minimize the material budget along the beam path, two new PixelGEM detectors replace two SciFi counters. In ECAL2, the innermost lead glass blocks were replaced with radiation-hard Shashlik-type lead/scintillator modules of the same transverse size. In order to maximise the photon detection acceptance near the beam, the size of the ECAL2 central hole was reduced. The central hole of the hadron calorimeter HCAL2, located immediately behind ECAL2, was reduced accordingly.

2.5. Trigger

The trigger system for hadron beam was designed to select the processes listed in Section 1. Several new trigger counters were built and combined with those already available [1]. A beam counter (BC) was installed upstream of the target, as a part of the beam-definition trigger. Both RPD and ECAL2 detectors were included in the trigger. The information from the RPD is used to identify diffractive scattering events. High energy photons, particularly important for the Primakoff reaction, are selected by the central part of ECAL2. Triggering in the region of the lowest momentum transfer values is provided by a new Multiplicity Counter (MC). The existing veto system was extended to veto non-interacting beam particles by adding two beam-killer (BK1 and BK2) scintillator counters along the beam path.

With the nominal hadron beam intensity the trigger rate reaches values of up to $30\,\mathrm{kHz}$. The corresponding data flow is as high as $350\,\mathrm{MB/s}$. The COMPASS data acquisition system was upgraded to meet these conditions.

3. Beam Line

The CERN SPS M2 beam was originally built as a high-energy, high-intensity muon beam. For the COMPASS experiment, the beam line was partly rebuilt to include a high-intensity hadron beam option as well as the possibility to use low-intensity electron beams. For beam particle identification, two CEDARs were added just before the COMPASS spectrometer. Modifications relevant to the muon mode of operation were described in [1]. In this section, the hadron and electron beam modes of operation are summarised. In addition, the detectors used for the identification of the particles in the hadron beam are described.

3.1. Hadron beams

In order to produce a secondary hadron or tertiary muon beam, $400\,\mathrm{GeV}/c$ protons from the CERN SPS are slowly extracted onto a primary production target (T6). These protons arrive during a time period of $9.6\,\mathrm{s}$ once every $30\,\mathrm{s}$ to $48\,\mathrm{s}$, depending on other users of the SPS. The primary target station allows the selection of five positions, an empty target or one out of four Be targets, $80\,\mathrm{mm}$ wide, 2 to $3\,\mathrm{mm}$ high and 40, 100 or $500\,\mathrm{mm}$ thick. Measurements with hadron beams used a nominal intensity of $5 \cdot 10^6\,\mathrm{s}^{-1}$, which e.g. for a negative beam of $190\,\mathrm{GeV}/c$ central momentum is achieved by using $9 \cdot 10^{12}$ protons/cycle on T6 and the $500\,\mathrm{mm}$ target.

The M2 beam line (Fig. 5) starts with a series of six high-gradient quadrupoles (Q1–Q6) for maximum acceptance and a set of three dipoles (BEND 1). The highest-acceptance optical mode works only up to 225 GeV/c due to limited quadrupole gradients.[9] The beam optics is optimised to achieve highest possible momentum resolution.

A pair of massive collimators, which allows a first momentum selection of the beam particles or is also used to dump the beam in case of access to the experiment (TAX 1,2), is located downstream of the first dipoles (BEND 1). The particles passing through theses collimators are transported to an about $430\,\mathrm{m}$ long array of alternately focusing and defocusing (FODO) quadrupoles (Q12–Q18). Before entering the FODO array, two pairs of horizontal (H1, H3) and vertical (V2, V4) collimators define the angular and momentum acceptances of the beam. At the end of the FODO section, the beam is focused into a set of four vertical dipoles (BEND 4,5). The Be absorbers (ABS), which are used in the muon beam operation, are moved out in the hadron mode. After these dipoles, the beam is transported into a second $250\,\mathrm{m}$ long FODO channel (Q22–Q30) that contains a second momentum-defining collimator. The beam is then bent horizontally (BEND 6) and parallelised at the location of the two CEDARs (for more details, see Section 3.3), while restricting the momentum spread to below 1%. Behind the CEDARs, the beam is focused (Q34–Q36) onto the entrance of the electromagnetic calorimeter in the second spectrometer stage, which is located $33\,\mathrm{m}$ downstream of the target. The main beam characteristics are listed in Table 1.

Negative beams are mainly composed of pions, while for momenta larger than $150\,\mathrm{GeV}/c$ the positive beam have a dominant proton component. In both cases, kaons

[9] A different optical mode is available for higher momenta, but the angular acceptance of that mode is about 40% lower.

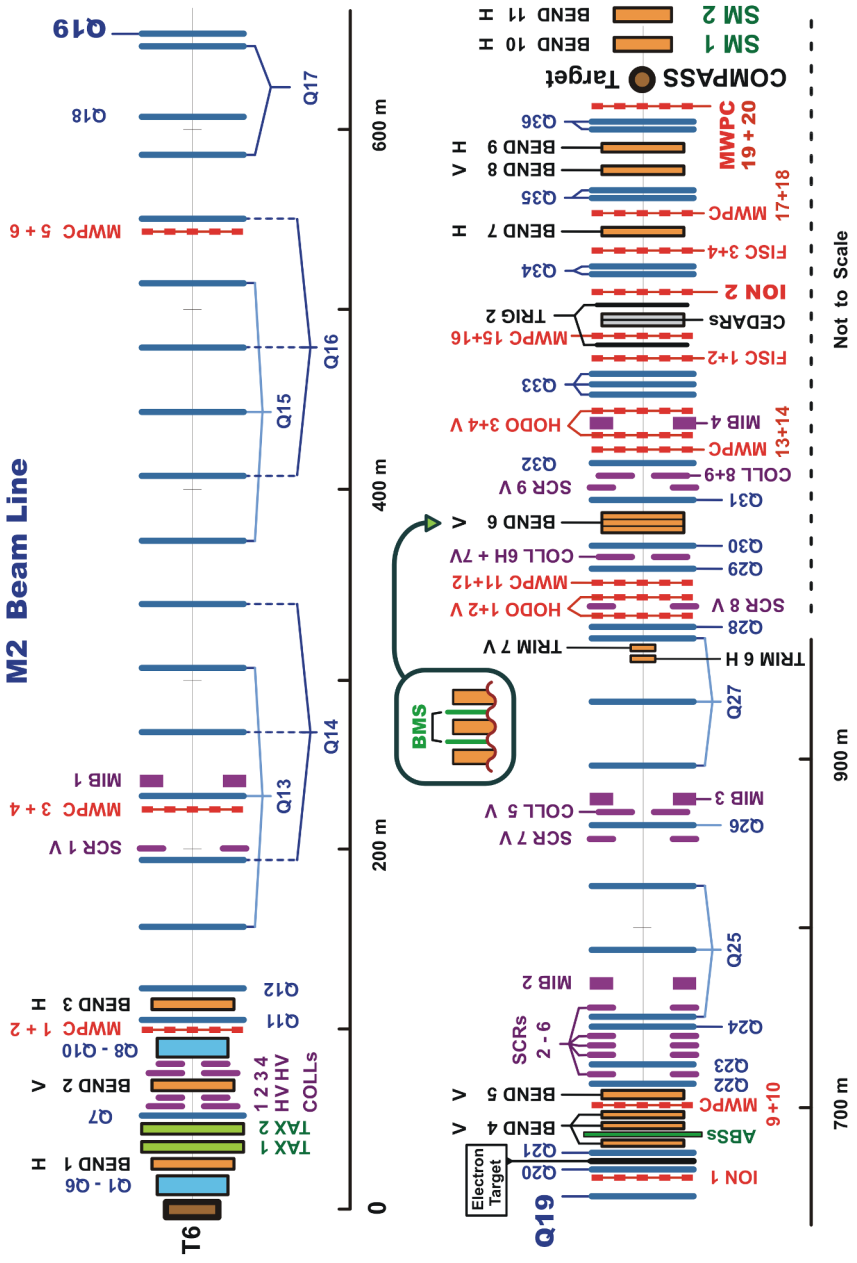

Figure 5: The CERN M2 beam line.

Table 1: The main parameters of the M2 hadron beam.

Parameter	**Value**
Length of beam line from primary target to COMPASS target	$1131.8\,\mathrm{m}$
Maximum beam momentum (high-energy mode)	$280\,\mathrm{GeV}/c$
Maximum beam momentum (normal mode)	$225\,\mathrm{GeV}/c$
Angular acceptance: Horizontal	$\pm 1.0\,\mathrm{mrad}$
Angular acceptance: Vertical	$\pm 2.5\,\mathrm{mrad}$
Angular acceptance: Solid angle	$7.8\,\mu\mathrm{sr}$
Momentum acceptance	$\pm 8\%$
Momentum resolution	1%
Spot size at COMPASS target ($\sigma_x \times \sigma_y$)	$7 \times 8\,\mathrm{mm}^2$
Divergence at COMPASS target ($\sigma_x \times \sigma_y$)	$80\,\mu\mathrm{rad} \times 200\,\mu\mathrm{rad}$

Table 2: The relative composition of the hadron beam at the COMPASS target for some typical momenta. It does not include the $e^{\pm}$ component, which is still present at 100 GeV/c but rapidly decreasing at higher momenta due to synchrotron radiation. The composition values are calculated from measured values [5] and their relative uncertainties amount to 1% for pions and proton, and 2–3% for kaons and antiprotons.

Momentum	Positive beams			Negative beams		
(GeV/c)	π^+	K^+	p	π^-	K^-	$\bar{p}$
100	0.618	0.015	0.367	0.958	0.018	0.024
160	0.360	0.017	0.623	0.966	0.023	0.011
190	0.240	0.014	0.746	0.968	0.024	0.008
200	0.205	0.012	0.783	0.969	0.024	0.007

and electrons may be present at a level of a few percent, depending on the energy chosen. The particle composition of the hadron component of the beam is given in Table 2 for a few typical beam momenta.

3.2. Electron beam

A tertiary electron beam can be produced on demand. For this purpose, a $5\,\mathrm{mm}$ thick lead plate (also called "electron target") equivalent to 90% of a radiation length is moved into the beam line at the end of the first FODO section, about $680\,\mathrm{m}$ downstream of the primary production target (see Fig. 5). A high-intensity negative hadron beam of $100\,\mathrm{GeV}/c$, which contains electrons at the level of 10%, is directed to the electron target. The hadrons mostly traverse the lead target, as its thickness is equivalent to only about 3% of an interaction length. In contrast, most of the electrons of the beam lose energy by bremsstrahlung. The outgoing electrons have a momentum spectrum that extends up to the momentum of the parent beam but with very low intensity yielding useful electron energies of up to $50\,\mathrm{GeV}$. The required electron momentum is selected with the beam line magnets located downstream of the lead target. For the nominal energies of 15, 20 and $40\,\mathrm{GeV}$, which are used for the calibration of the electromagnetic calorimeters, intensities up to a few 10^4 electrons per spill are routinely reached.

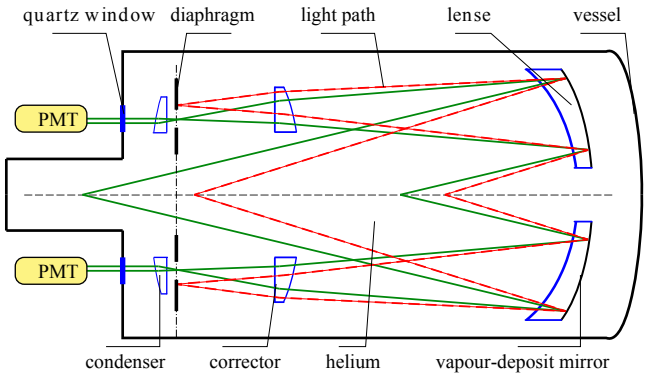

Figure 6: The basic principle of a CEDAR counter. Two particles with the same momentum but with different masses (here full and dashed lines) radiate Cherenkov photons at different angles, resulting in rings with different radii. A diaphragm selects the rings from the required particle type.

3.3. Beam particle identification

Two CEDAR detectors are installed $30\,\mathrm{m}$ before the COMPASS target region. They were designed to provide fast beam particle identification at high rates for particle momenta up to $300\,\mathrm{GeV}/c$ [6].

3.3.1. The principle of operation and the mechanical design

The principle of operation of a CEDAR detector is illustrated in Fig. 6. For a beam containing particles of different types but the same momentum, the angles of the emitted Cherenkov photons differ due to the different masses. The Cherenkov photons are focused onto the photon detectors using a mirror and a system of lenses (lens, corrector, condenser). This results in rings of photons at the focal plane whereby compensating for the chromatic aberration in the gas, which is mandatory for a proper separation of the rings. A ring shaped diaphragm, which is located in the focal plane perpendicular to the beam direction, selects photon rings with a fixed radius. The radius of the photon ring is matched to the radius of the diaphragm by adjusting the pressure of the helium gas in the vessel.

COMPASS operates two CEDAR detectors. Each consists of a $6\,\mathrm{m}$ long vessel containing pressurised He gas, a mirror, a lens system and a diaphragm (Fig. 7). The nominal pressure at $190\,\mathrm{GeV}/c$ beam momentum is 10.5 bar. The photons are detected with eight PMTs (Thorn-EMI-9820) equipped with passive voltage dividers.

The photon rings are smeared by several effects, e.g. temperature changes, beam divergence and limited precision of alignment. In order to keep the density constant along the $6\,\mathrm{m}$ long vessels and thus the refractive index, good thermal insulation and conduction is mandatory. The vessel is covered with copper filaments for thermal conduction and surrounded by a $10\,\mathrm{cm}$ thick polyethylene foam layer for insulation. In addition, the PMT voltage dividers are mounted outside the vessel. Particles travelling not parallel to the optical axis will produce shifted photon rings that do not match the diaphragm. A tilt of the beam with respect to the principal axis of the optical system can be corrected by adjusting the detector position with the help of a motorised base.

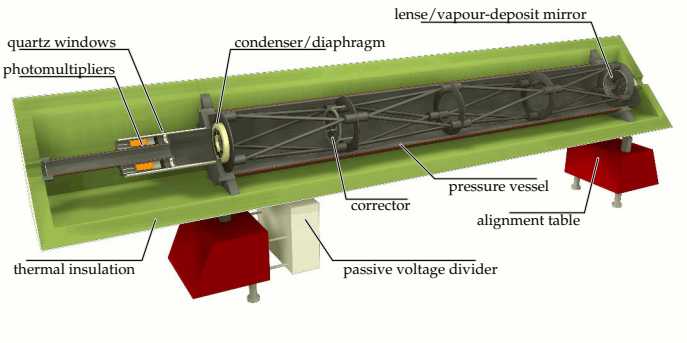

Figure 7: A cut through one of the CEDAR detectors.

The beam divergence could only be compensated by opening the diaphragm at the expense of a lower purity of the particle identification.

As the parallelism of beam tracks is of great importance for an efficient operation of the CEDARs, the beam divergence is optimised using pairs of single scintillating fibre detectors (one horizontal, one vertical) that were installed upstream (FISC1,2) and downstream (FISC3,4) of the CEDARs. Their position in the beam can be adjusted to measure the track angles by a coincidence between an upstream and a downstream fibre hit. Furthermore, two scintillating discs (TRIG 2) are installed as beam counters. They are used to normalise the CEDAR count rates during so-called pressure scans. While taking physics data, the discs and single-fibre detectors are moved out of the beam in order to reduce the material budget in the beam line.

As the ratio of pressure over temperature, p/T, is proportional to the refractive index, the working point of the CEDAR detectors is determined by performing pressure scans. In a pressure scan, the count rate normalised to the rate in the FISC counters is determined as a function of the pressure in the vessel and the multiplicity of PMT signals. Using the known beam composition, this yields also an online estimate for the particle identification efficiency. A more refined offline method will be discussed in Section 9.6. During data taking the He pressure in the CEDARs is regularly adjusted to compensate for He leakage and to keep p/T constant.

3.3.2. Separation of protons, pions and kaons (positive beam)

In the high-energy positive hadron beam, the proton component is dominant. For the CEDARs, a difference of $1\,\mathrm{mm}$ is expected between the ring radii of protons and kaons at $190\,\mathrm{GeV}/c$. The plateau of the efficiency is reached with a slit width of $1.2\,\mathrm{mm}$. Figure 8 shows an example of a pressure scan for three different requirements on the minimum number of PMT hits (multiplicity). The clear separation of pions and protons is obvious, while the small kaon component is hidden under the pion signal and cannot be distinguished here. From the measured rates and the known beam composition, a particle identification efficiency of almost 90% for protons is estimated using a multiplicity of ≥ 4 with a high purity of larger than 95% for the chosen working point of the CEDAR. During the data taking one CEDAR was set to identify protons, the other to identify pions.

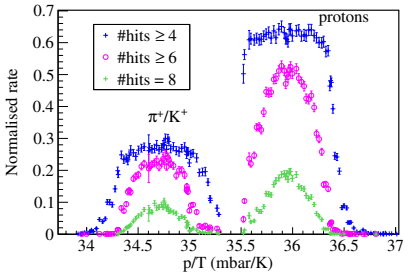

Figure 8: Pressure scan with CEDAR1 for a positive hadron beam with at least 4, 6 or 8 PMTs in coincidence. The kaon peak cannot be distinguished from the pion peak.

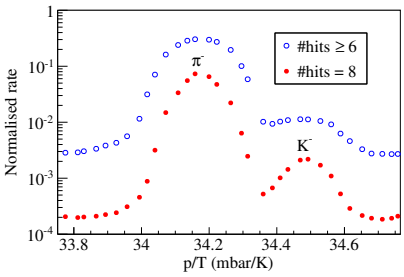

Figure 9: Pressure scan with CEDAR1 for a negative hadron beam with at least 6, or with 8 PMTs in coincidence.

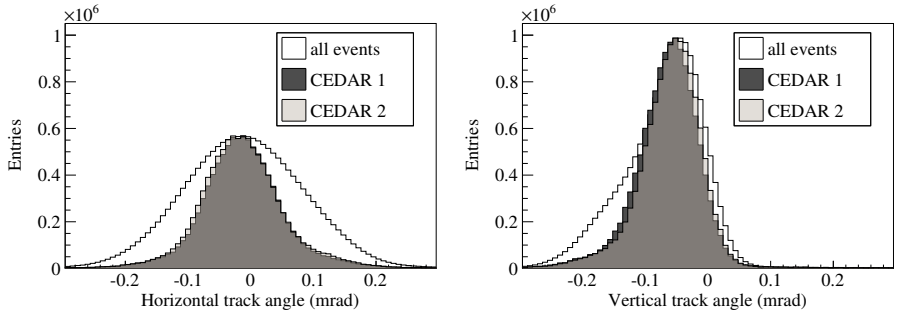

Figure 10: Horizontal (left) and vertical (right) track angles at the CEDARs. The angles for all tracks measured by the Silicon beam telescope and propagated back to the CEDAR positions are compared to the angles of the tracks accepted by CEDAR1 or CEDAR2. The acceptance of the CEDARs is reduced significantly for very divergent beam tracks.

3.3.3. Separation of kaons and pions (negative beam)

Negative hadron beams contain mainly pions with a small admixture of kaons and antiprotons. In this case, the CEDARs are used to identify kaons. Although the difference between the mean radii of the photons rings of kaons and pions at $190\,\mathrm{GeV}/c$ is less than $0.5\,\mathrm{mm}$, the diaphragm was set to $0.5\,\mathrm{mm}$ as a compromise between efficiency and purity. The pressure scan in Fig. 9 shows the obtained separation for multiplicities of ≥ 6 and 8. An online efficiency of about 35% is estimated for pions with a multiplicity of ≥ 6. Such a low efficiency is due to the high beam divergence of the very long beam line, in combination with the narrow slit width of the diaphragm. The loss due to the beam divergence is illustrated in Fig. 10 which shows the distributions of beam track angles as measured by the Silicon detectors upstream of the target and propagated back to the CEDAR position. The distribution for all beam particles are compared to those for beam particles identified online by CEDAR1 or CEDAR2.

Background in then photon detectors originates from several sources: halo particles, scintillation light produced by the beam and pile-up events during operation with a high-intensity beam. In order to suppress the background both CEDARs are set to

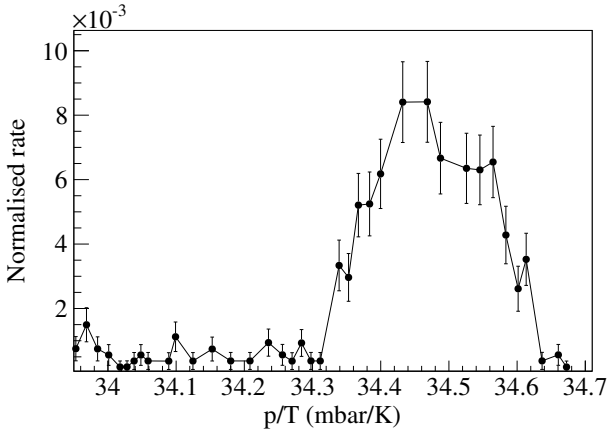

Figure 11: Count rate of coincident events recorded with CEDAR1 and CEDAR2. The pressure of CEDAR2 was scanned while CEDAR1 was set to detect kaons.

detect kaons. The amount of background can be estimated by setting one CEDAR to detect kaons and performing a pressure scan with the other CEDAR. As illustrated in Fig. 11, the resulting background is below 7%.

4. Target Region

The target region comprises the target systems, the Recoil proton detector, the Sandwich veto detector and the Silicon detectors (Fig. 4). Either liquid hydrogen or solid targets can be used during the measurements performed with hadron beams. The hydrogen and lead targets are used for diffractive dissociation and central production measurements. A nickel target is used for the study of the Primakoff reaction. The Silicon detectors, which are also located in the target region, will be described along with other tracking detectors in Section 5.

4.1. Liquid hydrogen target

For scattering on protons, a liquid hydrogen target is used. The target cell has a cylindrical shape with a length of $400\,\mathrm{mm}$ along the beam and a diameter of $35\,\mathrm{mm}$, which corresponds to a volume of 0.41 (Fig. 12). The thickness of hydrogen along the beam axis is equivalent to 4.5% of a radiation length (X_0) and 5.5% of a nuclear interaction length (λ_I). The diameter of the target is matched to the dimensions of the beam spot ($\sigma \approx 8\,\mathrm{mm}$) and kept small in order to reduce the amount of material traversed by recoil protons. The hydrogen is enclosed by a Mylar cylinder of $125\,\mu\mathrm{m}$ thickness ($5 \cdot 10^{-4} X_0, 2 \cdot 10^{-4} \lambda_I$). The liquid hydrogen inlet and gas outlets are constructed from stainless steel pipes, which are connected to a stainless steel ring surrounding the target Mylar cell. The hydrogen cell and the stainless steel pipes are wrapped with 10 layers of heat superinsulation foils (with thickness of $\leq 1\,\mu\mathrm{m}$/foil).

The target system with target cell, cryostat, and refrigerator is shown in Fig. 12. The target cell is surrounded by a cryostat tube made from aluminium. The cryostat

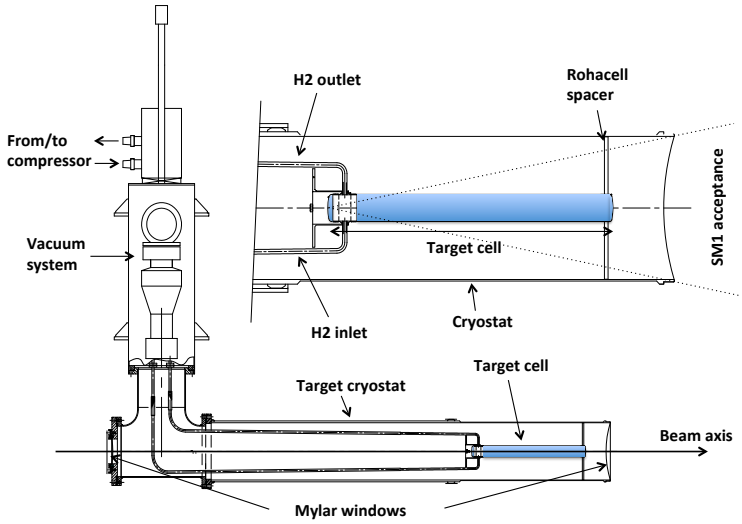

Figure 12: Side view of the liquid hydrogen target system. A closer view of the cylindrical Mylar cell and hydrogen piping is shown in the inset.

has a diameter of $185\,\mathrm{mm}$ and is terminated towards the spectrometer by a $250\,\mu\mathrm{m}$ thin Mylar window. Its diameter was chosen large enough so that forward going particles detected by the COMPASS spectrometer pass through the window and not through the aluminium cryostat itself. In order to reduce the amount of material traversed by the recoil particles, the thickness of the aluminium tube surrounding the target cell is $1.8\,\mathrm{mm}$ (see Fig. 4). The upstream $250\,\mu\mathrm{m}$ Mylar window of the cryostat has a diameter of $80\,\mathrm{mm}$.

During operation, the target cell is filled with about $0.4\,\mathrm{l}$ of liquid hydrogen. The necessary hydrogen is taken from a large buffer volume of about $850\,\mathrm{l}$, which is kept at room temperature. In warm mode (only hydrogen gas), the pressure of the hydrogen buffer is set to about $1800\,\mathrm{mbar}$. During the filling process, the hydrogen gas is cooled down inside a refrigerator and liquefied until the pressure in the buffer volume reaches about $1200\,\mathrm{mbar}$. This corresponds to about $0.6\,\mathrm{l}$ of liquid hydrogen. During operation, the pressure in the buffer volume is kept constant by a simple control unit regulating the effective cooling power of the refrigerator (5 W). The biggest fraction of the liquid drops into the target cell by gravity, while about 1/3 of it is kept in the $2.3\,\mathrm{l}$ condenser as a reserve. The heat exchange between the target cell and the condenser is driven by evaporation and condensation. The liquid inside the cell is just at the phase transition point and slightly bubbling. New liquid is continuously flowing from the condenser into the cell via the lower pipe, while the evaporated gas streams back into the condenser via the upper pipe where it is liquefied again. The target was designed

Table 3: Overview of target materials used during the measurements with hadron beams in 2008/2009.

Material	Number	Thickness x			
	(elements)	(mm)	$(\mathrm{g/cm^2})$	(λ_I)	(X_0)
Liquid H_2	1	400	2.84	5.5%	4.5%
Pb	6	0.250	0.284	0.14%	4.45%
Pb	2	0.125	0.142	0.07%	2.23%
Pb	2	0.025	0.028	0.01%	0.45%
Pb	2	0.050	0.057	0.03%	0.89%
W	2	0.050	0.097	0.05%	1.43%
W	2	0.025	0.048	0.03%	0.71%
Ni	1	4.2	3.74	2.8%	29.5%
W	1	0.025	0.048	0.03%	0.71%
W	1	0.050	0.097	0.05%	1.43%

such that bubbling should not affect the effective density by more than 3%. Evaporation of gas from the surface of the liquid occurs in the upper $2-3\,\mathrm{mm}$ of the target cell. The cell is tilted by $1\,\mathrm{mm}$ to insure that the gas flows back to the outlet. The resolution on the reconstructed vertex position is sufficient to discard events originating from the top of the cell.

Starting from room temperature, the filling of the liquid hydrogen target takes about 7 hours. The time for the evaporation of the liquid from the system is about 3 hours when the refrigerator is switched off. In order to allow for background measurements that require an empty target cell, the target system provides a fast emptying mode at low temperatures. For this purpose, the return pipe for the gas vapour is closed remotely by a pneumatic valve. Then, the pressure builds up rapidly by evaporation and pushes the liquid back from the cell into the condenser volume within a few minutes. The target is refilled by opening the valve.

The leakage rate of hydrogen was measured to be around $40\,\mathrm{mg}$ per day and allows for an operation of the target without any refill during the six months of a typical yearly data taking period. It has been observed that the vacuum in the cryostat degrades due to the diffusion of gases and water vapour through the thin Mylar vacuum windows ($0.1\,\mathrm{g}$ water per day). No indication for freezing of residual gases inside the cryostat was found in the offline analysis of physics data.

4.2. Nuclear targets

For measurements with nuclear targets, a light-weight target holder made of carbon fibre rods and thin frames of fibreglass reinforced epoxy (FR4) was used. Housing up to 16 target disks, the target holder is inserted into the RPD instead of the liquid hydrogen target. Figure 13 shows a schematic view of the target holder and the frames onto which the foils were glued.

The specifications of all targets used are listed in Table 3. Two different sets of nuclear targets were mounted on the target holder. The first set consisted of 16 thin disks made of Pb and W of natural isotopic composition. The thicknesses of the disks and the distance between them was chosen such that recoil protons from each individual

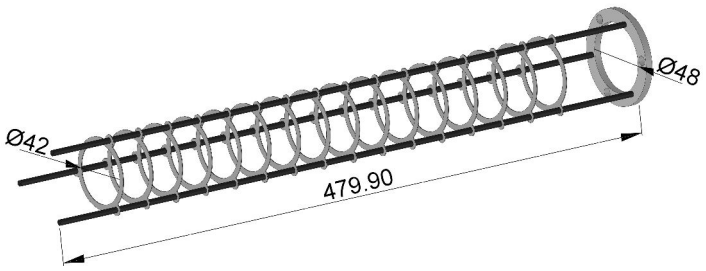

Figure 13: Schematic view of the target holder used for measurements with nuclear targets.

disk with momenta above $200\,\mathrm{MeV}/c$ could be detected over the full acceptance of the RPD. The more downstream disks were made thinner in order to minimise the effect of multiple scattering and conversion for events originating from the more upstream targets. The 12 Pb targets were used for diffractive dissociation measurements, while the four W targets were used for feasibility studies of a measurement of the π^0 lifetime.

The second set of target disks consisted of one $4.2\,\mathrm{mm}$ thick Ni disk and two thin disks of W. The W disks were separated by $30\,\mathrm{cm}$ from the Ni disk. This target set was used for Primakoff measurements and as an additional configuration for diffractive studies.

4.3. Recoil proton detector

The Recoil Proton Detector (RPD) measures the velocity and energy loss of the recoiling particles emitted at large angles. For particles produced in the middle of the target, the region of full acceptance covers polar angles from 50° to 90° (see Fig. 4). The energy loss of protons in the target walls and in the inner ring limits the lowest detectable momentum to $270\,\mathrm{MeV}/c$ in the case of the liquid hydrogen target. The RPD is also used in the trigger system (see Section 7) for the identification of protons.

The design of the RPD closely follows the design of the detector used for the GAMS NA12/2 experiment at CERN [7]. It is made of two concentric cylindrical barrels of plastic scintillators that surround the target and are referred to as "rings" in the following. The inner ring is segmented in 12 slabs of BC404® scintillator of dimensions $50 \times 6.6 \times 0.5\,\mathrm{cm}^3$, which are positioned at a radius of $12\,\mathrm{cm}$. Light guides for the inner ring are made of Plexiglas and have a fish-tail geometry. They are tilted at an angle of 15° with respect to the longitudinal axis in order to stay outside of the acceptance in the forward region.

The outer ring is segmented in 24 slabs of plastic scintillators with dimensions of $115 \times 20 \times 1\,\mathrm{cm}^3$, produced at IHEP Protvino [8]. Each slab is made of a single piece of material that also includes a $29\,\mathrm{cm}$ long light guide on each side. The ends are cut, twisted and molded to fit into a $3.9\,\mathrm{cm}$ diameter cylinder, to which the PMTs are attached. The radius of the outer ring is $75\,\mathrm{cm}$. Each element covers an azimuthal angle of 15°. In order to optimise the azimuthal angle resolution, the outer ring is positioned such that each inner ring counter faces three outer ring slabs as viewed from the target centre (see Fig. 54).

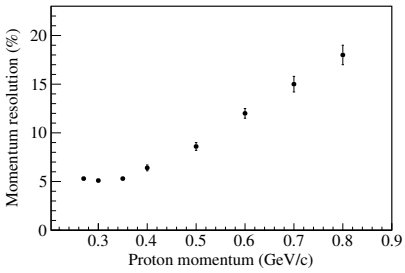

Figure 14: Momentum resolution of the RPD for protons detected at an angle of 70° relative to the beam axis.

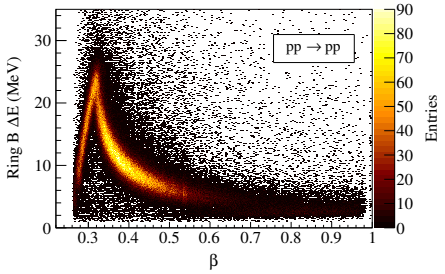

Figure 15: Energy loss ΔE in the outer ring of the RPD as a function of the velocity of the particle in elastic pp scattering.

Each scintillator is read-out at both sides using EMI 9813B photomultiplier tubes. The PMTs are equipped with active voltage dividers to cope with the high rate and high light output. The PMT signals are split using 8-fold active splitters [9] and sent to ADCs (2 dynamic ranges) and TDCs (2 threshold levels). The remaining outputs are used for the trigger system. Two outputs are connected to leading edge discriminators with two different thresholds. Furthermore, the signals from the inner ring downstream PMTs have the smallest time jitter with respect to the incoming track since light in the scintillator propagates in the same direction as the scattered particle. The signals from these are sent to Constant Fraction Discriminators to preserve their good timing properties. All logic signals are then fed into a FPGA-based system for triggering (see Section 7).

The properties of each individual counter were measured during earlier tests using muons from the beam halo with the RPD positioned transversely to the beam. The resolutions obtained are $\sigma(t) = 200\,\mathrm{ps}$ and $\sigma(z) = 2.7\,\mathrm{cm}$ for the inner ring elements and $\sigma(t) = 400\,\mathrm{ps}$ and $\sigma(z) = 5.0\,\mathrm{cm}$ for the outer ring elements. The attenuation lengths of both types of counters were measured and found to be of the order of $60\,\mathrm{cm}$.

The momentum resolution as a function of the proton momentum is measured using pion-proton elastic scattering events. The proton transverse momentum is measured in the RPD and then compared to the value calculated from the kinematics of the pion that is detected in the spectrometer. The width of the resulting momentum distribution is shown as a function of the proton momentum in Fig. 14. It is in agreement with an estimation performed using the time and position resolutions of the RPD, as determined from test beam data.

Figure 15 shows the energy loss in the outer ring as a function of the velocity measured with the RPD for elastic pp scattering. For velocities of up to $\beta = 0.34$ the protons are stopped in the outer ring. Above this value the protons escape the scintillator and deposit in it only part of their energy. The figure for pions would be similar and the energy loss for stopping pions would reach a maximum value of $10\,\mathrm{MeV}$ for $\beta = 0.4$. Therefore, proton particle identification is ensured only for $\beta < 0.4$. In Fig. 15 there is no indication for presence of pions, as expected in pp elastic scattering.

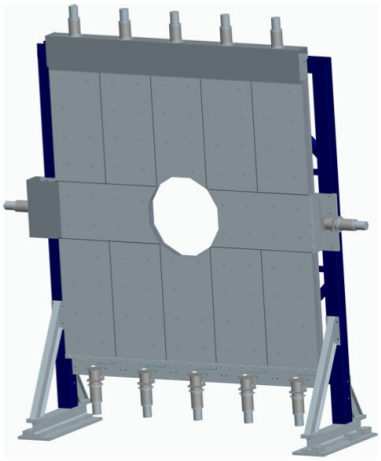

Figure 16: Sketch of the Sandwich veto detector. The active area of the detector (depicted in grey) has dimensions of $200 \times 200\,\mathrm{cm}^2$.

4.4. Sandwich veto detector

The role of the Sandwich veto detector [10] lies in vetoing events in which photons or charged particles reach the acceptance gap between RPD and LAS (see Fig. 4). This detector is a $2\,\mathrm{m} \times 2\,\mathrm{m}$ stack of five layers of steel-covered lead plates and scintillators with a total thickness of 5.1 radiation lengths. Segmented in 12 elements (Fig. 16), the detector has a central hole that matches the acceptance of the spectrometer. Each lead layer consists of $5\,\mathrm{mm}$ Pb plates, with $1\,\mathrm{mm}$ steel plates on each side to insure the stiffness of the assembly. Each scintillator layer is formed of a pair of $80 \times 20\,\mathrm{cm}^2$ scintillator bars lying side-by-side. The first three layers are $1\,\mathrm{cm}$ thick, the last two $0.5\,\mathrm{cm}$. The light is extracted from the scintillators using wavelength-shifting fibres connected to photomultiplier tubes. The Sandwich veto efficiency was measured to be 98% for minimum ionising particles [10]. Using MC simulation, the efficiency was also determined to be higher than 95% for pions with energies larger than $50\,\mathrm{MeV}$ and higher than 90% or 80% for photons with energies larger than $100\,\mathrm{MeV}$ or $50\,\mathrm{MeV}$, respectively. The effect of the Sandwich veto detector on the trigger rates is described in Section 7.2.

5. Tracking Detectors

The tracking system of COMPASS is composed of many tracking stations, each consisting of a set of planar tracking detectors of a given type located at approximately the same z-coordinate along the beam. Many different detector technologies with different sizes, granularities and resolutions are in use. Far from the beam in the outer region, large areas of several square meters have to be covered in order to detect low-momentum particles scattered at large angles. Close to the beam in the inner region, the particle rates quickly increase with decreasing distance to the beam, requiring fast detectors with good resolution. The large-area tracking is provided by several variants

of wire-based gas detectors such as Multiwire Proportional Chambers (MWPC), Drift Chambers (DC), and Straw Tube Chambers. The region closer to the beam, where the particle rates are too high for wire-based detectors, is covered by two types of Micropattern Gaseous Detectors with strip readout, namely the Micromegas and Gas Electron Multiplier (GEM) detectors. The beam region itself, where rates above $10^5\,\mathrm{mm}^{-2}\mathrm{s}^{-1}$ are observed, is equipped with Scintillating Fibre Detectors and novel GEM detectors with pixel readout, the PixelGEMs. Tracking immediately upstream and downstream of the target is performed by silicon microstrip detectors.

This section focuses on the upgrades of the tracking system for the hadron program as compared to the setup used for muon beams, detailed in [1]. For some detectors, like the straw tube chambers, the multiwire proportional chambers, and the large area drift chambers, no mentionable changes were introduced, and therefore they are not described here. These detectors are however discussed in detail in [1]. The wire and strip detectors measure different projections of a particle penetration point. They are called X and Y-planes when measuring horizontal and vertical coordinates, respectively. Detector planes measuring coordinates that are rotated clock or and anti-clockwise by a given angle with respect to the x-axis, are called U and V-planes, respectively.

5.1. Silicon Microstrip Detectors

The COMPASS silicon microstrip tracking system consists of three stations upstream of the target, which are used as a beam telescope, and two stations downstream of the target, which are used for vertex reconstruction. As these detectors are traversed by the beam particles and by the forward-boosted reaction products, they are prone to radiation damage. The damage affects the bulk material in terms of change of doping, and the surface in terms of decrease of insulation, resulting in an increase of the depletion voltage and of the leakage current, respectively. In order to minimise these effects, the detectors are cooled with liquid nitrogen. Since the leakage current decreases with temperature, noise caused by radiation damage is suppressed. In addition to this, the cooling leads to a significant improvement of the spatial and time resolution compared to room-temperature operation, as discussed below. While the system was designed to cool the detectors down to $130\,\mathrm{K}$, the desired performance is already achieved at $200\,\mathrm{K}$, which reduces the thermal stress on the modules.

One station comprises two Silicon detectors with a stereo angle of 5° between their respective strip orientations to resolve multi-track hit ambiguities. Each detectors consist of a $300\,\mu\mathrm{m}$ thick silicon sensor with an active area of $50\times70\,\mathrm{mm}^2$. The signals are picked up on both sides, by 1280 strips on the n-side and 1024 perpendicularly-oriented strips on the p-side. The sensors are glued onto two L-shaped FR4 printed circuit boards (L-boards) that hold the APV25-S1 [11] based readout electronics. There are three cryostats for the beam stations upstream of the target and one conically shaped cryostat housing the two stations downstream of the target (see Fig. 4).

The cooling system of the Silicon detectors has to fulfil the requirement of a minimal amount of material within the acceptance of the spectrometer. This prevents a solution, in which the detectors are connected to a massive cold head to dissipate the electronic heat. The technology developed for these detectors is based on the evaporation of liquid nitrogen in thin capillaries on the PCBs. The schematic layout of the Silicon cooling system is shown in Figs. 18 and 19. In order to dissipate about $8\,\mathrm{W}$

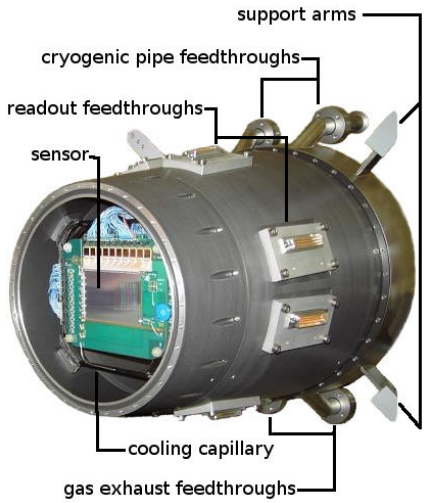

Figure 17: The conical cryostat with the upstream beam window dismounted. The height of the PCB frame that holds the detector (sensor) is about $100\,\mathrm{mm}$, the length of the full cryostat about $400\,\mathrm{mm}$. The bent cooling capillary is fixed to the PCB close to the sensitive area of the detector. Inside the cryostat, the readout cables are directly soldered to the detector module and plugged to vacuum-sealed feedthrough connectors also visible on the outer surface of the cryostat.

from each detector, purely liquid nitrogen must be provided to the capillary. For this purpose, a dedicated phase separator that removes the gaseous nitrogen is incorporated in each cryostat. The whole cooling infrastructure increases the material thickness of the PCB on average by 0.1% of a radiation length.

The nitrogen arrives from a central liquid nitrogen dewar located in the vicinity of the experimental hall. It is transferred by a $100\,\mathrm{m}$ long vacuum-isolated transfer line to a valve box near the Silicon stations. The valve box (Fig. 18) also acts as a buffer for the liquid nitrogen that is kept at $1.8\,\mathrm{bar}$ absolute pressure. The liquid nitrogen is brought to the Silicon stations using 2–$3\,\mathrm{m}$ long transfer lines. When the nitrogen reaches the phase separator, the gas that evaporated in the transfer line is allowed to escape. At the bottom of the phase separator, where there is only liquid nitrogen, two capillaries are connected, one for each detector. The thermal contact to the L-boards is made by soldering dots. The temperature of the detector is regulated through the gaseous exhaust flow with a feedback time in the order of one second. All components are operated by a Programmable Logic Controller (PLC, SIMATIC S7 300), utilising a Proportional-Integral-Derivative algorithm for the temperature regulation. The software used is a Java™-based application called Muscade[12] which provides real-time monitoring, remote control, data storage, and an alarm system.

In 2009, all Silicon stations were cooled to $200\,\mathrm{K}$. The temperature of the system was stabilised to within $\pm 1\mathrm{K}$ for all detectors of the upstream stations. Slightly larger variations were observed for the detectors in the conical cryostat, where a partly blocked capillary prevented good cooling for one of the detectors, limiting the tem-

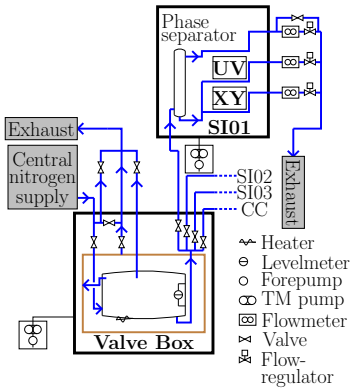

Figure 18: Block diagram of the valve box and the first upstream cryostat labelled SI01. The other two upstream cryostats SI02 and SI03 are equipped analogously. The downstream conical cryostat (CC) is shown in Fig. 19. The phase separators are integrated in the cryostats near the detectors, but outside the acceptance.

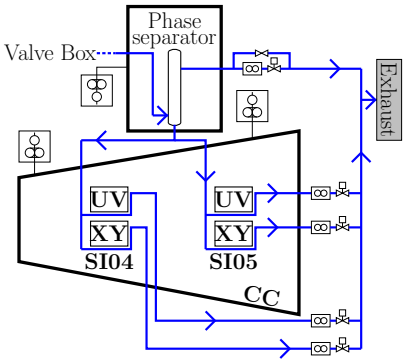

Figure 19: Block diagram of the conical cryostat (CC), symbols as in Fig. 18. The phase separator is mounted in an extra housing outside the spectrometer acceptance with a vacuum connection to the cryostat.

perature to $\sim 220\,\mathrm{K}$ only. This detector also exhibited slow drifts following the daily temperature variations.

The spatial resolution of the cold Silicon detectors is in the range $4 - 6\,\mu\mathrm{m}$ for clusters when two strips are hit and amplitude weighting can be employed to determine the track position [13]. When only one strip is hit, the resolution is in the range $7 - 11\,\mu\mathrm{m}$. This spatial resolution is illustrated in Fig. 20 for one of the detectors. It represents an improvement of 15-20% compared to room-temperature operation [1]. The reduction of the leakage current and the increase of the signal each contribute of about 10% to this improvement. The time resolution, displayed in Fig. 21, is improved for the same reason and is in the range $1.4 - 1.8\,\mathrm{ns}$.

The efficiency was studied in detail with a high-intensity muon beam. Tracks reconstructed without taking into account hits of the detector under study are used to measure the efficiency by providing the expected hit position on the detector. The presence of a hit is then checked within a $\pm 3\sigma$ window around the expected position. The measured efficiency is above 99% as shown in Fig. 22 for one of the planes. Similar results were also obtained for operation with hadron beams.

5.2. PixelGEM Detectors

In order to minimise the material from detectors directly exposed to the hadron beam, some of the scintillating fibre detectors that were used with the muon beam were replaced by thinner detectors based on Gas Electron Multiplier (GEM) foils [14]. Starting with the first hadron run in 2008, five GEM detectors with a novel kind of readout and a thickness in the beam region of $0.26\,\%$ of a radiation length (X_0) and $0.1\,\%$ of a nuclear interaction length each (λ_I) were installed, thereby reducing the

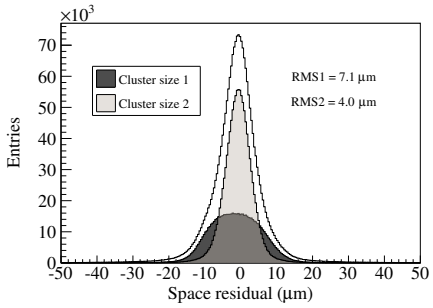

Figure 20: Spatial resolution as determined for a single Silicon detector plane. "RMS1" and "RMS2" refer to the cases of clusters with one and two hit strips, respectively.

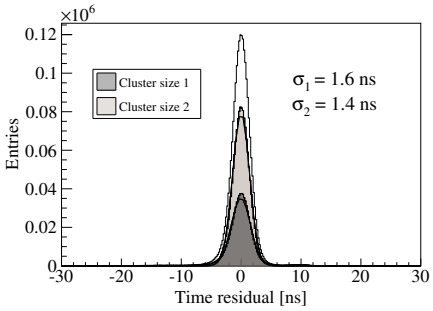

Figure 21: Time resolution of a single Silicon detector projection.

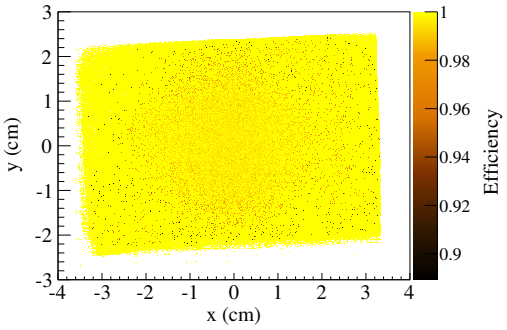

Figure 22: Two-dimensional efficiency distribution for a plane in the beam telescope. The stereo-angle tilt of the sensitive area is visible.

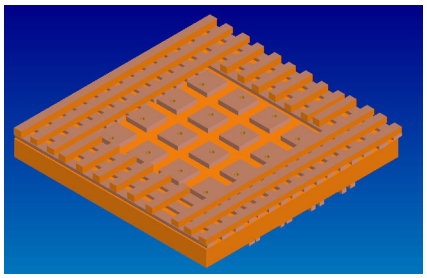

Figure 23: Schematic view of the pixel and strip region of the readout circuit. Note that the pixel region consists of 32×32 pixels of $1\,\mathrm{mm}^2$ size each, while only 4×4 are shown for clarity. Figure not to scale.

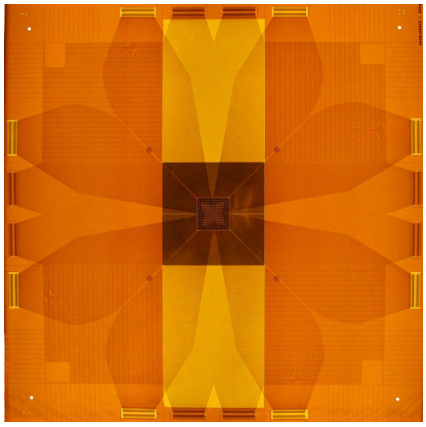

Figure 24: The PixelGEM read-out foil. The inner $10 \times 10\,\mathrm{cm}^2$ darkest part is the active area. The symmetric wires connecting the pads and the strips to the read-out electronics surround this part.

material budget of the whole system by a factor of 5–10 compared to the scintillating fibre detectors.

GEM detectors with a two-dimensional strip readout have been used in COMPASS since its start-up [15]. These gaseous detectors have proved to be able to cope with the high particle fluxes in the beam centre, but the strip readout makes it impossible to separate individual hits close to the beam due to a too high occupancy. In order to overcome this limitation, a novel read-out structure has been realised on a polyimide basis using the GEM patterning and wet-etching printed-circuit board (PCB) technologies [16]. The central are of $32 \times 32\,\mathrm{mm}^2$ with 1024 pixels of $1 \times 1\,\mathrm{mm}^2$ size each are patterned on one side of $50\,\mu\mathrm{m}$ thick polyimide foil. The signal traces from the pixels to the readout electronics are routed on the other side of the foil, with an extremely small width of only $50\,\mu\mathrm{m}$ and a pitch of $100\,\mu\mathrm{m}$. The rest of the total active area of $100 \times 100\,\mathrm{mm}^2$, where the occupancy is sufficiently low, is covered by two orthogonal sets of 512 strips with a pitch of $400\,\mu\mathrm{m}$, realised on a second $50\,\mu\mathrm{m}$ thick polyimide foil. The strip foil is then glued onto the one with the pixels, with the central area completely removed from the strip foil in order to open the pixels for charge collection. The strips are split in the middle and read out on both sides in order to equalise their capacitances, also for the ones not ending at the pixel region. In Fig. 23, the pixel and strip regions are displayed schematically, while Fig. 24 shows a photograph of the complete readout foil. The readout foil is glued onto a light honeycomb sandwich panel of $610 \times 610\,\mathrm{mm}^2$ size, which serves as support plate and also carries the front-end electronics, the high voltage distribution circuit, and the GEM stack.

The GEM stack consists of three GEM foils of $10 \times 10\,\mathrm{cm}^2$ active area, stretched and glued onto larger frames of fibre glass material with $316 \times 316\,\mathrm{cm}^2$ inner dimensions. These frames with a thickness of $2\,\mathrm{mm}$ are piled up and glued on top of each other. The active part of a GEM foil is sectorised on one side into four parallel sectors of equal size, and a fifth sector in the centre matching the pixel area of $32 \times 32\,\mathrm{mm}^2$. In

order to minimize inefficiencies and spatial distortions of the drifting charge cloud at the sector boundaries, the spacing between adjacent conductive Cu surfaces was chosen to be $150\,\mu$, the spacing between GEM holes in two neighbouring sectors $350\,\mu$, both values limited by the production yield. The central sector requires a separate line between two longitudinal sectors, which locally increases the gap between holes to $550\,\mu$.

The foils are mounted such that the segmented sides face the drift cathode. The potentials on the foils are defined through an external resistive divider. They are adjusted such that the largest gain is provided by the first foil and it is stepwise decreasing for the second and third foil. The segmented sides of a foil are supplied through individual $10\,\mathrm{M}\Omega$ loading resistors, while there are no loading resistors for the non-segmented side. This configuration allows for an operation of the detector even with a potential permanent short circuit in one of the sectors, and avoids a high electric field between the last foil and the readout circuit in case of a discharge [**?**]. The central sector of the third GEM foil is powered by a separate supply through a $1\,\mathrm{M}\Omega$ serial resistor, which allows an independent adjustment of the gain for the central region. This takes into account the fact that a smaller effective gain is necessary for the central region because the signal is induced on pads instead of two sets of strips for the peripheral region. Efficiency scans performed with prototype detectors showed that an effective gain of 8000 is required for the strip region for fully efficient detection of minimum ionising particles, while a gain of 6000 is sufficient for the pixel region. The triple amplification together with the non-uniform gain distribution and the segmented GEM foils, which were already used for the large-size COMPASS GEM detectors [17], ensures operation of the PixelGEM detectors without electrical discharges even in a high-intensity hadron beam.

In order to minimise the material in the region near the beam, the gas-filled volume extends to cover a total area of $316 \times 316\,\mathrm{mm}^2$. It is enclosed by a frame defining the conversion volume, and a smaller honeycomb panel of $330 \times 330\,\mathrm{mm}^2$ size, which carries the cathode foil made of Cu-coated polyimide. The material exposed to the beam is minimised by central holes of $30\,\mathrm{mm}$ diameter in both honeycomb panels and by reducing the thickness of each of the Cu layers on the drift cathode and the GEM foils from originally $5\,\mu\mathrm{m}$ to about $1\,\mu\mathrm{m}$.

Figure 25 shows a top view of an assembled detector, with the high voltage distribution board (lower right corner) and the 16 front-end electronics cards mounted upside-down. During operation the whole detector is shielded from external electronic noise by a thin aluminium-coated Mylar foil. As the large-area GEM detectors, the PixelGEM detectors are operated in a gas mixture of Ar/CO_2 (70%/30%).

A total of 2048 channels per detector are read out using the APV25-S1 preamplifier/shaper ASIC [11], which samples the input signal at a frequency of $38.88\,\mathrm{MHz}$ into an analog pipeline with a depth of 160 samples. Each chip is mounted onto a separate front-end card connected to the readout circuit using high-density 130-pin connectors, of which two pins are used to connect the ground level of the chip to the detector ground. In contrast to the large-area detectors, where the front-end cards were directly wire-bonded to the readout circuit, the connector solution provides much more reliability and allows for a simple replacement of faulty cards. The front-end cards also contain an external protection network consisting of a pair of high-speed switching

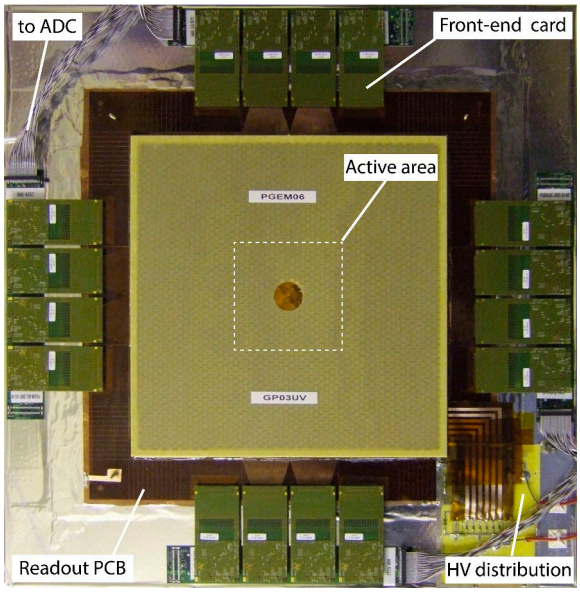

Figure 25: A fully assembled PixelGEM detector, equipped with 16 APV front-end cards. The digitisation of the analog signals from the APVs is done at an external ADC card, which is connected via the grey cables.

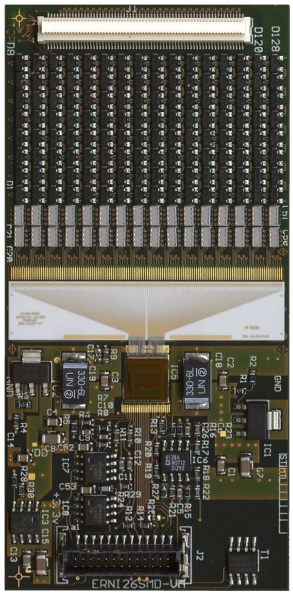

Figure 26: Front-end card carrying (from top to bottom) the 130-pin connector, the protection network, a ceramic pitch adaptor, and the APV25-S1 ASIC for analog sampling of the signals induced on the readout electrodes.

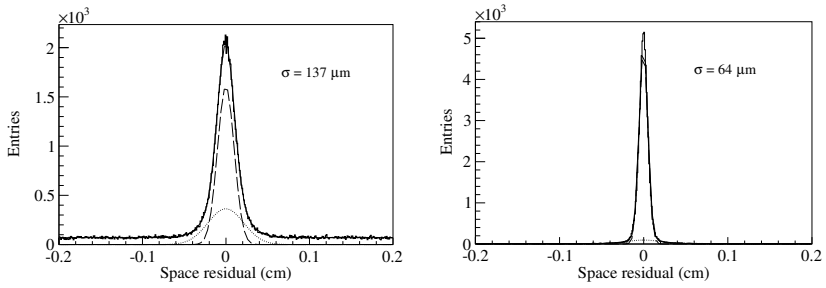

Figure 27: Residual distribution (difference between measured cluster position and track penetration point) in x-direction for (left) the pixel region and (right) the strip region of a PixelGEM detector. The quoted residual widths are obtained from fits of a sum of two Gaussians. When corrected for the track uncertainties, spatial resolutions of $106\,\mu\mathrm{m}$ (pixels) and $54\,\mu\mathrm{m}$ (strips) are obtained for this particular detector.

diodes (BAV99) and an AC coupling using a $220\,\mathrm{pF}$ capacitor for each channel, and a ceramics pitch adaptor. Figure 26 shows a photograph of the front-end card. Three signal amplitudes per channel are multiplexed onto a single differential line for each APV25-S1 chip and digitised by a pipelined 12-bit differential ADC at a sampling rate of $40\,\mathrm{MHz}$. The signals from sixteen APV25-S1 chips are digitised on a custom-made ADC card. This card also includes a Virtex FPGA [18], which performs pedestal subtraction with individual values for each channel, common mode noise correction and zero suppression by applying individual thresholds for each channel.

After a successfully operated prototype, which was tested in a muon beam with a flux up to $1.2 \cdot 10^5\,\mu^+/\left(\mathrm{mm}^2\mathrm{s}\right)$ [19; 20], five PixelGEM detectors were installed in the spectrometer in 2008. One detector was placed about $2.5\,\mathrm{m}$ downstream of the target. Two pairs of detectors mounted back to back, with the second rotated by 45° with respect to the first, were installed around SM2, at $19\,\mathrm{m}$ and $24\,\mathrm{m}$ downstream of the target, respectively (see Fig. 3).

In the offline analysis, a pulse-shape analysis technique is used to extract the signal amplitude and time for each channel, a feature of great importance in a high-intensity environment. Signals from neighbouring pixel channels on the detector are then weighted by their amplitudes and grouped into clusters. Corrections for a non-linear charge sharing between pixels are applied. These corrections have been determined in a dedicated test beam experiment, using high-resolution silicon microstrip detectors [19]. At this stage also a small (percent-level) cross-talk between channels, arising from the narrow and long PCB traces between the pixels and the front-end cards, is removed. For the strip signals a simpler clustering algorithm based on a centre-of-gravity method is applied.

In the following, the performance of the PixelGEM detectors at a hadron beam flux density of $2.4 \cdot 10^4\,\pi^-/\left(\mathrm{mm}^2\mathrm{s}\right)$ (total flux of $6.3 \cdot 10^5\,\pi^-/\mathrm{s}$), used for data taking, is shown. Figure 27 shows the residual distribution, i.e. the difference between the measured cluster position and the extrapolated penetration point of a reference track, for the pixel region (left) and the strip region (right). As for the Silicon detectors, the detector under investigation has been excluded from the track reconstruction, such that unbiased residuals are obtained. The residual distributions are fitted with the sum of

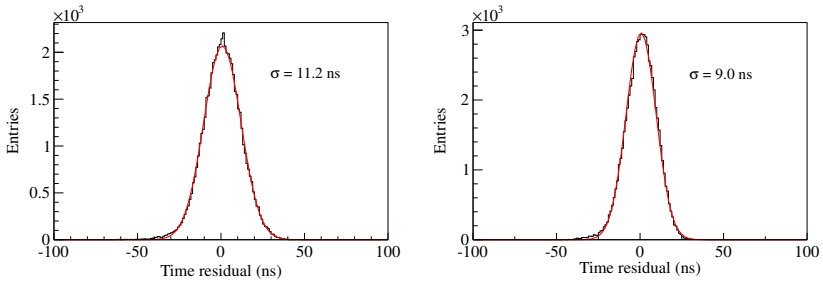

Figure 28: Time residual distribution (difference between measured cluster time and track time) for (left) the pixel region and (right) the strip region (x-direction) of a PixelGEM detector.

a constant background and two Gaussians to account for different cluster sizes and regions in the detector where the resolution is deteriorated due to sector boundaries. After deconvolving the uncertainty on the reconstructed tracks, one obtains, for all five PixelGEM detectors, spatial resolutions distributed around an average value of $125\,\mu\mathrm{m}$ with a standard deviation of $13\,\mu\mathrm{m}$ for the pixel regions, and an average value of $65\,\mu\mathrm{m}$ with a standard deviation of $12\,\mu\mathrm{m}$ for the strip regions. From the pulse-shape analysis of the three samples read out per channel per event, one can extract the time of the signal and thus efficiently remove background hits due to pile-up. The time resolution is then determined by comparing the time extracted that way with the one measured by scintillation detectors for a given track, as shown in Figure 28 for one particular detector. The time resolutions obtained for the five PixelGEM detectors are distributed around an average value of $11.2\,\mathrm{ns}$ with a standard deviation of $1.7\,\mathrm{ns}$ for the pixel regions and an average value of $9.4\,\mathrm{ns}$ with a standard deviation of $1.1\,\mathrm{ns}$ for the strip regions.

In order to determine the efficiency ϵ of a detector in a high-background environment, one has to take into account the presence of uncorrelated background hits that may fall within the road width around a track with a probability b and thus artificially increase the apparent efficiency $\epsilon_{\mathrm{app}} = \epsilon + b(1-\epsilon)$. Here, the background probability b at a given position on the detector is determined from hits that fall outside the road width around a given track used for the efficiency calculation. Figure 29 shows the background-corrected efficiency for a complete detector plane. Here, the pixel region is merged into the strip region, hence the complete active area of $10 \times 10\,\mathrm{cm}^2$ is shown. The lines of lower efficiency parallel to the x and y axes correspond to the boundaries between the HV sectors on the GEM foils. Few, or no tracks are reconstructed in the ring-shaped region when this particular detector is excluded from the tracking to obtain an unbiased efficiency determination. Background-corrected efficiencies for the PixelGEM detectors were found to be above 97% for all detectors during data taking in 2008.

The PixelGEM detectors are also used for data taking with muon beams of intensities around $10^7\,\mu^+/\mathrm{s}$.

5.3. Micromegas Detectors

Twelve Micromegas (MicroMesh Gaseous Structure, or MM) detectors are used for tracking particles emitted at small angles. Assembled in 3 stations of four detectors each, they are installed in the region between the target and the first dipole magnet SM1. Each MM detector covers an active area of $40 \times 40\,\mathrm{cm}^2$, except a central dead zone with a diameter of $5\,\mathrm{cm}$, and measures a single projection of a particle track crossing the detector. To this end, the anode plane is divided in three zones, a central zone with 512 strips and pitch of $360\,\mu\mathrm{m}$, and two outer zones, each with 256 strips and pitch of $420\,\mu\mathrm{m}$. The detectors, of 1024 strips each, have a parallel plate electrode structure, with a volume separated into two regions: a $5\,\mathrm{mm}$ conversion gap with a moderate electric field (less than $1\,\mathrm{kV/cm}$), where the ionising particle produces primary electrons, and an amplification gap of $100\,\mu\mathrm{m}$ with a much stronger field (typically $40\,\mathrm{kV/cm}$), where the primary electrons generate an avalanche. A $5\,\mu\mathrm{m}$ thin metallic micro-mesh (grid), which captures most of the ions produced during the avalanche, separates the two regions. Another grid, which is used as a drift electrode, defines the conversion gap region.

From 2006 onwards, the original MM detectors [1] were modified in order to satisfy two additional requirements: operate in a strong magnetic field, and withstand an increased flux of highly-ionising particles during data taking with hadron beam. The first requirement comes from the use of a superconducting magnet with a $2.5\,\mathrm{T}$ solenoid field during data taking periods with the muon beam and the polarised target. This magnet, designed to match the large angular acceptance of the COMPASS setup, produces a strong fringe field that reaches $1\,\mathrm{T}$ at the level of the nearest MM detector. In order to minimise the effect of the solenoid field on the detector, the nickel grids used in the first generation MMs were replaced with new $5\,\mu\mathrm{m}$ thin, non ferromagnetic copper grid foils. The new mesh used for the amplification gap has $65\,\mu\mathrm{m}$ diameter holes and a pitch of $90\,\mu\mathrm{m}$. The corresponding values of the drift electrode are $300\,\mu\mathrm{m}$ and $600\,\mu\mathrm{m}$.

The second requirement comes from the use of hadron beams, which produce a large number of highly ionising secondary particles and generate nearly three orders of magnitude more discharges per incident particle. Since the discharge rate is proportional to the gain of the detector, the size of the conversion gap was enlarged from $3.2\,\mathrm{mm}$ to $5\,\mathrm{mm}$ in order to increase the number of primary electrons. The detectors could then be operated at a lower gain while preserving a good efficiency. The gas mixture used is Ne/C_2H_6/CF_4 with corresponding volume fractions of 85%/10%/5%. In comparison to data taking with a muon beam, the CF_4 component was decreased from 10% to 5%, thereby further reducing the discharge rate at the expense of a slight decrease of the electron drift velocity. At the nominal hadron beam intensity of 5×10^6 particles per second impinging on a $40\,\mathrm{cm}$ long liquid hydrogen target, each MM detector sees an integrated flux of up to $30\,\mathrm{MHz}$, reaching $100\,\mathrm{kHz}$ per strip near the central dead zone. The mean discharge rate in such conditions varies between $0.026\,\mathrm{Hz}$ and $0.050\,\mathrm{Hz}$, depending on the specific plane and HV settings. During a discharge the micromesh voltage decreases and thereby reduces the efficiency of the detector. The decrease is recovered several microseconds after the discharge.

For all MM detectors, a digital readout of the signal using the SFE16 chip is used. When recording the leading and the trailing edges of a signal, both the mean time

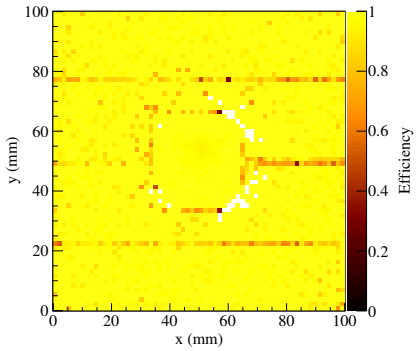

Figure 29: Efficiency of one of the PixelGEM detectors, measured in a high-intensity hadron beam. The horizontal lines with reduced efficiency correspond to boundaries between GEM sectors. In the white region not enough tracks are reconstructed when this particular detector is excluded from the tracking.

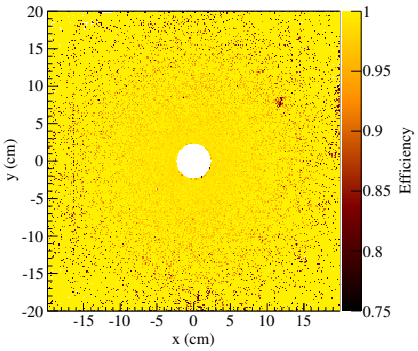

Figure 30: Two-dimensional efficiency of a Micromegas detector. The empty region in the middle is the $5\,\mathrm{cm}$ central dead zone.

and the amplitude of a hit can be calculated, the latter by using a time-over-threshold technique. Adjacent hits are then combined to clusters. The average cluster size is 2.8 and 3.2 in the region with $360\,\mu\mathrm{m}$ and $420\,\mu\mathrm{m}$ pitch, respectively. The mean value of the time resolution is $14\,\mathrm{ns}$, compared to $8.5\,\mathrm{ns}$ measured for the first generation of MM detectors. This loss in performance is due to the combined effect of the increased conversion gap size, the decrease of the drift-gap electric field, and the use of a smaller fraction of CF_4 in the gas mixture.

The efficiencies of the MM detectors are determined using the same method as described in Section 5.2 for the PixelGEM detectors. A two-dimensional representation of the efficiency of one of the detectors is shown in Fig. 30. The mean efficiency values obtained for the other 11 MM detectors are all in the range 97.5% - 98.5%. Note that the use of copper grids with a less favourable geometric transparency than that of the nickel grids has negligible effect on the final efficiency values.

Figure 31 shows the space residual distribution of a MM detector for nominal beam intensity and running conditions. After subtracting the contribution of the track uncertainty, the intrinsic spatial resolution obtained is $105\,\mu\mathrm{m}$. The resolution value is a weighted average of the resolution in the central zone ($360\,\mu\mathrm{m}$ pitch), and that of the two outer zones ($420\,\mu\mathrm{m}$ pitch). The four detectors of the third MM station operate in the fringe field of the SM1 dipole magnet, which exerts a Lorentz force on the drifting electrons. The resolution of these detectors varies from 110 to $145\,\mu\mathrm{m}$, depending on the orientation of the strips relative to the SM1 field lines.

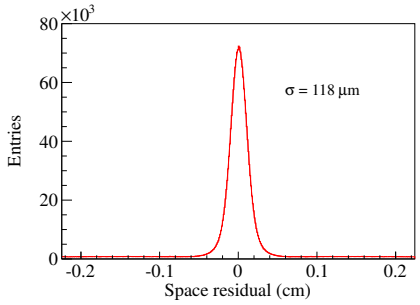

Figure 31: Space residual distribution of a Micromegas detector. The quoted residual width is obtained from a fit of a sum of two Gaussians.

5.4. Drift Chambers

A new large-size multiwire drift chamber (DC4) was installed already in 2006 in the LAS part of the setup. The design of DC4 closely follows that of the medium-size DC trackers [1] already operational in the COMPASS set-up, while the overall dimensions were enlarged to match the angular acceptance downstream of the SM1 magnet. The distance between active wires was increased by $1\,\mathrm{mm}$ and the angle of the inclined wires was decreased. The DC4 chamber also features a water-cooling system, which ensures a good temperature stability of its frame.

The external dimensions of the DC4 detector are $294 \times 254 \times 17\,\mathrm{cm}^3$ with an active gas area of $248 \times 208\,\mathrm{cm}^2$. The detector has eight layers of wires and four wire orientations: two vertical layers (X- and X'-plane), two horizontal layers (Y- and Y'-plane), two layers with wires inclined with respect to the vertical axis by $+10°$(U- and U'-plane) and two others by $-10°$(V- and V'-plane). The configuration of the detector along the beam is UU', VV', XX', YY'. Every second layer is staggered by $4\,\mathrm{mm}$ (half of the cell dimension) in order to minimise track ambiguities. Each layer consists of 256 active wires made of gold plated tungsten and 257 alternating potential wires made of beryllium, with diameters of $20\,\mu\mathrm{m}$ and $100\,\mu\mathrm{m}$, respectively. To avoid sagging, two nylon wires per plane are fixed perpendicularly to the active and potential wires. The distance between every two active wires is $8\,\mathrm{mm}$. Each wire layer is enclosed between two $25\,\mu\mathrm{m}$ thick Mylar cathode foils, at a distance of $\pm 4\,\mathrm{mm}$ from the wire. This configuration defines drift cells of $8 \times 8\,\mathrm{mm}^2$, which are small enough to cope with counting rates as high as 250 kHz per wire. During operation of the detector, the active wires are kept at $0\,\mathrm{V}$, whereas both Mylar foils and potential wires are set at values close to -1700 V.

Central zones with a diameter of $28.6\,\mathrm{cm}$ and independent HV power supplies are segmented in all cathode foils. During normal operation their HV values are kept small enough (usually 900 V), which makes them blind to the high particle flux in the vicinity of the beam. The central zones are activated only for detector alignment purposes, when the beam intensity is low.

The gas used is a mixture of Ar, C_2H_6 and CF_4 with volume fractions of 45%, 45% and 10% respectively. This gas ensures a fast charge collection (drift velocity is

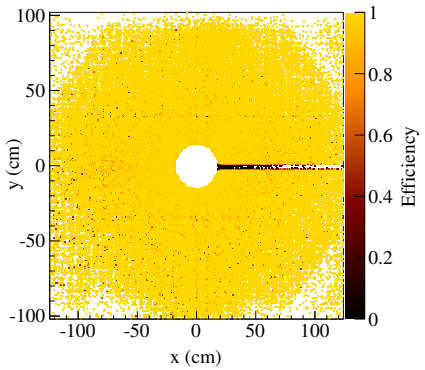

Figure 32: Two-dimensional representation of the efficiency for one of DC4 layers. The half horizontal lines with reduced efficiency indicate the position of the power supply lines of the beam killer.

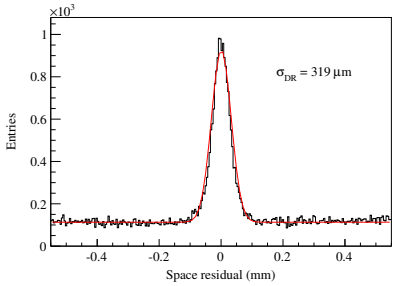

Figure 33: Double residual (see text) distribution of the DC4 chamber for one of its doublets. The quoted width is from the fit of a simple Gaussian.

$77\,\mu\mathrm{m/ns}$) while preserving a good spatial resolution. Full efficiency is reached for gain values close to 10^4, corresponding to HV settings of approximately $1750\,\mathrm{V}$.

The read-out electronics of the detector is identical to the electronics used for the already installed DC trackers. A single front-end card with 64 channels consists of eight pre-amplifier/amplifier/discriminator chips[21], called ASD8. Each ASD8 card is connected to a 64-channel F1-TDC board. The thresholds on the ASD8 card are remotely controlled. The nominal threshold is set at values between $0.8\,\mathrm{V}$ and $1.1\,\mathrm{V}$, or between 25000 and 34000 electrons.

Due to its large size, the components of the DC4 tracker are sensitive to the temperature variations in the hall. The thermal expansion or contraction of the DC4 aluminium frame may alter the nominal wire tension and degrade the detector performances. In order to minimise such effects, a specific cooling system was installed. The system consists of copper pipes running on both sides of the detector frame. The copper pipes are part of a closed secondary circuit filled with demineralised water and maintained at constant temperature. Several probes, which are installed at various locations, continuously measure the actual detector temperature. The cooling system limits the temperature variation of the frame to within 2 K.

The efficiencies of the eight DC4 planes were measured at nominal running conditions (hadron beam intensity of $5 \times 10^6/\mathrm{s}$). They were found to be in the range of 95% to 97%. Figure 32 shows the efficiency of the first vertical plane (Y1) of the DC4 chamber.

The spatial resolution of the DC4 drift chamber planes is determined by taking advantage of the staggered layers with the same orientation (doublet). The difference between the positions of the hits in the two planes, x_1 and x_2 of a doublet (double residual, or DR), is independent of the track uncertainty associated with the other planes or detectors. It includes a correction $\Delta x_{12}(\theta_{track})$, which accounts for a non perpendicular incidence of the track, i.e. a position shift when going from one plane to another.

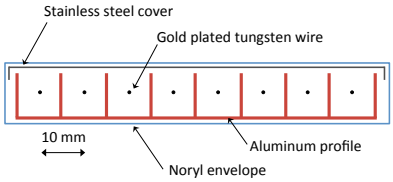

Figure 34: Sketch of a Mini Drift Tube module.

The distance between two planes being $8\,\mathrm{mm}$, this correction is small. The double residual is therefore $DR = x_1 - x_2 - \Delta x_{12}(\theta_{track})$. Figure 33 shows the double residual distribution for the X-doublet of DC4, measured under nominal beam conditions. Except for a shift of half a drift-cell length, the two layers have identical characteristics; therefore the resulting DR resolution is $\sigma^2_{DR} = \sigma^2_{x_1} + \sigma^2_{x_2} = 2\sigma^2_x$. The position resolution for a single DC4 plane is consequently $\sigma_x = 226\mu\mathrm{m}$. This result is obtained in the central region of the detector, which corresponds to about one tenth of the total detector area.

5.5. Rich Wall

The Rich Wall detector is a large-area tracker that is positioned between RICH-1 and ECAL1. The detector was built to improve the tracking accuracy at large angles ($150 < \theta < 300\,\mathrm{mrad}$) downstream of RICH-1. The additional track points measured by the detector provide a better determination of large-angle particle trajectories through RICH-1 and, as a consequence, improve the accuracy of Cherenkov ring reconstruction.

The detector has dimensions of $5.27 \times 3.91\,\mathrm{m}^2$ with a central hole of $1.02 \times 0.51\,\mathrm{m}^2$. It consists of eight planes of Mini Drift Tubes (MDT) made up of MDT modules. An MDT module consists of an eight-cell aluminium comb extrusion with a wall thickness of $0.44\,\mathrm{mm}$, which is covered on the top by a $0.15\,\mathrm{mm}$ thick stainless steel foil. Gold-plated tungsten wires of $50\,\mu\mathrm{m}$ diameter are strung in the centre of the cells. The wire pitch is $10\,\mathrm{mm}$. A Noryl® plastic envelope with a thickness of around $1\,\mathrm{mm}$ encapsulates the module. The wires are thermally glued to polyethylene plastic spacers (not shown in Fig. 34) at equal distances of $1\,\mathrm{m}$ along the length of the MDT to provide electrostatic stability. A sketch of one MDT module is shown in Fig. 34.

Figure 35 shows a front view of an X-plane. It consists of 2×25 long MDT modules (length $3910\,\mathrm{mm}$), and 2×12 short modules (length $1700\,\mathrm{mm}$) above and below the central hole. Similarly, a Y-plane comprises 2×20 long MDT modules (length $5270\,\mathrm{mm}$), and 2×6 short modules (length $2125\,\mathrm{mm}$). The eight MDT planes are arranged in four groups of two planes each, i.e. two X- or two Y-planes. The two planes within one group are staggered by $2.5\,\mathrm{mm}$. Each group is mounted onto an aluminium frame.

The readout electronics consists of front-end (FE) cards fixed on the detector frame and digital (DG) cards plugged into the FE cards. The FE cards are connected to the MDT signal wires via short shielded cables. Each FE card houses 16 MAD4 chips [22],

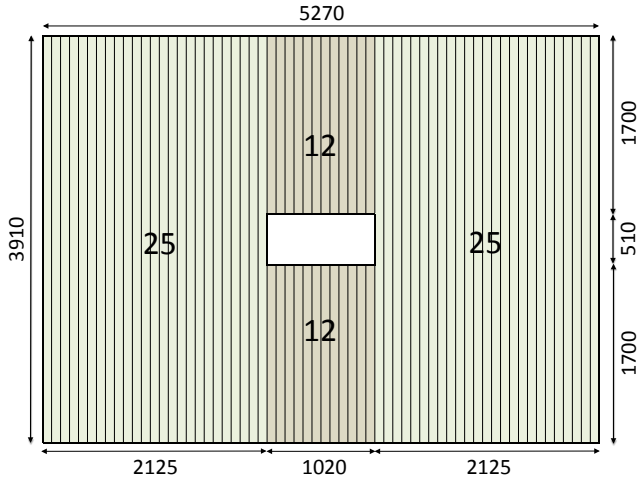

Figure 35: Front view of an X-plane of the Rich Wall detector. The large-size numbers correspond to the number of MDT modules in each sector, the small numbers indicate the dimensions in units of mm.

Figure 36: Schematic view of the Rich Wall readout chain.

a threshold digital-to-analog converter (DAC), a test-pulse generation circuit, power-supply filters and regulators. The FE card is connected to the DG cards through a high-speed card edge connector. The DG card houses eight F1 TDC [23] chips, a high-speed ($40\,\mathrm{MHz}$) HOTLink chip, and initialisation circuits. The card reads out 64 TDC channels in parallel. Two 8-bit Analog Devices DAC8841 chips per DG card are used to independently set the threshold of each MAD4 chip (common threshold for four channels) and a third one is used to generate a variable-charge test pulse. The readout chain shown in Fig. 36 is completed with FPGA-based HotGeSiCA cards (see Section 8.1) programmed in two different ways. In the first stage, the data from eight DG cards are multiplexed onto a single connection. Eight such multiplexers are then connected to the second multiplexing stage consisting of one HotGeSiCA card equipped with additional random access memory (RAM), which sends the data to the readout buffers.

The gas mixture used in the Rich Wall detector is Ar/CO_2 (70/30). For this gas

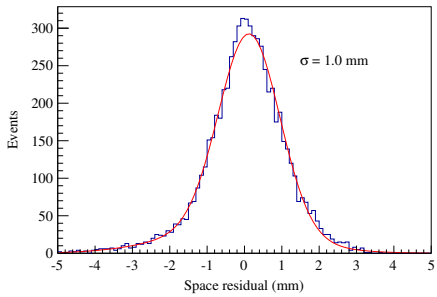

Figure 37: Rich Wall residual distribution, showing the difference between reconstructed cluster position and extrapolated track position along the axis perpendicular to the wire layer. The quoted sigma is extracted by fitting a sum of two Gaussians.

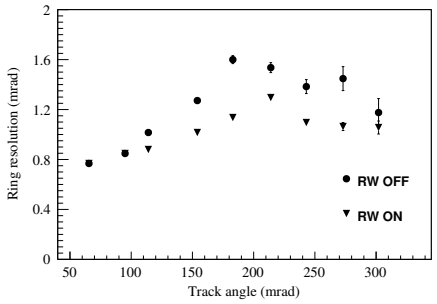

Figure 38: Resolution of the reconstructed Cherenkov ring for pions as a function of the track angle. The two different trends in the curve below and above $\sim 175\,\mathrm{mrad}$ are due to the different RICH-1 photon detector types (see Section 6.1).

mixture an operating HV of $2050\,\mathrm{V}$ was chosen. Ageing tests performed with this gas mixture have shown no degradation effects for incident charges of up to $1\,\mathrm{C}$ per cm of anode wire length. The beam-induced MDT charge, integrated over the lifetime of the COMPASS experiment, is comparable to this value. The Rich Wall detector is operated in the drift mode where the coordinate of a crossing track is calculated from the drift time in the MDT cell, using the measured RT relation. Operating the detector in the drift mode allows us to obtain a single-plane coordinate resolution of the order of $1.0\,\mathrm{mm}$, determined by fitting a sum of two Gaussians to the residual distribution (Fig. 37). During operation the detector has shown a stable single-plane efficiency of 90–91%.

The beneficial effect of the Rich Wall detector on the Cherenkov ring reconstruction in RICH-1 is shown in Fig. 38. In the polar angular range 150–$300\,\mathrm{mrad}$ the Cherenkov ring resolution is improved by 20% on average.

6. Particle Identification Detectors

The hadron physics programme at COMPASS requires the reconstruction of final states with charged and/or neutral particles in a large angular range. Several types of particle identification detectors (PID) are used to achieve this goal (see Fig. 3). Charged pions and kaons, as well as protons, with momenta of up to $50\,\mathrm{GeV}/c$ are identified in the RICH-1 detector, while their energy is measured in the two hadron calorimeters, HCAL1 and HCAL2. Photons emitted during the interaction and decay photons are detected in two electromagnetic calorimeters, ECAL1 and ECAL2. Scattered muons are identified in the two muon identification systems, consisting of drift tubes detectors (MW1 and MW2) and absorber walls made of iron (Muon Filter 1) or concrete (Muon Filter 2).

Since the publication of Ref. [1], the PID part of the setup was significantly upgraded. New photon detectors were installed in the central region of RICH-1, and a new readout system was implemented in its peripheral region. The new ECAL1 calorimeter was added, which extends the acceptance for photon detection to large angles. The ECAL2 calorimeter was upgraded with radiation-hard Shashlik modules in its central region and with fully pipelined electronics. For both calorimeters, the calibration procedure and the monitoring of the individual modules were significantly improved. The hadron calorimeters and the muon identification systems remained unchanged since their description in Ref. [1] and are hence not discussed here.

6.1. The RICH-1 detector

The RICH-1 detector [24] covers the horizontal and vertical angular acceptances downstream of the SM1 magnet (250 mrad$\times$180 mrad). Its $3\,\mathrm{m}$ long vessel is filled with C_4F_{10} gas as a radiator [25]. The refractive index of the radiator material corresponds to Cherenkov thresholds of about 2.5, 9, and $17\,\mathrm{GeV}/c$ for pions, kaons, and protons, respectively. A steel pipe with a radius of $5\,\mathrm{cm}$ and thickness of $0.15\,\mathrm{mm}$ separates the vessel from the beam path. Cherenkov photons produced along the path of a hadron are reflected by a $21\,\mathrm{m}^2$ surface that consists of 116 spherical UV mirror elements that are grouped into two spherical surfaces [26]. The mirrors are designed such that the photons are focused onto two arrays of photon detectors (see Fig. 39), located outside of the spectrometer acceptance.

6.1.1. Upgrade

Until 2004, Cherenkov photons were detected in Multiwire Proportional Chambers (MWPC) equipped with solid-state CsI photocathodes that limit the MWPC operation to gains below 5×10^4. The first stage of the electronics readout system [27] was characterised by a long integration time; this was a limiting factor in the COMPASS environment, where a high-rate uncorrelated background is present due to the large muon beam halo. High rates and large correlated background are also typical for measurements with a hadron beam. In addition, the long base-line restoration time (about $3.5\,\mu\mathrm{s}$) generated a non-negligible dead time.

In order to overcome these limitations, a major upgrade of the RICH-1 detector was undertaken. Details can be found in Refs [28–30]. Two different technologies

were chosen in order to minimise the overall cost of the project. In the peripheral regions that cover 75% of the photo-detection surface, where the level of the uncorrelated background is small, the MWPC/CsI photon detectors were kept. However, their front-end electronics was replaced by a new system [28] that is based on the 128 channel APV25 chip [11]. The new system provides two major improvements. First, it reduces the effective time window from $3\,\mu\mathrm{s}$ to $400\,\mathrm{ns}$ and decreases the dead-time losses of the readout system to values close to 5%. Second, the APV25 chip performs a triple sampling of the MWPC signal, which results in a much improved time resolution and in an increase in the signal-to-background ratio [28] from 0.35 with the old system to 2.13 with the new one.

The central region of RICH-1, which covers 25% of the photo-detection surface, is instrumented with a detection system based on Multi-Anode PhotoMultiplier Tubes (MAPMTs) [30]. The MAPMTs are coupled to individual telescopes of fused silica lenses which consist of a prismatic field lens followed by a concentrator lens, thereby enlarging the effective active area of the photon detectors by a factor of seven. The effective pad size that results from the MAPMT pixel-size and the lens telescope magnification is about $12 \times 12\,\mathrm{mm}^2$. The new system detects about four times more Cherenkov photons than the old one and reaches values as high as 60 photons per ring. The MAPMT detectors are intrinsically fast and have time resolutions better than $1\,\mathrm{ns}$. They are coupled to a readout system [29] based on the MAD4 high sensitivity amplifier/discriminators and the standard COMPASS F1 TDCs.

6.1.2. Characterisation

A dedicated software package, called RICHONE [31], was developed for the RICH-1 data reduction. It performs pattern recognition and particle identification, and characterises the detector response. Figure 39 shows an example of a RICH-1 event in the hadron beam environment showing many rings in the central detectors. The time windows applied are the same as used in data reconstruction, namely $10\,\mathrm{ns}$ for the MAPMT part and $250\,\mathrm{ns}$ in the MWPC part. Each visible ring belongs to a detected particle. A major difference between the use of RICH-1 with muon and with hadron beam is the different particle population in the events, which is due to the different event multiplicity and particle phase space. The muon beam is characterised by a wide halo, which extends over all photon detectors and has a flux comparable to that of the focused beam. The Cherenkov photons that are emitted by the halo particles travelling parallel to the beam are focused into the central zone of the RICH-1 photon detectors, which results in a large background. The hadron beam can be better focused and has hence much less halo. Nevertheless, due to the higher interaction rate in hadron scattering, a large number of particles is emitted at small polar angles, i.e. in the very forward region. These particles also populate the central region of the RICH-1 photon detectors. A map of the integrated hit distribution in the central part of the RICH-1 photon detectors is shown in Fig. 40 for data taken with muon and positive hadron beam. The distributions are normalised to the number of entries and the same scale is used for the comparison. Both distributions show large occupancies for photons emitted from particles traversing RICH-1 under small polar angles. The ring images in the muon environment have more overlap since they are mostly produced by the parallel halo particles, while in the hadron case the particles have a slightly broader polar angle

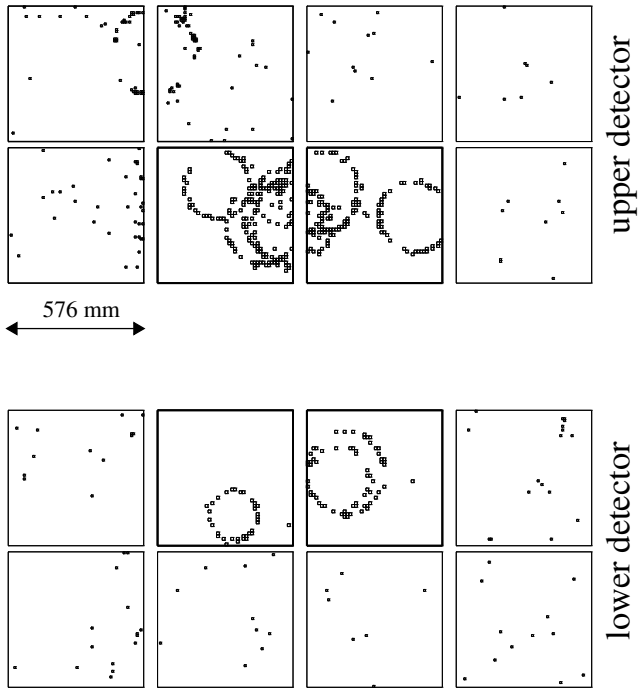

Figure 39: A typical event display during hadron data taking. The 16 squares represent the detector areas; the four central ones are equipped with MAPMTs. The small squares represent the hits detected in the photon detectors.

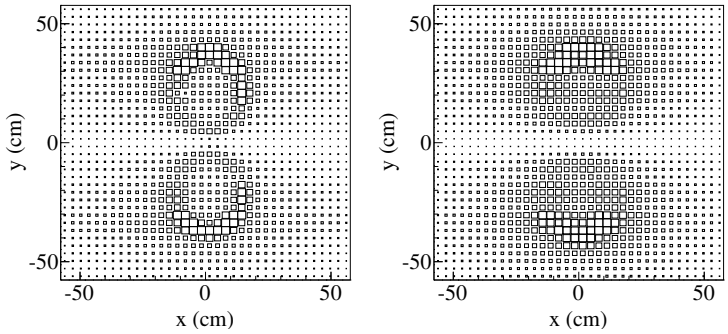

Figure 40: Two-dimensional hit distributions in the central part of the RICH-1 photon detectors for (left) data taken with a muon beam and (right) data taken with a positive hadron beam.

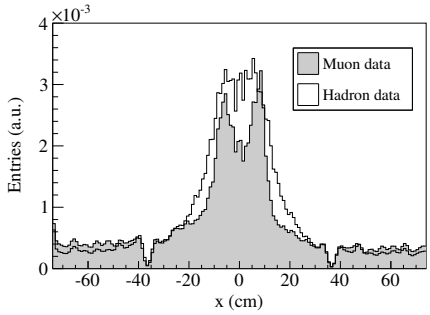

Figure 41: Horizontal axis projection of the integrated hit distributions for the lower photon detectors. Both central and peripheral parts of RICH-1 are included. The shaded histogram refers to the muon environment, the open to the hadron one. The small dips in the hit distributions correspond to the dead zones between the detector parts equipped with MAPMTs and with MWPCs.

distribution. Figure 41 shows the projection of the hit distribution in the lower photon detectors onto the horizontal axis, for both the muon and the hadron environment. Even if the origin of the background is different in the two environments, the overall background distributions are similar. The same was observed when changing to another hadron beam or target, so that the general properties of the detector response remain the same as the ones measured with a muon beam [31]. The uncertainties in the reconstructed angle of the individual Cherenkov photons is $2\,\mathrm{mrad}$ in the central region and $2.5\,\mathrm{mrad}$ in the periphery, while the uncertainties in the determination of the mean Cherenkov angle (ring angle) are $0.3\,\mathrm{mrad}$ and $1.6\,\mathrm{mrad}$, respectively. These resolutions allow pion-kaon separation at 95% confidence level for momenta up to $45\,\mathrm{GeV}/c$. The average number of photons per ring at saturation, i.e. for $\beta \to 1$, is 56 in the central and 14 in the peripheral region. The dependence of the mean number of detected photons per ring versus the corresponding Cherenkov angle is shown in Fig. 42 for the detectors equipped with MAPMTs.

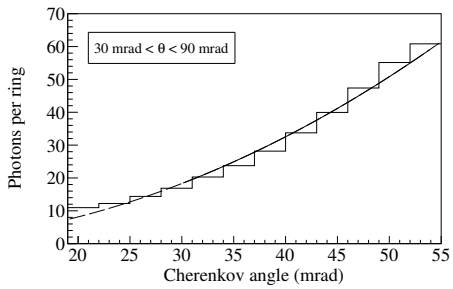

Figure 42: Mean number of detected photons per reconstructed ring as a function of the corresponding Cherenkov angle $\theta_{\rm Ch}$ in the central region of the RICH-1 detector for track angles θ between $30\,\mathrm{mrad}$ and $90\,\mathrm{mrad}$. The line is a fit with the functional form $N = N_0 \sin^2(\theta_{\rm Ch})$.

Part of the data taking in 2009 was devoted to a test of the Primakoff measurement. For this test, RICH-1 was filled with N_2 gas in order to have a smaller material budget in the acceptance region. The response is largely different in this case as the refractive index of N_2 is lower than that of C_4F_{10}. In particular, the number of emitted photons at saturation is expected to be lower by a factor of 4.8 for the N_2 radiator. The number of detected photons is then sufficient to allow for particle identification only in the central part of RICH-1, which is equipped with MAPMTs. In this region, the average number of photons per ring at saturation is 11.7, which has to be compared with 56 for the C_4F_{10} radiator (Fig. 42). The lower number of detected photons leads to an uncertainty in the determination of the ring angle, which is larger by a factor 2.2 with respect to the operation with the C_4F_{10} radiator. Nevertheless, the upper momentum limit for pion-kaon separation is very similar for the two radiators as the poorer resolution of N_2 is compensated by a larger difference between the corresponding Cherenkov angles. The thresholds of the Cherenkov effect are 5.6, 20, $38\,\mathrm{GeV}/c$ for pions, kaons, and protons respectively. Thus, in comparison to the values for C_4F_{10} quoted above, the momentum range for pion-kaon separation is severely reduced.

6.2. Electromagnetic calorimeter ECAL1

The ECAL1 calorimeter is part of the Large Angle Spectrometer. It consists of 1500 lead glass (LG) modules. For reasons of availability and cost, three types with different dimensions are used, see Table 4. The calorimeter ECAL1 has a width of $3.97\,\mathrm{m}$ and a height of $2.86\,\mathrm{m}$, which corresponds to the angular acceptance for photons coming from the centre of the liquid hydrogen target of $37\,\mathrm{mrad}$ to $136\,\mathrm{mrad}$ in the horizontal direction and of $21\,\mathrm{mrad}$ to $98\,\mathrm{mrad}$ in the vertical direction. The central hole has a size of $1.07 \times 0.61\,\mathrm{m}^2$. The ECAL1 calorimeter is installed on a motorised platform that allows horizontal and vertical movements orthogonal to the beam direction, which is used mainly for calibration purposes.

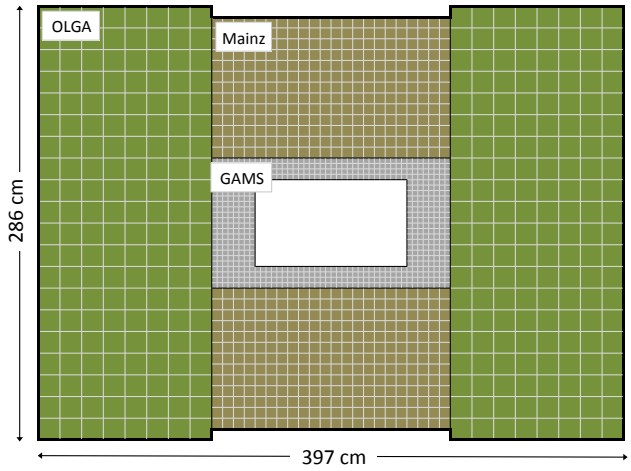

Figure 43: Configuration of ECAL1. The central area is equipped with GAMS modules. The MAINZ modules are installed above and below the GAMS area. The OLGA modules cover the outer left and right regions.

Table 4: Parameters of the ECAL1 lead glass modules.

Parameter	Units	GAMS	MAINZ	OLGA
LG type		TF1	SF57	SF5
Density	g/cm^3	3.86	5.51	4.08
Rad. length (X_0)	cm	2.74	1.55	2.55
Total thickness	X_0	16.4	23.3	18.5
Moliere radius	cm	4.7	2.61	4.3
Refractive index		1.65	1.89	1.67
Length	cm	45	36	47
Surface	cm^2	3.83×3.83	7.5×7.5	14.1×14.1
PMT type		FEU-84-3	EMI 9236KB	XP2050

6.2.1. Design and electronics

A front view of the ECAL1 calorimeter is shown in Fig. 43. The central part of ECAL1 consists of 608 LG modules of transverse dimensions 3.83×3.83 cm^2, which are denoted GAMS modules [32]. They are arranged in a 44×24 matrix with its central 28×16 array left empty. Above and below this central part, two 22×13 matrices of "MAINZ" modules [33] are installed, which contain in total 572 LG modules. One MAINZ module has the size of nearly four GAMS modules. In order to compensate for the small difference in size, 1.6 mm vertical gaps have been left between all columns of MAINZ modules, except the two central columns. On both sides of the central columns, the nearest two gaps are filled with iron plates. The two outermost parts of ECAL1 consist of two matrices of 8×20 large-size "OLGA" modules [34]. Each OLGA module has the size of nearly four MAINZ modules. Table 4 summarises all relevant parameters of the LG modules used. It also contains the types of PMTs that detect their Cherenkov light. The analogue signals coming from the PMTs pass through shaper modules. The shaper modules preserve the integral value of a signal and enlarge its width to 80 ns FWHM in order to match with the SADC sampling rate of 77.76 million samples per second.

In the offline event reconstruction the SADC information is used to extract the amplitude and time of a signal relative to the trigger time. After subtracting the ADC-baseline that is determined for even and odd samples separately averaging the first 3 samples for each hit, the separation between even and odd samples is implemented in order to account for interleaved readout as described in Section 6.3.1. The amplitude of a signal is determined as the difference between its absolute maximum and the calculated baseline. The hit time is determined for each calorimeter module by selecting those SADC samples with amplitudes A_n and A_{n+1}, which surround the position in time that represents one-half of the maximum amplitude A_{max}. In order to improve timing accuracy, the time at which the signal is reaching 50% of A_{max} is derived from an interpolation between the samples n and $n+1$:

$$t = \left(n + \frac{A_{max}/2 - A_n}{A_{n+1} - A_n} \right) \times 12.86\,\text{ns}\,, \tag{1}$$

where 12.86 ns is the sampling period. For photon energies larger than 1 GeV the

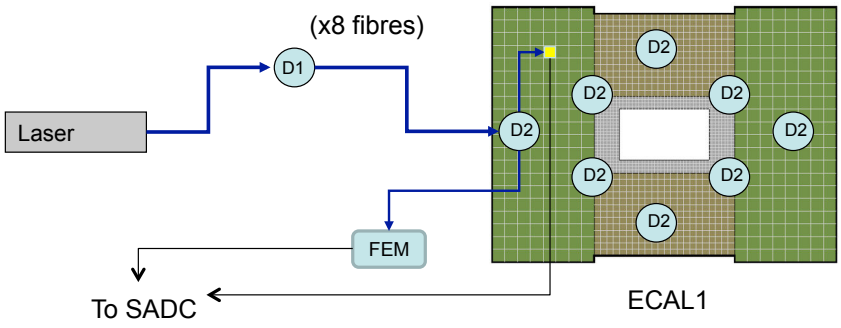

Figure 44: Schematic view of the LASER monitoring system for ECAL1. The laser beam is distributed to the ECAL1 modules using one primary (D1) and eight secondary (D2) light diffusion spheres. For clarity, only one of the 8 primary fibres dispatching the light to D2, only one of the secondary 1500 fibres transmitting it to the LG modules, and only one of the 8 front-end-monitoring (FEM) modules are explicitly shown.

resulting time resolution is about 1 ns.

6.2.2. Calibration and monitoring

For the calibration of ECAL1 LG modules the field of SM1 is set to zero. A 15 GeV electron beam is used, which is a compromise that accounts for the different dynamic ranges of the three types of modules. An automatised calibration procedure changes the position of the calorimeter between two consecutive spills, so that every module is exposed during calibration. Up to several thousands electrons per module are collected within each spill. The total cluster charge deposited, i.e. the sum of the charges of the module being calibrated and its neighbouring modules, is compared to the incident electron energy. Several iterations are necessary to determine the HV settings for all modules.

The calibration coefficients, which relate the charge measured by each SADC to the energy deposited in the corresponding module, are calculated taking into consideration the energy range of the photons detected in that module during the experiment. Since the energy of the photons decreases as the angle between the photon direction and the beam axis increases, three different HV settings are applied. For the incident beam energy of 190 GeV, the settings are chosen such that the corresponding dynamic ranges for the three types of modules extend up to 60, 30, and 20 GeV for GAMS, MAINZ and OLGA modules. The whole calibration procedure is applied once or twice per data taking period of several months.

In order to control the light collection efficiency and the photomultiplier gains of all 1500 LG modules, the ECAL1 calorimeter is equipped with a dedicated monitoring system that is based on the design of Ref. [35]. It uses a single laser source, namely a Minilite-1 model from Continuum [36]. The use of a single light source allows the detection of possible light collection or PMT instabilities individually in each ECAL1

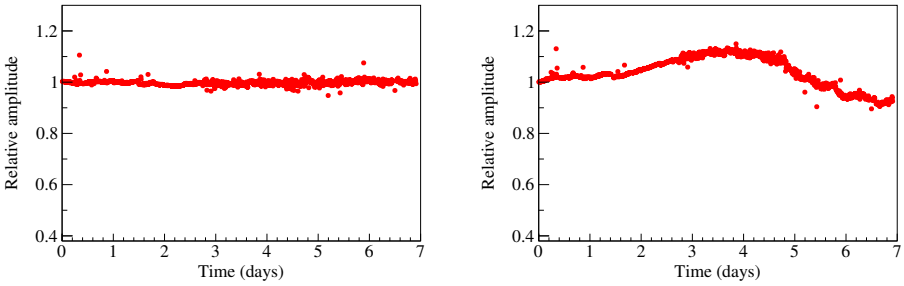

Figure 45: ECAL1 module responses as monitored during a period of one week for (left) a stable module and (right) an unstable module. The vertical scale is normalised to the SADC charge measured in the beginning of the period.

channel. The laser light is transmitted to the LG modules through one primary and eight secondary optical fibre bundles. The fibre bundles are interconnected using light diffusers that guarantee a uniform distribution of the light in the fibres. Each secondary bundle consists of 240 fibres from which between 160 and 200 fibres are connected to the LG modules.

A simplified drawing of the monitoring system is shown in Fig. 44. The laser injects $532\,\mathrm{nm}$ light pulses with $5\,\mathrm{ns}$ FWHM into all calorimeter modules at a frequency of $1\,\mathrm{Hz}$ in the SPS inter-spill periods. The laser energy per pulse is tuned to an amount that matches the photomultiplier signal amplitudes. Since the light output of the laser source itself may vary between two consecutive pulses, an independent reference measurement of the pulse amplitudes is required. Nineteen fibres, to make the available light signal strong enough, from each secondary bundle are plugged into eight reference photodiodes. Each photodiode is connected to a temperature-stabilised electronics circuitry [35], which is enclosed in a Front-End Monitoring (FEM) module. The eight FEM signals are read out by the same SADC electronics as the calorimeter modules, thus providing an eight-fold normalisation of the laser pulse amplitude. The amplitude of the signals from the LG modules is determined as the peak value of the SADC samples as obtained after pedestal subtraction.

The recorded laser monitoring amplitudes are used to correct the responses of all ECAL1 modules on a run-by-run basis. The electron beam calibration provides the starting values of the calibration coefficients C^i. These coefficients convert the photomultiplier signal amplitude from ADC channels to GeV using

$$A^i_{GeV}(t) \;=\; A^i_{ADC}(t) \times C^i \times \frac{L^i(t)}{L^i(0)}\,. \tag{2}$$

Here, $A^i_{ADC}(t)$ is the ADC amplitude for the module i measured at a given time t, $L^i(t)$ is the ADC amplitude of the monitoring amplitude of the module i at time t, and $L^i(0)$ is the monitoring amplitude of the same module, but recorded during the electron beam calibration run. The time t is taken as the time of the run, for which the correction is to be applied. A display of two LG modules (a good one and an unstable one) as a function of time is shown in Fig. 45.

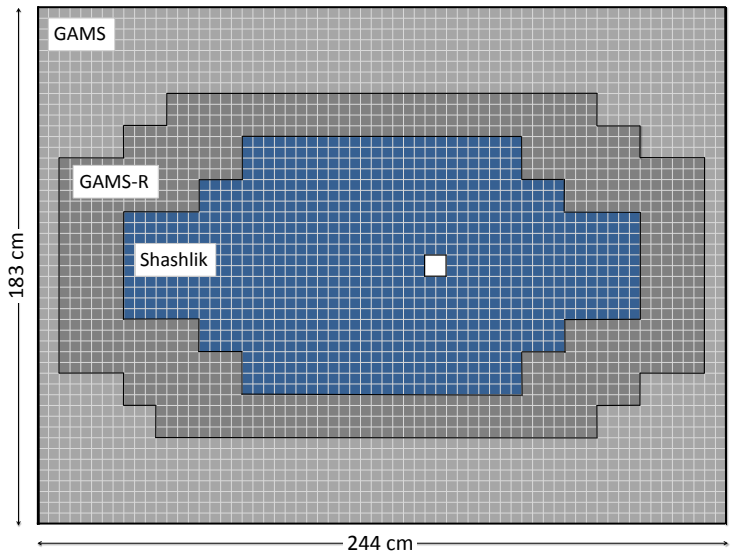

Figure 46: Configuration of ECAL2. The outer and intermediate regions are equipped with GAMS and radiation-hardened GAMS modules respectively. The inner region is equipped with Shashlik sampling modules. The transverse sizes of all three types of modules are identical. The central hole of 2×2 modules can be seen as a white spot.

6.3. Electromagnetic calorimeter ECAL2

ECAL2 is a part of the Small Angle Spectrometer. It consists of 3068 calorimeter modules of three different types, all with the same transverse dimensions ($3.83 \times 3.83\,\mathrm{cm}^2$). With its dimensions of $2.44 \times 1.83\,\mathrm{m}^2$, ECAL2 covers angular ranges between $1.3\,\mathrm{mrad}$ and $39\,\mathrm{mrad}$ in the horizontal plane and between $1.3\,\mathrm{mrad}$ and $29\,\mathrm{mrad}$ in the vertical plane. In both planes the angular ranges are slightly larger than the corresponding angular ranges of both ECAL1 (Section 6.2) and the hadron calorimeter HCAL1. Accordingly, the peripheral rows and columns of ECAL2 are not used; for the corresponding ECAL2 angles the photons from the target are either detected in ECAL1 or absorbed in HCAL1. ECAL2 is installed on a motorised platform allowing movements in both horizontal and vertical directions.

6.3.1. Design and electronics

The ECAL2 modules are arranged in a 64×48 matrix, as shown in Fig. 46. For data taking with hadron beams, its central hole with respect to the nominal beam directions is set to 2×2 modules. The central hole of the HCAL2 calorimeter is set accordingly to $10 \times 10\,\mathrm{cm}^2$. The outermost part of ECAL2 is equipped with 1332 TF1 lead glass [32] modules, which are identical to the GAMS modules used for ECAL1. The intermediate part of ECAL2 is filled with 848 radiation-hardened modules (GAMS-R) made out of

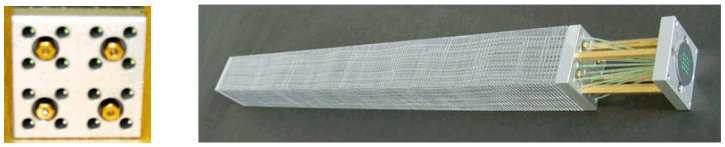

Figure 47: Photographs of a Shashlik-type calorimeter module. Left part: the upstream face of the module with its four central rods and 16 light fibres. Right part: the module itself with the fibres guide at the downstream face.

TF101 material [37]. This material is a standard TF1 type LG, which is enriched with 0.2% of cerium. The innermost part is equipped with 888 Shashlik type modules (see Fig. 47). The 39 cm long Shashlik modules are composed of 154 double layers, each consisting of a $0.8\,\mathrm{mm}$ thick lead plate and of a $1.55\,\mathrm{mm}$ thick scintillator plate. The photons from the Shashlik modules are collected by 16 wavelength-shifting light fibres and guided onto FEU-84-3 photomultipliers.

The different ECAL2 modules have identical transverse dimensions, but different radiation hardness properties. Calculations for the present ECAL2 configuration have shown that with the COMPASS nominal hadron beam intensity and duty cycle the most exposed modules, i.e. those located closest to the beam, would stand radiation doses corresponding to several years of data taking for GAMS and GAMS-R and nearly 20 years for Shashlik, without significant degradation of their response.

The photomultiplier signals coming from the 3068 ECAL2 modules are first transferred to a shaper, which increases the signal width to $120\,\mathrm{ns}$ FWHM. The signals are then digitised by sampling ADCs. The ECAL2 readout was upgraded with a new sampling ADC system, which provides a dynamic range of 12 bit and allows more elaborate data processing. The basic building block is a compact Mezzanine Sampling ADC card (MSADC), which performs a digitisation of the 16 analogue input channels at 77.76 million cycles per second, with two interleaved multichannel ADCs [38]. Data processing is implemented by a Xilinx Virtex4 FPGA [18]. The MSADC firmware includes a digital ring buffer to compensate the trigger latency, a pipelined logic for pedestal correction, zero suppression and data formatting. In addition, an independent processing chain is implemented on the FPGA to determine time and amplitude information for the calorimeter trigger described in Section 7.5. As shown in Fig. 48, four MSADCs are combined on a 9U VME carrier card, which merges the data from 64 calorimeter channels and provides a serial 40 Mbit/s HOTLink interface to the HotGeSiCA multiplexer modules in the next readout stage. In order to reduce the power dissipation, all MSADC supply voltages are generated centrally on the carrier card with DC/DC converters. The resulting noise on the MSADC channels is below 1.5 least significant bit.

The information from the MSADCs is also used to calculate the time for each event. For each ECAL2 module, the algorithm interpolates between the times of the two samples around the one-half value of the maximum sampled amplitude (see Section 6.2). The time resolution for ECAL2 is shown in Fig. 49. For energies higher than $2\,\mathrm{GeV}$, resolutions of 1 ns or better are achieved.

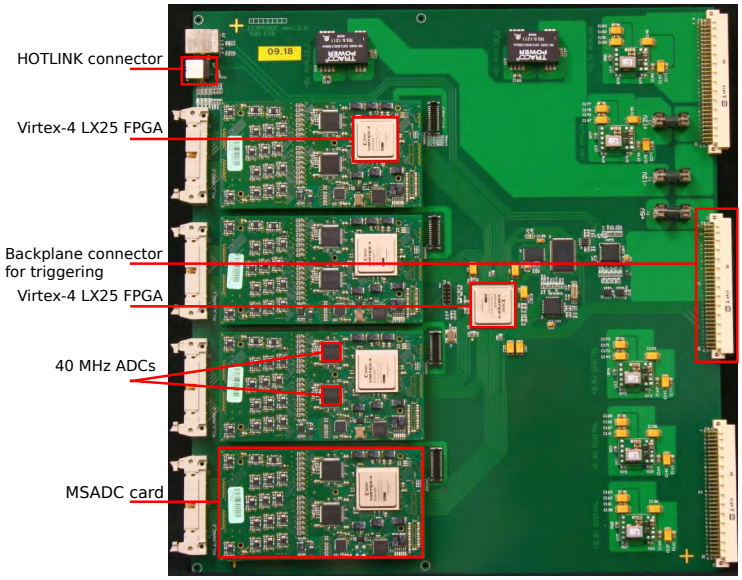

Figure 48: VME carrier card with four mounted MSADC modules.

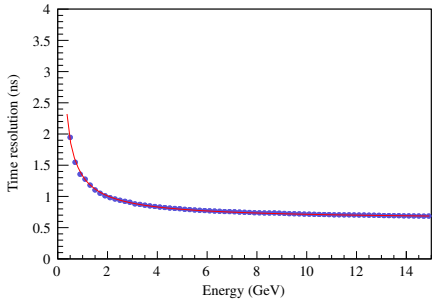

Figure 49: Standard deviation σ for the ECAL2 time resolution as a function of the photon energy E. The solid curve is a fit to the data points using the expression: $\sigma^2(E) = 1.13/E + 0.22/E^2 + 0.39$.

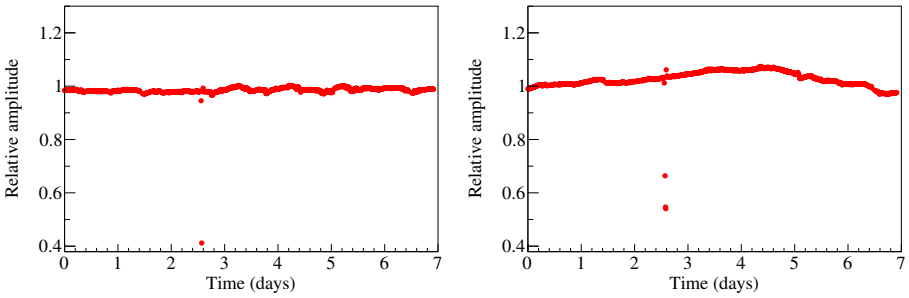

Figure 50: ECAL2 module responses as monitored during a period of one week for (left) a stable module and (right) an unstable module. The vertical scale is normalised to the SADC charge measured in the beginning of the period.

6.3.2. Calibration and monitoring

The ECAL2 calorimeter is calibrated by exposing all its modules to a $40\,\mathrm{GeV}$ electron beam. Apart from different geometry and different number of modules, the calibration procedure is identical to that used for ECAL1 (see Section 6.2.2). The charge deposited in each cluster of LG modules (as measured in the MSADCs) is calculated and compared to the incident electron energy. After the data for all modules are collected, few iterations are necessary to determine the calibration coefficients for all Shashlik and LG modules. The final HV settings are calculated after taking into account the energy ranges of the photons detected in the different parts of ECAL2. The high voltages of the PMTs of the innermost 16×16 modules are set to measure energies of up to $200\,\mathrm{GeV}$. In the surrounding part, which represents a 48×48 matrix, the maximal energy is set at $150\,\mathrm{GeV}$. Finally, in the two outermost parts with 8×48 modules each, the PMTs are set to detect energies of up to $60\,\mathrm{GeV}$.

The time stability of the ECAL2 calibration is monitored using a LED-based monitoring system. This light-distribution system consists of 30 fibre bundles, where the number of fibres varies between 64 and 140 per bundle. Each bundle is illuminated by six simultaneously activated LEDs. The combined use of six LEDs increases the available light intensity and minimises possible intensity fluctuations by averaging out the individual LED instabilities. The system is activated using a calibration trigger with a frequency of $1\,\mathrm{Hz}$. A display of two ECAL2 modules with a stable and with an unstable response is shown in Fig. 50. The information from the monitoring system is used to correct short and long term drifts of individual cells on a spill by spill basis.

7. Trigger

The COMPASS trigger system for hadron beams is designed to select events that carry all the information needed for exclusive measurements. A fast response is needed to provide the time reference for the readout of all detectors. A physics trigger consists of three subsystems: beam-defining elements to select beam particles crossing the target, veto detectors to reject events containing particles produced outside of the target or outside of the spectrometer acceptance, and specific detector systems that account

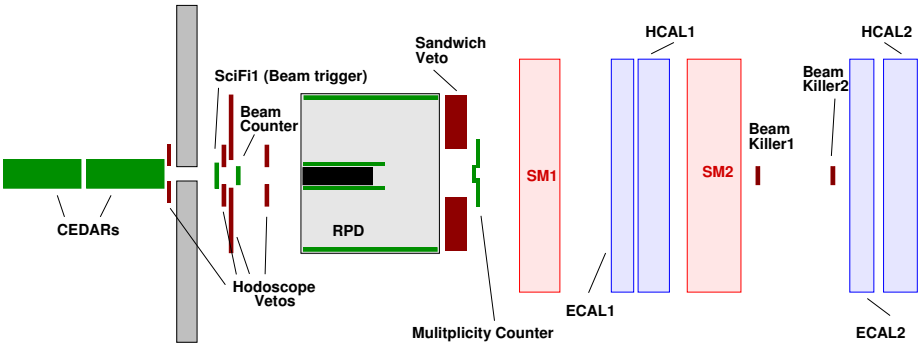

Figure 51: Arrangement of trigger elements in the spectrometer (schematic side view, not to scale).

for the particular physics case. The latter are: i) the proton trigger (Section 7.3) that is used for measurements of diffractive scattering and central production processes with momentum transfers $t < -0.07\,\mathrm{GeV}^2/c^2$ (see Section 4.3), ii) the multiplicity trigger that completes the coverage in t for reactions with higher charged track multiplicities (Section 7.4), and the calorimeter trigger (Section 7.5) that is used for Primakoff data taking. Figure 51 shows schematically the location of the trigger elements in the spectrometer.

7.1. Beam Trigger

The beam trigger selects incoming beam particles and is used to define the reference time of an event. In addition, it reduces the geometric acceptance of the beam in the transverse plane to match the target geometry. It consists of a coincidence of a scintillating fibre detector, SciFi1, with a beam counter. SciFi1 is located 7 m upstream of the liquid hydrogen target. It has one vertical and one horizontal plane. Each plane is read out by six multi-anode photomultiplier tubes (PMT) with 16 channels each. In addition, the PMTs are read out at the last dynode stage, thus providing six analogue sums for each of two planes of the detector.

The beam counter is a small scintillator disc that is located 50 cm downstream of SciFi1. It has a diameter of 3.2 cm, a thickness of 4 mm, and is centred at the beam. It is surrounded by a thin, black PVC tube covered inside by aluminised Mylar foil with an internal reflection of better than 92%. A 35 cm long tube used as an air light-guide is connected to a single EMI 9813KB PMT. The PMT is equipped with a voltage divider that stands beam rates of up to 10 MHz. The efficiency of the beam counter was measured to be 99.5% all over the surface of the disk, as shown in Fig. 52.

The beam trigger is defined by the coincidence of the beam counter signal and the logical OR of the 6 analogue sums of the SciFi1 X plane. The time resolution is measured to be 450 ps $\pm$ 50 ps (Fig. 53). It is used as a time reference of the trigger system.

7.2. Veto Detectors

The veto system consists of two scintillation counters ("beam killers"), a 'sandwich" veto detector (see Section 4.4) and a hodoscope veto system. It inhibits false

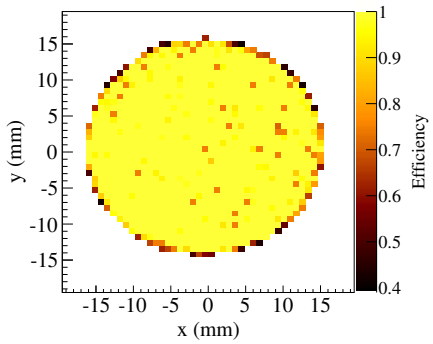

Figure 52: Beam counter efficiency distribution in transverse coordinates.

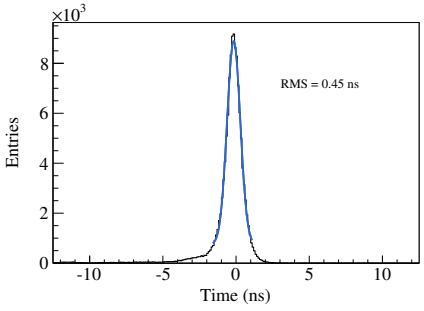

Figure 53: Time residual of the beam trigger.

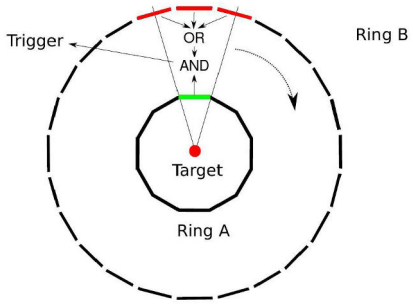

Figure 54: Allowed combinations for target pointing in the RPD part of the proton trigger.

physics triggers. The overall dead time of the veto system was measured to be 13%-16% for the nominal beam intensity of $5 \cdot 10^6\,\mathrm{s}^{-1}$. For Primakoff data taking, it is reduced to 8%-10% due to the lower beam intensity.

7.2.1. Beam killers

Two scintillating counters are positioned along the beam axis of the spectrometer at z =+25 m (BK1) and z =+33 m (BK2). Both counters have a diameter of 3.5 cm and a thickness of 0.5 cm. Their function is to inhibit a trigger signal coming from non-interacting beam particles. The use of the beam killers introduces an angular cut-off of 0.97 mrad with respect to the nominal beam axis. Including the beam killers in the diffractive trigger (see Table 5), reduces its trigger rate by about a factor of 2.

7.2.2. Sandwich Veto Detector

A Sandwich veto detector (described in Section 4.4) is used to veto charged and neutral particles that are detected outside of the angular acceptance of the spectrometer and the RPD. Such particles are dominantly produced in inelastic, non-diffractive reactions or in reactions in which the target protons are diffractively excited. Including the Sandwich veto in the trigger improves the purity of the physics triggers by a factor of about 3.5.

7.2.3. Hodoscope Veto System

The hodoscope veto system is the same as the one used for the muon programme. It consists of three parts: a beam line hodoscope veto system (V_{BL}) installed at $z = -20$ m, a Veto1 system located at $z = -7.5$ m, and a Veto2 counter at $z = -1.5$ m. A detailed description can be found in Refs [1] and [39]. The hodoscope veto system removes events with large multiplicities in the RPD.

7.3. Proton trigger

The proton trigger selects events with recoiling protons from the target. The RPD (described in Section 4.3) information is used for two purposes: target pointing and discrimination of protons from pions and delta-electrons by measuring the energy loss

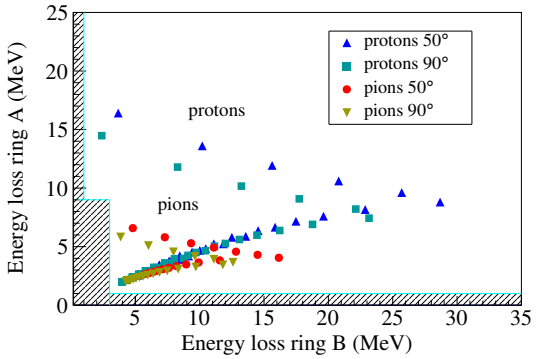

Figure 55: Correlation between the energy losses of protons and pions traversing ring A and stopping (or traversing) ring B of the RPD. For each particle type the minimum and the maximum polar angles ($50°$ and $90°$) are shown. The shaded area corresponds to the region rejected by the trigger logic.

in each ring of the RPD. Target pointing is implemented by allowing only for combinations, where hits in one scintillator of the inner ring are followed by a signal in one of the three corresponding outer ring scintillators, as shown in Fig. 54.

For a particle traversing the RPD, its energy losses in the inner and in the outer rings are strongly correlated. This is used to reject electrons coming from the target as well as part of the low-energy pions. Fig. 55 shows the calculated energy losses for both protons and pions, and for the minimum and maximum polar angles ($50°$ and $90°$) of the RPD acceptance (see Section 4.3). The area to be rejected is defined using the two levels of discriminator thresholds in both rings. The coincidence of low-threshold signals for upstream and downstream PMTs of the inner (outer) ring is denoted by A_i^{Low} (B_j^{Low}), where i and j are the respective scintillator elements. Similarly, the coincidence of the two high-threshold signals is denoted by the superscript "High". The trigger logic function for recoil protons has the following expression:

$$RPD = \bigvee_{i=1}^{12} A_{i,down}^{Low} \wedge \bigvee_{j=2i-1}^{2i+1} \left(A_i^{Low} B_j^{High} \vee A_i^{High} B_j^{Low} \right). \qquad (3)$$

Here, the signals from the downstream PMTs of the inner ring, $A_{i,down}^{Low}$, are used to minimise the time jitter with respect to the beam trigger. The trigger logic is set to reject the electrons that cross both rings as well as pions that cross ring A but leave less than few MeV in ring B. In Fig. 55, the region rejected by the proton trigger is indicated by the shaded area.

In order to be able to measure the time-of-flight of all recoil protons, irrespective of their velocities, a large time window of 50 ns is required for the coincidence between any of the inner-ring downstream PMTs with the geometrically allowed outer-ring PMTs. The trigger logic function (3) is implemented in a single FPGA module that is fed by the logic signals from all PMTs of the RPD.

7.4. Multiplicity Trigger

The multiplicity triggers were built to extend the measurements to events with momentum transfers $-t$ smaller than $-t < 0.07\,\mathrm{GeV}^2/c^2$ that are outside the acceptance of the proton trigger. It uses the multiplicity counter to estimate the charged-particle multiplicities in the beam region or tag events with at least one (or two, see Table 5) track at large angles.

The multiplicity counter (Fig. 56) consists of 12 trapezoidally shaped scintillator slabs with a central hole of $20\,\mathrm{mm}$ diameter. It covers the charged-particle acceptance of the spectrometer at 1.7 m, which projects to a disk with a radius of $310\,\mathrm{mm}$. The light is read out by one photomultiplier per slab. The counter was upgraded in 2009 with a scintillator disk with a diameter of $32\,\mathrm{mm}$, which is centered at the hole and is read out by two photomultipliers. In order to minimise photon conversion in the active area, all scintillators have a thickness of $3\,\mathrm{mm}$, which corresponds to $0.71\,\%$ of a radiation length. The photomultipliers for the inner disk are connected through an $83\,\mathrm{cm}$ long air light guide made of a tube skeleton of $15\,\mu\mathrm{m}$ aluminised Mylar inside a $150\,\mu\mathrm{m}$ thick plastic coating.

The two components of the multiplicity detector, the outer and the inner counters, are used to build two independent triggers, MT1 and MT2. The MT1 multiplicity trigger requires one hit or more in each element of the outer multiplicity counter. For this purpose, the threshold per element is set to reject noise only, thereby selecting charged particle multiplicities of one or larger. A logical OR of all elements is then used as the trigger signal. The MT2 multiplicity trigger requires an energy deposit corresponding to 1.6 MIPs[10] or higher in the inner counter. Data were also taken in stricter conditions for both MT1 and MT2. For MT1 this was achieved by using a multiplicity logic instead of the logical OR, thereby selecting events where two or more slabs of the outer counter are hit. For MT2 a higher energy deposit equivalent to 2.5 MIPs was required to select multiplicities of three or larger. These conditions enrich events that have final states with higher multiplicities and therefore higher masses.

7.5. Calorimeter Trigger

The calorimeter trigger selects high-energy photons detected by ECAL2 within 12×12 cells, whereby 8 cells surrounding the beam hole are excluded, as depicted in Fig. 57. The trigger logic is implemented in the existing ECAL2 readout module described in Section 6.3.1. At the first stage, FPGAs mounted on the MSADC cards detect a signal and extract, on a cell-by-cell basis, amplitude and time information. The time information is obtained using a digitally implemented constant fraction algorithm. In order to achieve good time resolution and clean up noise, signals below $800\,\mathrm{MeV}$ are rejected at the cost of a small uncertainty of the measurement of the total amplitude. At a later stage, time and energy calibrations are applied. The sum of the time-correlated energies in a selected region of cells is compared with a programmable threshold. The achieved precision is $\sigma = 4.97\,\mathrm{GeV}$ for a $60\,\mathrm{GeV}$ threshold, determined by fitting an error function, as shown in Fig. 58. The main contributions to this precision are the

[10] minimum ionising particle

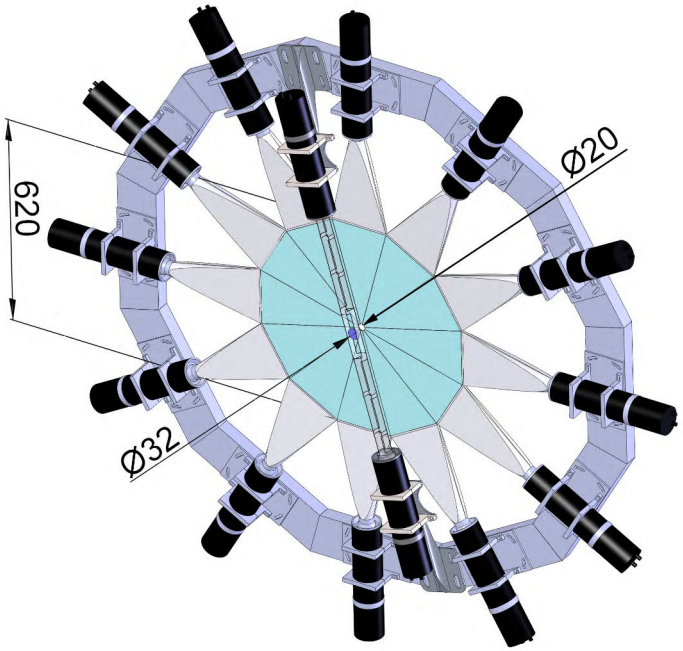

Figure 56: The multiplicity counter. All dimensions are in mm.

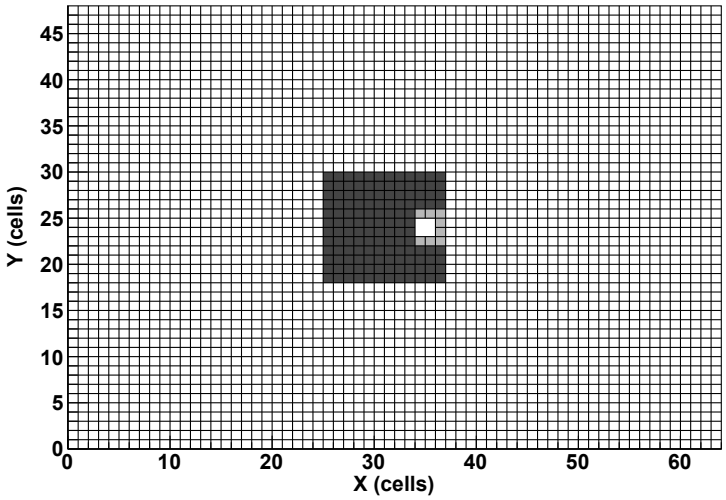

Figure 57: The active area of the ECAL2 trigger (shown in dark grey). The cells shown in light grey are rejected due to high rates.

accuracy of the per-channel thresholds and the preliminary calibration constants used in the trigger system. The overall time resolution could be reduced to about 1 ns by digital signal processing, as illustrated in Fig. 59.

7.6. Physics Triggers

The final physics triggers are summarised in Table 5 together with their typical rates. A standard physics trigger is generated by a combination of the beam trigger, the veto system, and one of the specialised triggers described above.

The diffractive trigger (DT0) is the main physics trigger for spectroscopy data taking. Based on the proton trigger, it selects events with recoiling protons from the target. Besides the low angle cut-off of the beam killers, DT0 introduces only a minimum bias on the angular acceptance of forward particles.

The "low-t" triggers, LT1 and LT2, are especially important for measurements with solid-state targets. In this case, the recoil proton has to pass dense material that can lead to large uncertainties due to multiple scattering or protons stopping in the material. This means that for heavy targets the DT0 trigger is not as efficient as for the hydrogen target. Therefore, a large part of the solid-state target data is recorded with prescaled LT1 and LT2.

The Primakoff trigger (Prim1) uses the calorimeter trigger with a $60\,\mathrm{GeV}$ threshold. A secondary Primakoff trigger (Prim2) is based on a calorimeter trigger with a threshold of $40\,\mathrm{GeV}$ and a prescaling factor of two. Its purpose is to monitor the Prim1 trigger threshold.

The kaon trigger (KT) makes use of the CEDAR detectors in the beam line, which are set to detect beam kaons (see Section 3.3). Signals from both CEDARs need to

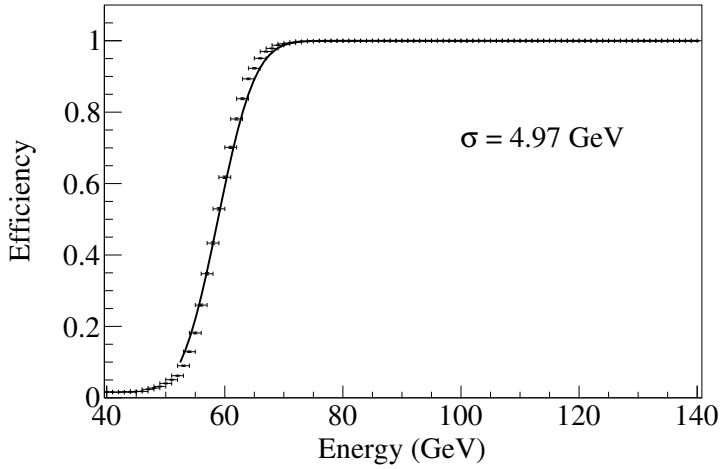

Figure 58: Efficiency of the ECAL2 trigger as a function of the energy. The solid line is a fit to the data with an error function.

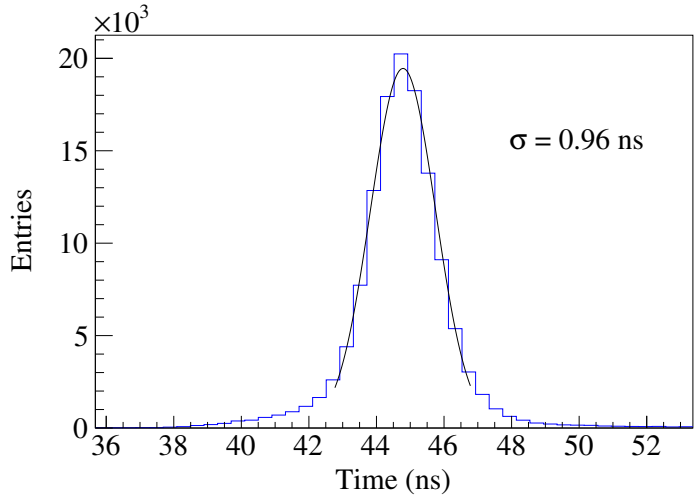

Figure 59: Time resolution of the CFD algorithm for a representative cell in the centre and signal amplitudes above 800 MeV.

Table 5: Overview of trigger subsystems, vetos and physics triggers used for data taking.

Trigger subsystem	**Logical composition**	
Beam trigger (BT)	SciFi1 $\wedge$ beam counter	
Beam killer veto	beam killer 1 $\wedge$ beam killer 2	
Veto	Sandwich $\vee$ veto hodoscopes $\vee$ beam killer	
Proton trigger	see Eq. 3	
Multiplicity trigger MT1	1 (later 2) el. of outer ring counter	
Multiplicity trigger MT2	amp. inner disk $>$ 1.6 MIPs (later 2.5 MIPs)	
Calorimeter trigger	$\sum_{12\times12}$ cell $\mathrm{amplitude} > \mathrm{threshold}$	
CEDAR trigger	CEDAR1 multiplicity $\wedge$ CEDAR2 multiplicity	
Physics trigger	**Logical composition**	**Rate / 10 s spill**
Diffractive trigger DT0	BT $\wedge$ proton trigger $\bar{\wedge}$ veto	180k
Low-t trigger LT1	BT $\wedge$ MT1 $\bar{\wedge}$ veto	370k (140k)
Low-t trigger LT2	BT $\wedge$ MT2 $\bar{\wedge}$ veto	620K (260K)
Primakoff trigger Prim1	BT $\wedge$ calorimeter trigger ($>$ 60 GeV) $\bar{\wedge}$ veto	260k
Primakoff trigger Prim2	BT $\wedge$ calorimeter trigger ($>$ 40 GeV) $\bar{\wedge}$ veto	450k
Kaon trigger KT	BT $\wedge$ CEDAR trigger$\bar{\wedge}$ veto	30k

be present for the trigger in order to maximise its purity. It is used as a kaon-enriched beam trigger for luminosity monitoring via $K \rightarrow 3\,\pi$ decays and for systematic studies.

Further auxiliary triggers are set up for monitoring purposes, systematic studies and alignment purposes (see Section 9.2). They include an additional beam trigger with a transverse acceptance of $3.9 \times 3.9\,\mathrm{cm}^2$, which is required for the alignment procedure. The Veto Inner trigger and Halo triggers make use of the hodoscope veto system to detect straight halo tracks for muon data taking, which is utilised in the alignment procedure, as well.

All inputs to the trigger system and the signals of the individual sub-triggers and triggers themselves are monitored with TDCs and scalers. In addition, the individual signals of the multiplicity counters are monitored by sampling ADCs.

8. Data Acquisition

The COMPASS data acquisition system (DAQ) has been designed to cope with high trigger rates and large data flow. For data taking with hadron beams both interaction rate and particle multiplicity per interaction are higher than for a muon beam, making these requirements even more important. The DAQ is based on a pipelined architecture, which was fully implemented for the 2008/2009 data taking. It is complemented with a Detector Control System (DCS), which permanently monitors all parameters relevant for the operation of the setup. The general structure of the COMPASS DAQ and DCS systems were described in Ref. [1]. In this section their main characteristics are shortly reviewed; only the most important improvements and modifications are discussed.

8.1. General structure of the COMPASS data acquisition system

For typical hadron beam intensities of up to $5 \cdot 10^7$ particles per spill, the various COMPASS triggers combine to a total trigger rate of more than 30 kHz. The overall number of electronic channels is larger than $\sim 250\,000$, and the generated event size has a mean value of 40 kB. Accordingly, a data rate of up to 1.2 GB/s is acquired during the 9.6 s long SPS spill. When averaged over a typical SPS accelerator 'supercycle" of 42 s (duty factor of 23%), these data generate a flow of about 270 MB/s. Note that as a

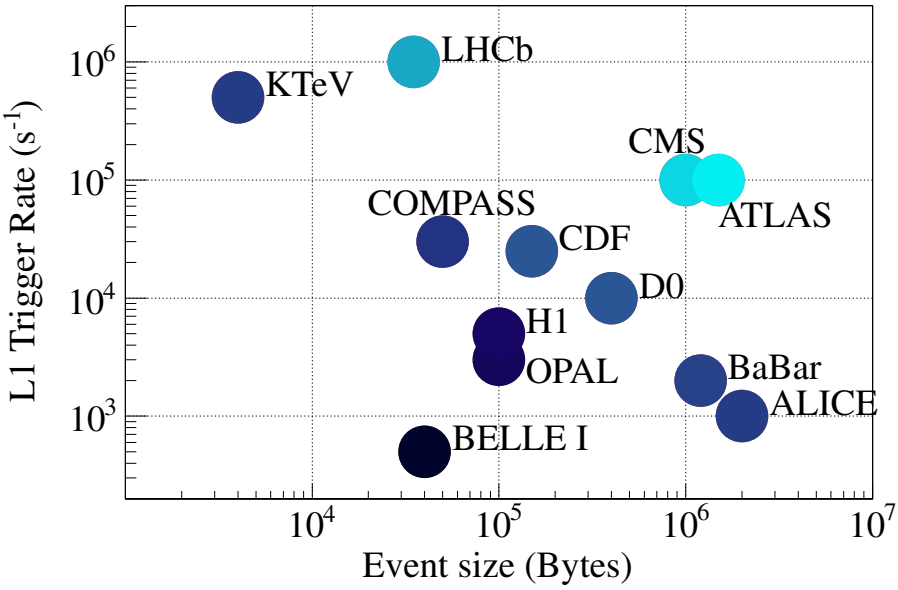

Figure 60: Trigger rate versus event size. The COMPASS DAQ system is compared to several large-scale experiments. The comparison is done for first-level (L1) triggers or their equivalent.

function of the actual SPS accelerator usage, the length of the supercycle may change by several seconds. As a consequence, the instantaneous data flow of the COMPASS readout system must be able to reach peak throughput values of up to 350 MB/s. In comparison with other large-scale experiments, the COMPASS data acquisition system operates with relatively moderate event sizes, but features high trigger rates (Fig. 60).

The DAQ system is controlled by the Trigger Control System (TCS). The TCS synchronises the elements of the front-end electronics by providing a common low-jitter system clock of 38.88 MHz, an encoded trigger signal, and event identification information. More than 150 data concentrator modules (called readout-driver modules in Ref. [1]) receive this information and distribute it further to the front-end cards. The system has a star-like network topology implemented using optical network elements and passive splitters. The system clock is used for front-end pipeline data processing and time measurements.

The overall structure of the COMPASS DAQ system is shown in Fig. 61. The detector signals collected by the front-end electronics are digitised in either TDC or Sampling ADC (SADC) cards. The data coming from the digitisation cards are then transmitted to the concentrator modules through a HOTLink interface [40]. Two types of concentrator modules were specifically developed for the COMPASS detectors: CATCH and GeSiCA, including a more recent version, called HotGeSiCA. All modules are housed in VME crates. Spill and event numbers, reference clock and synchronisation signals are provided to the concentrator modules by an optical link coming

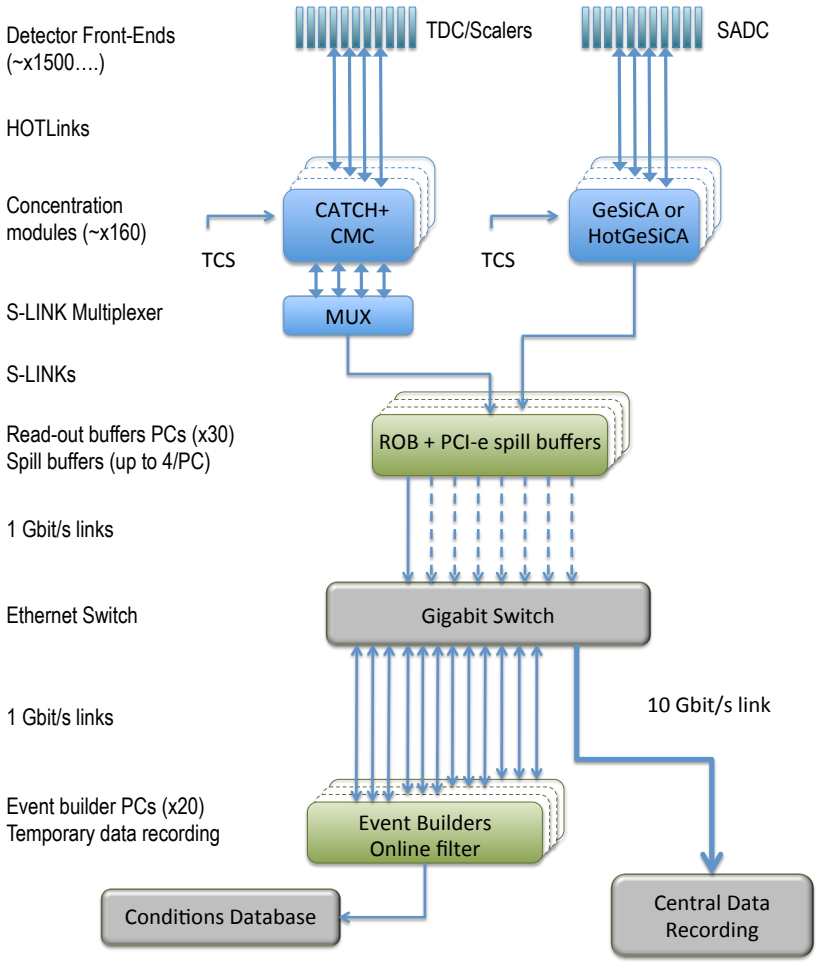

Figure 61: Overview of the COMPASS DAQ system. Data coming from the detectors are first digitised in the front-end cards and then merged in the concentrator modules, either CATCH or GeSiCA(HotGeSiCA). The data from the concentrator modules are first sent to the Readout Buffers and then transmitted to the Event Builders. The data are temporarily saved on disk, before being migrated to the Central Data Recording facility.

from the TCS. The HOTLink interface is also used to transmit this information to the front-end cards.

Each 9U CATCH module [41] houses four CATCH mezzanine cards (CMC) that receive detector signals coming from Micromegas, scintillating fibres, wire chambers, and hodoscope detectors. The CATCH firmware merges the data from the mezzanine cards and transmits them to the central readout buffer computers through a S-LINK optical link [42].

For detectors with low occupancies the data of up to 4 CATCH modules are multiplexed by an S-LINK MUX card before being transmitted to the readout computers. The S-LINK MUX card houses one S-LINK source card and is mounted on P3 connectors on the backside of a VME crate.

The 9U GeSiCA modules can read up to four 12-channel GEM or Silicon SADC cards. The more recent 6U version named HotGeSiCA is also able to read SADC, MSADC, and APV data from the RICH and PixelGEM detectors. Although smaller in size, the HotGeSiCA module has eight RJ45 or optical HOTLink ports, instead of four for GeSiCA. In addition, the HotGeSiCA module can be equipped with 500 MB of memory and a HOTLink output interface for cascading HotGeSiCA modules and concentrating the data from up to 64 front-end cards. This readout scheme is used for the Rich Wall detector (see Fig. 36). Similar to the CATCH modules, the GeSiCA and HotGeSiCA modules send data through a S-LINK interface to the readout buffers, while the information coming from the TCS receiver is transmitted to the front-end electronics through a HOTLink connection.

The DAQ system is composed of two main types of computers, called Readout Buffers (ROB) and Event Builders (EB). All computers run Linux operating system (see Table 6). Each ROB is equipped with up to four spill-buffer PCI cards. The PCI cards collect the information from the corresponding concentrator modules via S-LINK optical fibres. The data are temporarily stored in a daughter SDRAM card of 512 MB or 1 GB memory during the spill, before being fully transmitted to the computer. All ROBs are connected to all EBs through a Gigabit Ethernet interface. The role of each EB is to build a complete event using the information from all the ROBs, to split the data into files of 1 GB each (chunks), and to store these files on its internal disks. In addition, the EBs run an on-line filtering software used for both data filtering and data quality monitoring. The software used for the data acquisition is the DATE acquisition framework [43], developed for the CERN experiment ALICE.

From the EBs disks, the data files are transferred to the CERN computer centre into the CASTOR hierarchical storage system [44]. Files are copied to CASTOR disk pools by multiple TCP/IP streams through a 10 GB/s optical link and then stored to tapes. Up to 20 TB of data per day can be stored on tape when the experiment is running.

8.2. Trigger rate and dead time settings

In order to achieve high trigger rates with reasonable dead times, several improvements of the data acquisition chain were necessary. The dead time, as defined by the Trigger Control System, depends on three minimum time intervals. These are: the time interval between two consecutive triggers, the time interval for three successive triggers, and the time interval for ten successive triggers. During data taking with a muon beam these values were set to 5, 75 and 250 µs, respectively.

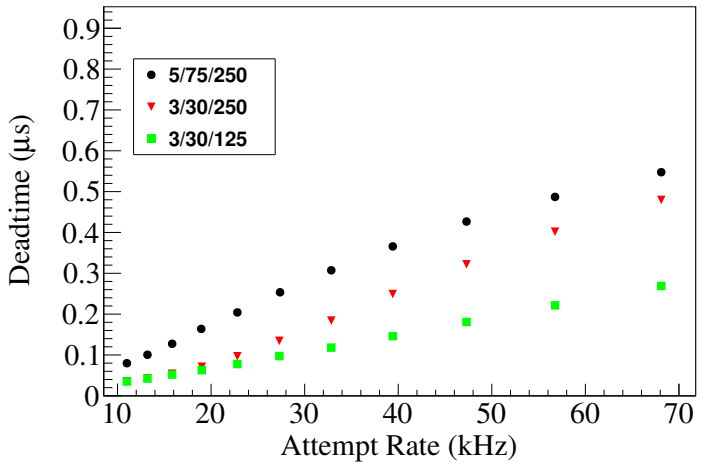

Figure 62: Data acquisition dead time for three different TCS settings, as measured as a function of the attempted trigger rate. The settings used in 2008/2009 are shown in triangles.

For data taking with hadron beams, the minimum time between two consecutive triggers was decreased to 3 μs. Smaller values were prevented due to a noise correlated with the previous trigger and appearing on the front-end cards of the MWPC detectors. The minimal time interval for no more than three triggers was set at 30 μs. Smaller values could lead to an overflow in the TDC multi-event buffer. A third minimal time interval is required by the internal buffer of the APV chip, which can store up to 10 events. This time is set according to the speed of the analogue output signal sent by the APV chip to the SADC cards. Analogue values are sent by the APV chip at a frequency of 20 MHz, corresponding to a digitisation time (including overheads) of 21 μs per event. More than 200 μs are then necessary to read ten events, justifying the 250 μs limit. Dedicated tests have shown that in the future the ten events interval can be reduced to 125 μs if the APV read-out frequency is increased to 40 MHz and the SADC card firmware is modified accordingly.

Figure 62 shows a comparison between the dead times resulting from the different trigger settings. The improvement of the time interval for three triggers results in a significant decrease of the dead time. For the nominal hadron data taking trigger rates of 30 kHz the new settings generate a dead time of 15% instead of 28%.

8.3. DAQ hardware and database architecture

The COMPASS DAQ system operates with a large number of hardware (Table 6) and software components, which are controlled through various parameters. These parameters are produced by on-line processes, operator entries, slow-control of the detectors, or result from specific run conditions. Together with other monitored quantities, such as trigger rates, run and spill information, they are stored in several MySQL [45] and Oracle [46] databases.

Table 6: Summary of the COMPASS data acquisition hardware, as used in 2009. Dual and quad-core processors are indicated in the parenthesis near the processor name. Both memory and disk sizes are given in GB.

Service	Nb	Processor	Memory size	Disk size
Event builders	12	Xeon, 3 GHz (×2)	4	1100
	8	Xeon, 2.5 GHz (×4)	4	5600
Read-out buffers	5	Xeon, 2 GHz (×4)	4	500
	8	Xeon, 3 GHz (×2)	4	250
	16	Pentium-3, 866 MHz	1	18
File servers	2	Xeon, 3 GHz (×2)	4	1100
Gateways computers	2	Pentium-4, 3 GHz (×2)	2	82
Database servers	3	Xeon, 3 GHz (×2)	4	1100
Run control	4	Pentium 4, 3 GHz (×2)	2	82
Front-end CPUs	26	Celeron, 336 MHz	0.256	

The *front-end configuration database* incorporates all information relevant to the front-end modules and processors. The *logbook database* collects a large number of experimental parameters and operator comments relevant for a specific data-taking period, usually defined as a run. Parameters that are likely to change more frequently, such as beam information, beam line settings, scalers and some monitoring values, are stored in a *spill database*. The *DATE configuration database* is used for the description of the on-line computers (ROBs, EBs, FSs,..) as well as for parameters relevant for the data acquisition. This database also includes the configuration of the on-line filter software. Another database, called *DATE message log database*, collects all process logs and messages.

The 130 GB of data from all MySQL databases are hosted on two physical servers, synchronised through a master–master replication. Clients connect to the database through a virtual address pointing to a third server. The third server runs a MySQL Proxy software [47] that monitors the communication between the client and the database. Besides the proxy, the third server also hosts a web server Apache [48] and a monitoring service (Nagios) [49]. The web service provides interfaces to run logbook, database administration programs, and diagnostic tools. Nagios monitors the availability of database servers and the state of replication.

A specific database table is used for the Detector Control System (DCS), e.g. for monitoring of ECAL1 and ECAL2 modules. On the other hand, read-out values of parameters obtained by the DCS independently are copied to a dedicated database table.

Full MySQL database backup is being executed regularly, whereby the binary log that is created during the replication is regarded as incremental backup. Furthermore, the databases are periodically replicated into the CERN computer centre.

8.4. Detector Control System

The Detector Control System (DCS) [50] collects data from the various detectors, hardware devices, and data acquisition elements with programmable reading cycles. For the COMPASS experiment the actual cycle times range between 2 seconds and 30 minutes. It provides a user-friendly interface, which is used to set remotely most

parameters relevant for operating the experimental setup. When predefined conditions are met, namely if monitored values go beyond predefined thresholds or settings, it displays on-line warnings and alerts in the user interface, sounds acoustic alarms in the control room, notifies predefined recipients by SMS and email and, when necessary, switches off sensitive detector channels. All values and alerts are stored in a centralised Oracle database with a frequency of typically few minutes per monitored parameter. Queries on the database are executed regularly for storage of data, or on demand.

The DCS architecture consists of three layers: the supervisory layer, the front-ends layer and the devices layer. The supervisory layer of the DCS is based on a commercial SCADA system (Supervisory Control and Data Acquisition), PVSS-II [51], adopted by CERN. On top of PVSS-II, a package of software tools called Joint COntrol Project (JCOP) Framework [52] is also used. Developed at CERN, this package is specific for high-energy physics applications. The front-ends layer includes the drivers necessary for the hardware devices and provides the communication protocol between the supervisory layer and the devices layer. The devices layer comprises all hardware elements and sensors.

The system is flexible enough to easily incorporate new detectors and monitored parameters. For the data taking with hadron beams in 2008/2009, a number of new detectors were included in the system: RPD, Sandwich veto, Multiplicity Counter, Beam Killers, Beam Counter, PixelGEMs, liquid hydrogen target, and the new Silicon detectors with their cryogenic devices. In addition, the monitoring of the CEDARs and the two electromagnetic calorimeters was considerably improved.

New high voltage and low voltage channels and VME crates were used and integrated in the DCS for the hadron data taking. They are monitored and controlled by OPC or DIM servers [53; 54], with which they communicate by use of the CAN[11] and CAENet field buses [55].

The monitoring of CEDAR parameters (pressures, temperatures, HVs and motors) is done via a DIP server maintained by CERN [56]. The ratio of the pressure to the temperature is calculated for every spill. If the value is found outside the appropriate range, a warning signal requesting a correction of the CEDAR gas pressure is generated.

The monitoring of the two electromagnetic calorimeters required a substantial extension in the number of monitored channels, namely 1500 for ECAL1 and 3068 for ECAL2. Between spills, the calorimeter modules of ECAL1 and ECAL2 are flashed by a laser and LED light pulses, respectively (see Section 6.2.2 and Section 6.3.2). The DAQ on-line filtering software collects the responses from all modules, calculates the average amplitudes for each spill, and stores them in the conditions database. The DCS reads them, compares them to the reference values, and defines its state of alert. The voltage and the current of the powering system of ECAL1 and ECAL2, the power supply of the LED monitoring system and the status of the laser of ECAL1 were added to the list of controlled parameters.

The monitoring of the liquid hydrogen target and of the cryogenic system of the Silicon detectors is done using a dedicated Programmable Logic Controller (PLC) and a control system. Pressures, temperatures, vacuum gauge values and liquid levels are

[11] Controller Area Network. ISO standard 11898, see e.g. www.iso.org.

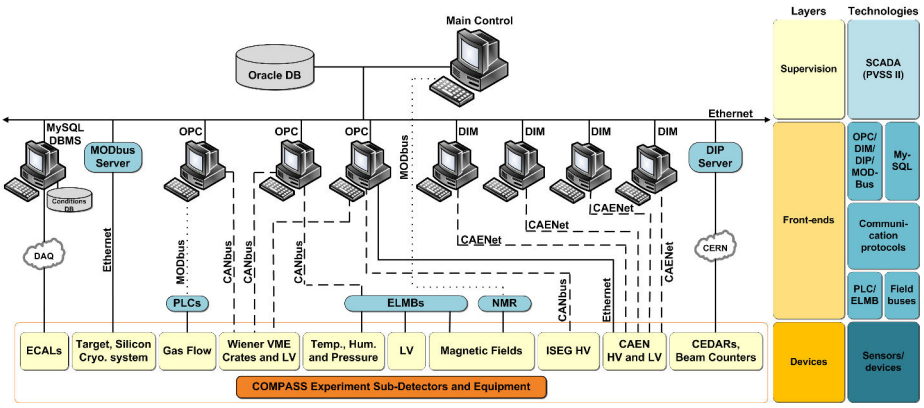

Figure 63: Implementation of supervision, front-end and device layers of the Detector Control System.

transmitted to the DCS using a MODbus [57] server.

The data generated by the DCS are temporarily saved on a local disk whose contents are transmitted to a centralised CERN Oracle database with a cycle of a few seconds. Parameters that are relevant for the physics analysis are regularly copied to a COMPASS MySQL database or are provided to users as ROOT trees or ASCII files.

9. Event Reconstruction and Detector Performance

The main reconstruction software is called CORAL (COmpass Reconstruction and AnaLysis); it is detailed in Ref. [1]. CORAL outputs mDST ("mini Data Summary Trees") files that contain reconstructed events and information related to the detectors. The mDST files are organized in tree-like structures based on the ROOT [58] package. The information stored in the mDST is analysed using a dedicated software called PHAST (PHysics Analysis Software Tool). Besides accessing the mDST data, PHAST provides an environment for physics analysis and includes tools for mDST creation, further data processing and filtering. The event reconstruction in CORAL comprises all detectors except the RPD and the CEDARs, which are included at the PHAST level, i.e. during the mDST processing stage.

This section describes the tracking method, the detector alignment procedure, and the vertex reconstruction technique used in the analysis. It gives also details on the analysis flow for detectors introduced into or upgraded for the hadron setup, namely for RPD, RICH-1, CEDARs, and ECALs.

9.1. Track Reconstruction

The track reconstruction software reconstructs trajectories of charged particles, thereby determining such properties as their momentum and total radiation length traversed. It uses the measurements from the tracking detectors and combines them with the description of the magnetic fields and material distribution in the setup. For the material distribution the ROOT geometry package [59] is used. The included detectors

are all tracking detectors, trigger hodoscopes and the beam telescope (SciFi and Silicon detectors before the target in Fig. 3). Prior to the reconstruction process, a time cut relative to the trigger time is applied to all hits.

The track finding algorithm is subdivided into two steps. First, it searches for straight track segments in the zones that are free of strong magnetic field or of large material thickness. In these zones the particle trajectories can be approximated by straight lines. In a second step, called "bridging", the straight track segments from different zones are combined over dipole magnets and hadron absorbers. In order to account for the deviation from a perfect straight line, as caused by fringe fields and multiple scattering, an iterative approach is used with progressively wider search roads. This approach is motivated by the idea of first solving the case of the straighter tracks, which have higher momenta, and turning to the more difficult case of the lower-momentum tracks only after the hits used in the first iterations have been removed from the search procedure. This scheme still yields many ghost tracks, particularly in the later iterations that have wider "roads". To filter these out, candidate tracks are checked against a lookup table of all tracks within the accessible phase space, which was produced in a dedicated MC simulation.

The track fitting procedure is based on a Kalman filter [60]. It comprises the treatment of multiple scattering, which is based on a prior estimate of the track momentum. A "forward" fit, which starts from the most upstream tracking plane, gives the best estimate of the track parameters in the plane of the detector with the last hit. A "backward" fit, which starts from the most downstream tracking plane using the same hits, gives the best estimate at the first hit. A process combining the results of the two fits, which is known in the Kalman formalism as "smoothing", is used to determine the local best estimate at any position along the track. For each of these estimates, the procedure also determines the uncertainty in terms of the covariance matrix of the parameter vector. Outlier detection and elimination as well as the resolution of left/right ambiguities in drift detectors are also done within this framework.

For the data taken with hadron beams, the sequential three-step structure of straight zone track finding, bridging and fitting was adapted to the high rate. A search for straight track projections in the vertical plane spanning several zones of the spectrometer is attempted at an early stage. A re-evaluation of the hit patterns is undertaken after bridging, once the momenta are fairly well known and the number of competing candidate tracks is reduced. These modifications improve the tracking through the drift chambers that are located in high fringe fields around the SM1 magnet and in the Silicon vertex detectors that are placed in the close vicinity of the target and are densely packed with hits.

The event reconstruction was further improved by allowing some update of the track information after vertex reconstruction (see Section 9.3). If the weighted mean time of the hits associated to the incident particle of a primary vertex deviates from the trigger time more than expected by statistical fluctuations, in the order of a few ns, the latter is re-evaluated. After correcting it and updating the hits in the drift detectors, the tracks are either refitted or the search is restarted from scratch.

For the evaluation of the performances of the tracking package, a GEANT3-based simulation of the COMPASS setup is used, as described in Section 10.1. The evaluation is based on criteria of association, reconstruction, and reconstructibility. A track is

associated to a MC particle if more than a fraction f of the hits originate from this particle. Here, pions decaying into muons are considered the same single particle. A MC particle is declared reconstructed if a track fulfilling some *ad hoc* requirements can be associated to it. Not reconstructible (or not worth to be reconstructed) are those particles that fall outside the acceptance or are not relevant for the physics process being under study. In the examples presented below, the fraction f is set at 75%, only primary particles are considered, the reconstructed tracks must be bridged over one or both magnets and must originate from the primary vertex.

Several MC samples were evaluated, corresponding to different final states of the COMPASS hadron programme. They give similar performance values. As an example, Figs. 64, 65 show the results for the case of the dissociation of $190\,\mathrm{GeV}/c$ pions on a hydrogen target into five charged pions with an invariant mass in the range $1\,\mathrm{GeV}/c^2 \leq M(5\pi) \leq 4\,\mathrm{GeV}/c^2$. This process was selected, because it has a larger angular coverage compared to other processes.

The efficiency is defined as the ratio of number of reconstructed reconstructible particles over the number of reconstructible ones. With the criteria defined above, this corresponds to the fraction of primary particles reconstructed with momentum and connected to a vertex. The efficiency represents the combined performance of all involved detectors of the reconstruction software: a particle may fail to be reconstructed because it decays, re-interacts, re-scatters, because of inefficiencies of the trackers or because of deficiencies of the algorithm. In order to isolate the contributions of the software, the efficiency that an ideally performing algorithm would reach is computed in a special mode by exceptionally making use of the Monte Carlo truth information. The usual track finding steps are bypassed and the track hit patterns are determined instead by accumulating hits along the known trajectories of the generated particles up to a point where multiple scattering or reinteractions become dominant. The overall efficiency is then factorised into this ideal efficiency characterising the setup and a software contribution. The two factors, as well as their product, are shown as a function of momentum in Fig. 64. While beyond $10\,\mathrm{GeV}/c$ the overall efficiency is nearly flat, it starts to decrease below that value. The software contribution is stable at 95% down to about $1.5\,\mathrm{GeV}/c$.

The momentum resolution is obtained from the statistical distribution of the momentum residual for the reconstructed sample. The distribution is first binned as a function of the momentum, and in each bin it is fitted with a double Gaussian and the average standard deviation is taken as the resolution. This is done for particles bridged over SM2 (and possibly also over SM1), those bridged over SM1 only, and those only tracked in the fringe field of SM1. The latter have a very poor resolution, but can nonetheless be useful to reject unwanted final states. The simultaneously obtained angular resolution is dominated by the contribution from multiple Coulomb scattering in the target material (5% X_0 in case of the liquid hydrogen target).

9.2. Alignment procedure

In order to achieve the optimal reconstruction performance, a precise knowledge of the position and orientation in space of the more than 200 tracking detector planes of the COMPASS spectrometer is mandatory. In many cases, the geometrical survey of the experimental setup does not reach a precision that is comparable to the spatial

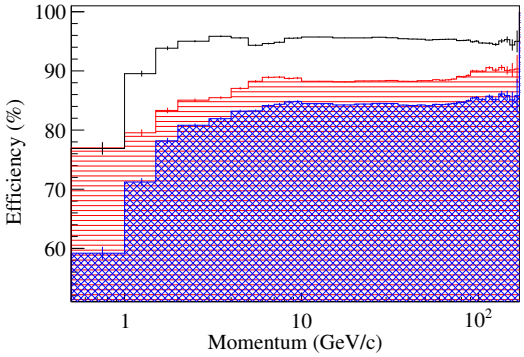

Figure 64: Efficiency of tracking and vertexing as a function of momentum with the efficiency of tracking software (solid line), setup efficiency (hatched area), and overall efficiency (crossed area).

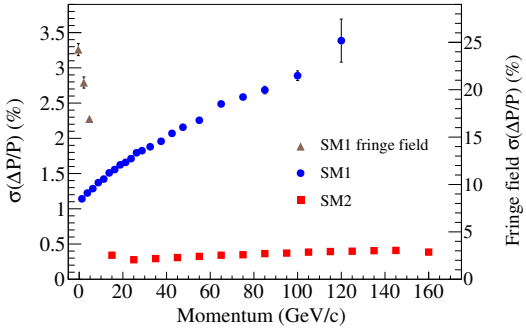

Figure 65: Relative momentum resolution as a function of track momentum. The standard deviation of the reconstruction error is shown for tracks deflected by the SM2 magnet alone or by both SM1 and SM2 (squares), by the SM1 magnet alone (circles) and for those deflected by the fringe field of SM1 only (triangles, right scale).

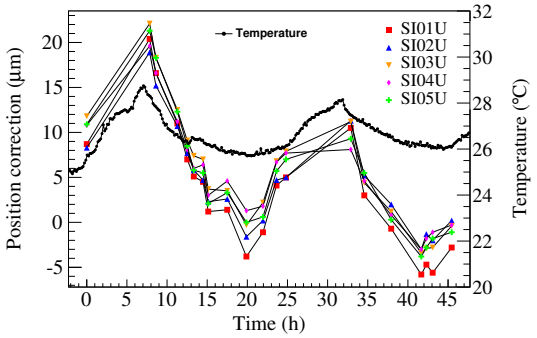

Figure 66: Run-by-run alignment correction applied to the silicon detector positions and correlation with ambient temperature.

resolution of the detectors. It is used as the starting point for an alignment procedure, which uses a sample of reconstructed tracks. The whole procedure is done in three steps with different sets of data. Each step is repeated until the corrections become negligible compared to the detector resolution.

The first step uses data recorded with a muon beam with the spectrometer magnets switched off. Therefore, straight trajectories can safely be assumed and all spectrometer arms including the beam telescope contribute to the reconstruction of a particle track. In order to reach a broad illumination of all spectrometer parts, these data are recorded with a widely defocused muon beam and by using both beam (see Section 7.1) and veto counters (see Section 7.2) as trigger. The alignment is performed by minimising the total χ^2 of all tracks in the sample, keeping four detector planes (GM04XY, GM10XY) fixed. For these pivotal points, the positions determined by an optical survey of the experimental setup has to be used in order to keep the coordinate system fixed in space. For all other planes, corrections for a translation along the measured coordinate, a rotation around the beam axis, and the effective pitch are introduced. The effective pitch takes into account a possible inclination of the detector plane with respect to the beam axis. The position along the beam axis is normally fixed to the position determined by the geometrical survey; a fit is only attempted if the residual distribution with respect to the beam axis of a given plane indicates a possible problem. The minimisation is done by the Millipede program [61], which analytically inverts a large but sparsely populated matrix.

For the second step of the procedure, the detector planes downstream of the target are aligned with the spectrometer magnets switched on. The magnetic field not only shifts the positions of the mechanical support of some detectors, but also influences the internal processes of charge propagation in gaseous detectors. The effect is strongest for some of the small-area trackers in the fringe field of SM1 (MM03 and GM01), where the Lorentz-force acting on drifting and amplified charges results in an apparent translation of the detector planes of up to $400\,\mu\mathrm{m}$. For these detectors, a correction in form of an effective shift is applied, since the distortion is uniform over the active area of the respective detector within the spatial resolution.

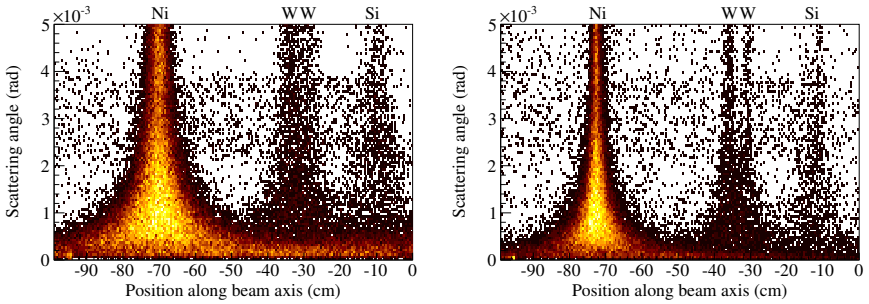

Figure 67: Distribution of scattering angle of the outgoing pion vs the position of primary vertex along the beam axis from Primakoff data, illustrating the improvement of the vertex resolution between (left) standard alignment and (right) run-by-run alignment. The structures correspond to interactions in the different targets used in the measurement (see Table 3) and in the first Silicon station downstream of the targets.

As the third step, the beam telescope upstream of the target is aligned with respect to the spectrometer that is kept fixed in space. This step is essential to optimise the reconstruction of vertices in the target. As a result, a primary vertex is reconstructed for up to 90% of the triggered events.

The alignment of the tracking stations is completed by a separate procedure for the silicon stations to fully exploit their high resolution. For these stations, displacements of up to $50\ \mu\mathrm{m}$ were observed, which are caused by variations in the temperature of the support structure. Therefore, a separate alignment for the silicon micro-strip telescope was produced for each run to account for these variations. As an example, Fig. 66 shows the corrections applied to the five silicon tracker stations in the horizontal plane as a function of time. The effect of this time-dependent alignment on the resolution is illustrated in Fig. 67 for the distribution of the scattering angle vs. the vertex position. For the events with Primakoff kinematics, in which the one outgoing track has a a very small scattering angle, the improvement is substantial. The background can therefore be reduced by a considerable fraction. As a result the distribution in Fig. 67 (right) matches the simulation, in which a perfect alignment is assumed (see Fig. 89 in Section 10.1).

The calorimeters are aligned with respect to the tracking detectors by using a separate procedure that associates charged particle tracks with signals in the calorimeters. Residuals are computed between the expected impact point of the track and the reconstructed shower position in the calorimeter. The calorimeter positions are adjusted accordingly in the plane transverse to the beam.

9.3. Vertex Reconstruction

The vertex reconstruction uses as input the charged tracks reconstructed in the spectrometer and in the beam telescope (see Section 9.1). Only two kinds of vertex topologies are considered: primary vertex and secondary vertex. The former designates the association of one beam track with any finite number of spectrometer tracks, whereas the latter corresponds to a combination between two oppositely charged tracks with a common origin.

Tracks are fed into the vertexing procedure as vectors of parameter estimates and their corresponding covariance matrices. Only tracks with momentum are accepted. Also, a cut is applied on the difference of the track times for the incoming and outgoing tracks, except for those reconstructed only in drift detectors.[12]

The contruction of a primary vertx is achieved in an iterative procedure that starts with the set of all tracks compatible with a given beam track and progressively removes outliers using an inverse Kalman filter. This procedure is prone to failing if the initial set of tracks contains a large number of fakes, because the preliminary estimate of the vertex position may then be too far from the truth. A recovery mechanism is therefore applied in order to reconnect one by one tracks that were unduly discarded. The overall procedure provides a good vertex-finding efficiency (see Fig. 64).

The vertex resolution for the hadron setup is is found to be significantly better than that of the muon setup described in [1]. The improvement is due to the reduced multiple scattering in the thinner targets employed with the hadron beam, as well as to the use of precise silicon microstrip detectors at both ends of the targets. For example, on the 5π sample already used to evaluate the tracking performances and for fully reconstructed 5π final states, the resolution along the beam axis varies from 0.75 to $4.7\,\mathrm{mm}$, depending on the 5π invariant mass, while the resolution across the beam axis lies in the 13 to 16 $\mu\mathrm{m}$ range. The vertex resolution achieved is illustrated in Fig. 67 for a single charged particle final state. Similarly, Fig. 68 shows the system of nuclear targets described in Section 4.2 as reconstructed for a three-particle final state. The sixteen lead and tungsten targets are all clearly separated. Thanks to the good resolution, the various details of the liquid hydrogen target are distinctly visible in the two-dimensional xy and xz distributions shown in Fig. 69 and Fig. 70.

Secondary vertices are reconstructed again using the Kalman filter for any pair of oppositely charged tracks that satisfy a cut on the minimum distance of approach. Any track can thus be associated with several secondary vertices and the primary vertex. Reconstructed neutral particles can then be tested against different particle hypotheses and the neutral particles can again be combined with other charged tracks to study heavier hadrons (see Section 10.1).

[12] For each reconstructed vertex, the output comprises its Cartesian coordinates and the list of its associated particles together with their reduced track parameters at the common origin, which encode only directional and momentum information.

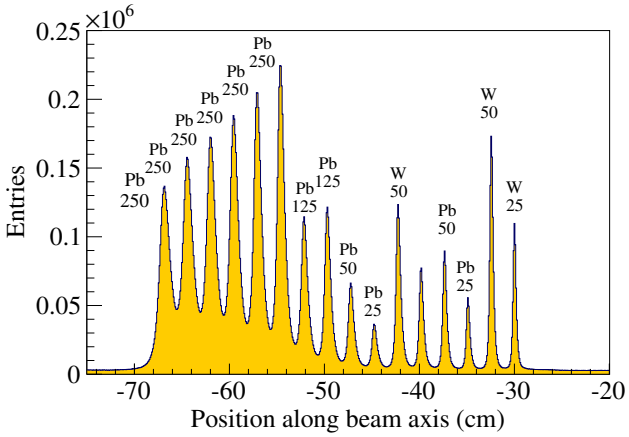

Figure 68: Distribution of reconstructed interaction vertices with three outgoing charged particles along the beam direction for exclusive events. For each solid state target the thickness is indicated (in μm).

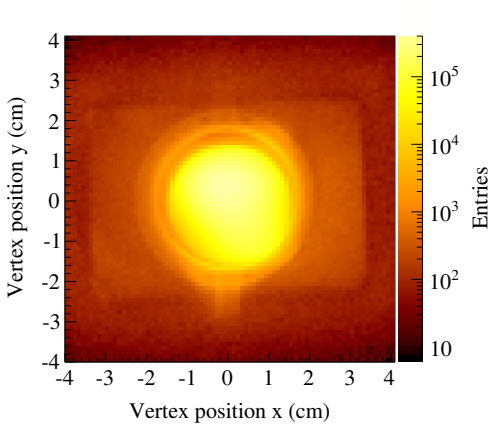

Figure 69: Vertex distributions for the liquid hydrogen target (xy projection) for events with three charged tracks.

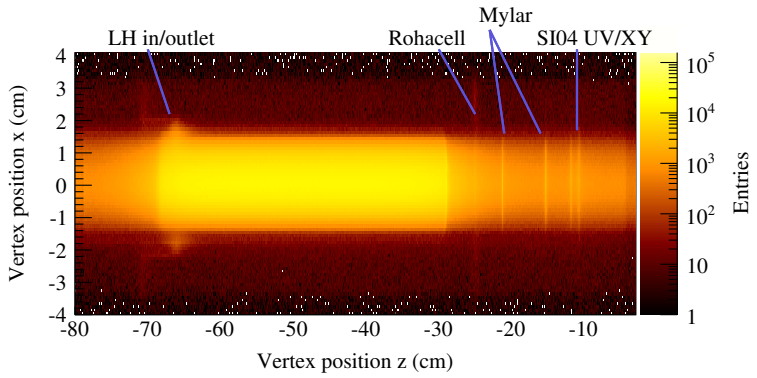

Figure 70: Vertex distributions for the liquid hydrogen target (xz projection) for events with three charged tracks. For the explanation of the structures, see also Figure 12.

9.4. Recoil Particle Detection

The 12 PMTs of the inner ring and the 24 PMTs of the outer ring of the RPD (described in Section 4.3) provide information about the integrated charge and a set of time hits. Each possible combination of upstream and downstream PMTs is used to determine a coordinate along the longitudinal direction of the scintillator and the time at which the particle crossed it. Hits are discarded if their reconstructed position is outside the fiducial dimensions of the scintillators with a safety margin of 20 cm. Reconstructed hits for the inner ring elements are associated to hits in the three corresponding outer ring elements to form tracks. For each track, the momentum is determined from the time of flight using the proton mass hypothesis and the calculated position of the hits. The track is extrapolated backwards to the vertex that is reconstructed using the beam track and the tracks of the scattered particles. A correction on the momentum is determined by accounting for the amount of the material crossed by the recoil particle. After reconstruction, a set of RPD tracks is available for event selection and physics analysis.

The calibration of the RPD is done using proton-proton elastic scattering events. The impact point of the scattered proton in the scintillator and its momentum can be predicted from the kinematics of this reaction. Matching of measurement and prediction allows for tuning the position offsets on each individual counter and the global offset of the RPD position in the COMPASS reference system. The correlation of the predicted longitudinal vertex position and the one determined using the information from the RPD is shown in Fig. 71. The momentum calibration is done by adjusting time offsets between each possible pair of scintillators in ring A and ring B. The energy loss is calibrated using the features of the energy loss distribution as a function of the velocity of the proton. The maximum in the energy loss distribution is adjusted to agree with a Monte Carlo simulation (see Fig. 15). For the inner ring, the corresponding distribution does not show the rising part seen in Fig. 15, hence the maximum energy loss ΔE is used for calibration.

For elastic pp scattering, the correlation (difference by $180°$) between the azimuthal

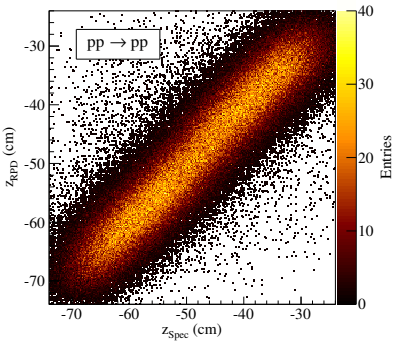

Figure 71: Correlation between the longitudinal vertex position z determined with the RPD and the one determined with the spectrometer.

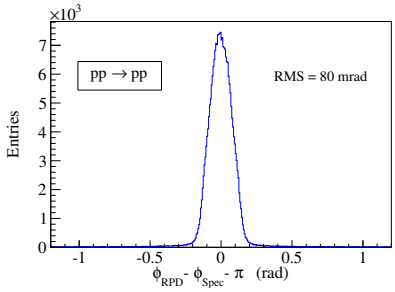

Figure 72: Correlation between the azimuthal angles of the recoil proton detected in the RPD and the scattered proton detected in the spectrometer.

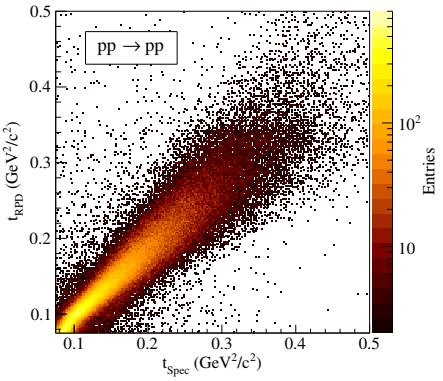

Figure 73: Momentum transfer correlation between the recoil proton detected in the RPD and the scattered proton detected in the spectrometer.

angles ϕ_{Spec} determined from tracking the scattered proton in the spectrometer and ϕ_{RPD} measured on the recoiling proton with the RPD is shown in Fig. 72. The value of the corresponding resolution, of about $80\,$mrad, is a consequence of the 24-fold segmentation of the outer ring barrel and the multiple scattering encountered by the recoiling particle in the target. The measured momentum transfer $|t|$ as determined from forward and from RPD tracks is presented in Fig. 73. A clear correlation between the two measurements over the covered range of momentum transfer is observed.

9.5. RICH-1

The separation between the different hadron types in RICH-1 is illustrated in Fig. 74, where the Cherenkov angles for reconstructed rings are shown as a function of the particle momenta. The four clearly visible bands correspond to electrons, pions, kaons and protons. For comparison, the same picture for the N_2 radiator (see Section 6.1.2)

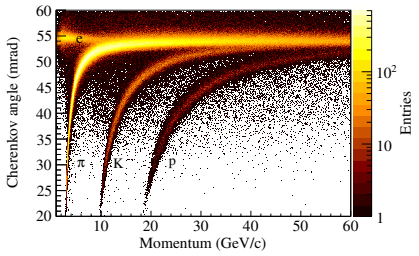

Figure 74: Cherenkov angle for reconstructed rings as a function of the particle momentum for the C_4F_{10} radiator.

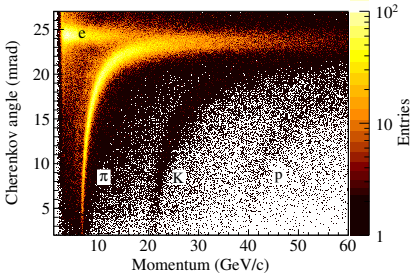

Figure 75: Cherenkov angle for reconstructed rings as a function of the particle momentum for the N_2 radiator.

is shown in Fig. 75. In this case, the Cherenkov angle at saturation reaches only $24.5\,\mathrm{mrad}$, a value that is about a factor of two smaller than the corresponding value for the C_4F_{10} radiator.

The particle identification (PID) efficiency was evaluated on samples of pions and kaons from the decay of ϕ and K^0_S mesons, respectively. The PID relies on an extended maximum-likelihood method. For each particle, different likelihood functions corresponding to the relevant mass hypotheses are computed and then compared. The likelihood function parametrises the photon distribution taking into account both the photons emitted by the considered particle (the Cherenkov signal) and the photons emitted by other particles in the event (the background). For the background parametrisation, the map of the integrated hits (see Section 6.1) in the photon detector is used. The PID probabilities (efficiency and mis-identification probabilities) are shown in Fig. 76 as a function of the particle momentum. The efficiency is larger than 90% in the region below $30\,\mathrm{GeV}/c$, where the Cherenkov angles for different mass hypotheses are well separated. Correspondingly, the mis-identification probabilities are close to zero. Above $30\,\mathrm{GeV}/c$, the Cherenkov angle starts to saturate, and as a consequence the efficiency decreases and the mis-identification probability increases. Moreover, the high momentum region corresponds to small polar angle values, and thus to a region with larger hadron multiplicity in the events.

9.6. CEDARs

As detailed in Section 3.3, two CEDARs are used to select the particle type in the hadron beam. Beam particles can be identified by requiring a minimum number of hits in the eight PMTs attached to each of the two detectors. For protons, this method achieves high efficiency and purity due to the good separation of proton and pion rings as discussed in Section 3.3. On the other hand, an online efficiency for kaon identification of only 35% is obtained using hit multiplicities, which is due to the large beam divergence and the small difference between kaon and pion ring radii. In the offline analysis this efficiency increases to 48% for physics events with a vertex in the target.

For measurements with negative hadron beams both CEDARs are set on kaon identification, requiring good kaon efficiency. In order to further improve the kaon iden-

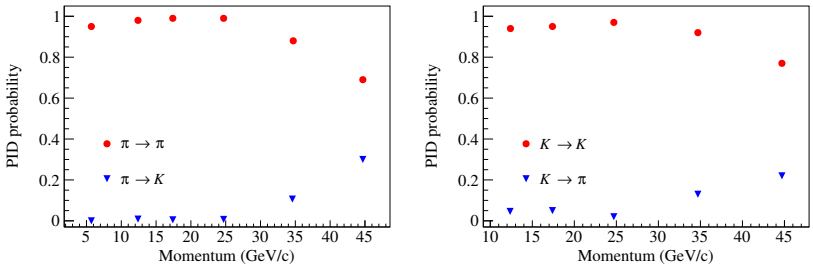

Figure 76: Identification efficiency and mis-identification probabilities as a function of the particle momentum for (left) a pion sample and (right) a kaon sample.

tification, a different method was developed for offline analysis. It is based on beam particles reconstructed in the beam telescope before the target and makes use of the response of each PMT individually to improve PID for particles that do not travel parallel to the CEDAR optical axis. In a first step, the response of the PMTs for kaons and pions is determined as a function of the horizontal and vertical angles between track and CEDAR optical axis, θ_x and θ_y. These angles are obtained from tracks measured in the beam telescope, which are traced back to the CEDAR position using the known beam optics.

A clean kaon sample is obtained from data taken with the CEDAR kaon trigger plus a beam trigger by selecting decays of beam kaon into three charged pions $K^- \to \pi^-\pi^+\pi^-$ outside the target region. The probability for a kaon to produce a signal in one of the photomultipliers is:

$$P_{(\theta_x,\theta_y)}(\text{signal}|K) = \frac{\text{Number of beam particles with signals in PMT}}{\text{Number of beam particles in kaon sample}}. \quad (4)$$

In order to identify a particle, the probability is needed that a signal is produced by a kaon. This probability can be calculated using Bayes' theorem:

$$P_{(\theta_x,\theta_y)}(K|\text{signal}) = \frac{P_{(\theta_x,\theta_y)}(\text{signal}|K) \cdot P_{(\theta_x,\theta_y)}(K)}{P_{(\theta_x,\theta_y)}(\text{signal})}. \quad (5)$$

Here, $P(K)$ and $P(\text{signal})$ are the probabilities to have a kaon with (θ_x, θ_y) in the beam and to get a signal from any beam particle with (θ_x, θ_y), respectively. Similar equations hold for a pion sample, which is obtained using diffractive production of three charged pions on liquid hydrogen, $\pi^- p \to \pi^-\pi^+\pi^- p$.

Since the beam divergences for pions and kaons are the same, the probabilities $P_{(\theta_x,\theta_y)}(\text{K})$ and $P_{(\theta_x,\theta_y)}(\pi)$ can be dropped together with the common $P_{(\theta_x,\theta_y)}(\text{signal})$. The only quantities needed are the probabilities (Eq. (4)) for kaons and pions to produce a signal in a PMT. In order to avoid regions with low statistics, a cut $(\theta_x^2 + \theta_y^2)^{1/2} < 200\,\text{mrad}$ is applied to the data before further analysis. As an example, the probability distributions $P(\text{signal}|\pi)$ for all eight PMTs of CEDAR 2 are shown in Fig. 77. The insets in the centre of the figure illustrate the position of a pion and a kaon ring relative to the PMT positions for $\theta_x = 0$ and $\theta_y = 0$ (left) and for $\theta_x > 0$ and $\theta_y = 0$

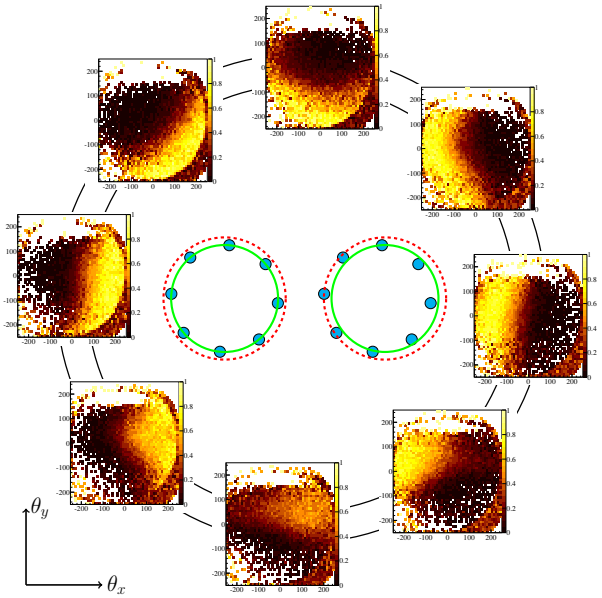

Figure 77: Dependence of $P(\text{signal}|\pi)$ on θ_x (horizontal) and θ_y (vertical) for the eight PMTs of CEDAR 2 (arranged according to the CEDAR geometry). The range for both angles is from $-250\,\mu\text{rad}$ to $250\,\mu\text{rad}$. The insets in the centre illustrate the position of a pion (dashed line) and a kaon (full line) ring relative to the PMT positions for $\theta_x = 0$ and $\theta_y = 0$ (left inset) and for $\theta_x > 0$ and $\theta_y = 0$ (right inset).

(right). No pions are expected to be detected for $\theta_x = 0$ and $\theta_y = 0$ as the detector was set on kaons for the negative beam (left inset in Fig. 77) yielding photon rings for pions larger than the diaphragm. However, PMT hits are expected when the photon ring intersects with the diaphragm due to beam divergence. As an example, pion and kaon photon rings with positive θ_x are shown in the right inset. The photon ring from the pion illuminates the PMTs on the left side, thus reducing the kaon identification efficiency.

Using the probabilities for all PMTs, the log-likelihood for a beam particle being a kaon is calculated according to:

$$\log L(K) = \sum_{\text{signal}} \log P_{(\theta_x,\theta_y)}(\text{signal}|K) + \sum_{\text{no signal}} \log\left[1 - P_{(\theta_x,\theta_y)}(\text{signal}|K)\right] \ , \quad (6)$$

where the first sum only counts photomultipliers with a signal and the second sum only those without a signal. A corresponding equation holds for the log-likelihood for a beam particle to be a pion. Figure 78 shows the distribution of $\log L(K)$ vs. $\log L(\pi)$ for (a) the kaon and (b) the pion sample, while (c) shows the results for an unbiased beam sample. The intensity in (c) reflects the beam composition, namely that the kaon component is nearly two orders of magnitude smaller than the pion component.

Kaons and pions are identified requiring a certain difference between $\log L(K)$

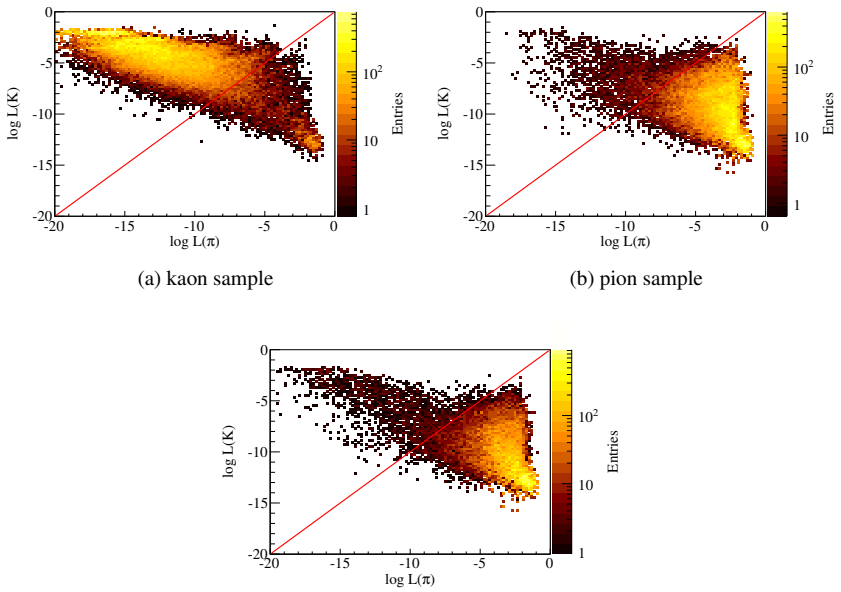

(a) kaon sample

(b) pion sample

(c) beam sample

Figure 78: Values for the log-likelihoods function for different samples obtained from CEDAR 2 calculated for (a) the kaon sample, (b) the pion sample and (c) an unbiased beam sample. The line indicates $\log L(\pi) = \log L(K)$.

and $\log L(\pi)$. The particle is identified as kaon If $\log L(K) > \log L(\pi) + A$, and as a pion if $\log L(\pi) > \log L(K) + B$. In all other cases no PID is given. The likelihood differences A and B are chosen by optimising purity and efficiency simultaneously. A good balance between high efficiency and high purity is achieved for the choice of $A = B = 1$.

In order to determine the purity of the CEDAR identification, the reactions $\pi^- p \to K^- K^0_S p$ and $K^- p \to \pi^- \bar{K}^0_S p$ are used. Due to conservation of strangeness, the incoming hadron is tagged by the outgoing hadron. The K^0_S and $\bar{K}^0_S$ are reconstructed using the two-pion invariant mass distribution. The negatively charged outgoing particle is identified using RICH-1 information. After selecting incoming kaons with the CEDAR, its purity is determined by the ratio of identified pions in RICH-1 divided by the total number of identified particles. Thus the kaon purity $p(K)$ is given by

$$p(K) = \frac{N_{\text{RICH}}(\pi)}{N_{\text{RICH}}(K) + N_{\text{RICH}}(\pi)} \,. \tag{7}$$

The purity for pions is obtained in the same way.

In order to determine the efficiency for pions and kaons, their numbers as obtained from the CEDARs are divided by the respective numbers of pions and kaons assuming the known beam decomposition (see Section 3.1). The values for kaon efficiency and purity are given in Table 7.

Table 7: Efficiencies and purities for the likelihood method ($A = B = 1$) in comparison with the multiplicity method. Only statistical errors are given.

	Kaon efficiency	Kaon purity
Multiplicity method	$(48.4 \pm 0.2)\%$	$(86.9 \pm 0.9)\%$
Likelihood method	$(80.3 \pm 0.4)\%$	$(85.4 \pm 0.9)\%$

The kaon identification efficiency is improved by almost a factor of two for the likelihood method in comparison with the multiplicity method when applied offline, while the corresponding purities are nearly identical. With the multiplicity method pion identification is not possible as the pressure was adjusted for kaon identification for the data taken with the negative hadron beam. The likelihood method allows for pion identification as well. The values obtained for pions are similar to those obtained for kaons.

In the analysis of Primakoff data, the CEDAR information is needed for an efficient kaon rejection. Using an optimisation of the likelihood method described above, pions are identified with an efficiency higher than 95%, while the kaon component is suppressed by more than a factor of 20.

9.7. Electromagnetic calorimeters

Event reconstruction in ECAL1 and ECAL2 is performed by using time and signal amplitude information as directly extracted from the SADC samples. The signal amplitude for each module is converted into energy applying conversion coefficients that were derived from the electron beam calibration. The variation of the amplitudes over the data taking period is accounted for by using the information provided by the Laser and LED monitoring systems. Details about signal extraction, electron calibration, and data monitoring are given in Section 6.2.

The energy calibration of each module is further improved by using the data derived from an analysis of the $\pi^0 \rightarrow \gamma\gamma$ decay process. The π^0 calibration is performed prior to the final data reconstruction on a fraction of the collected events. The two decay photons are singled out after having defined clusters of deposited energy and performed fits based on the definition of a shower profile. During the final data analysis, additional corrections are applied according to the specific data set, namely diffractive dissociation or Primakoff scattering.

9.7.1. Clusters and showers

For both ECALs, the event reconstruction consists of associating an energy deposit in one or several adjacent modules to a single incident particle. A set of energy deposits that is assumed to originate from a single particle is called in the following a *shower*; the full energy deposit and hit position of the particle are calculated from it. In many cases, two or more showers overlap and form a *cluster*. Thus precise knowledge of the shower profile facilitates the separation of overlapping showers. In addition, it improves spatial and energy resolutions and limits the impact of inefficient or noisy cells. Clusters of two or more particles can result from electromagnetic showers initi-

ated in the material upstream of the ECAL or from decay photons that hit the ECAL at a distance smaller than the lateral shower size.

The data analysis procedure starts by defining a cluster of neighbouring modules, in which the deposited charges are larger than a pre-defined threshold (see Section 9.7.3). The cluster is then split into showers employing a parametrisation for the lateral spread of the shower profile [62]. The shower parameters for the lead glass and Shashlik modules are determined using electrons from a dedicated calibration beam (see Section 3.2). For Primakoff data taking in which mainly high-energy photons are detected, no electron beam with the corresponding energy is available. The shower parameters are therefore derived using single photons from real data events.

9.7.2. Shower profile

The shower profiles used in the reconstruction are based on an empirical cumulative function, as defined in [62]. If the energy deposited by a shower is projected onto a transverse axis with the shower center at 0, the fraction of the total shower energy accumulated between $-\infty$ and a position x on this axis can be described by:

$$F(x) = \frac{1}{2} + \frac{1}{\pi} \sum_i a_i \cdot \arctan \frac{x}{b_i} \,. \tag{8}$$

In addition to providing a good description of this ratio, Eq. 8 is conveniently related to the energy deposited in each module [62]. Up to three contributing shower components (denoted by the index i) are summed up, with parameters a_i and b_i describing the relative weight and width of each component, respectively.
In order to obtain the shower profile parameters, the following procedure is applied. A column-wise calculation of the ratio of the energy accumulated so far over the total energy of clusters, taking the simple centre-of-gravity as the central position, yields a distribution that is fitted with the cumulative function Eq. 8 describing the shower. This is illustrated in Fig. 79 (left), which represents the fraction of the total energy deposited up to a particular column at a given distance from the shower center. The fraction of the total energy deposited in a column as a function of its distance from the shower center is shown in Fig. 79 (right).

This concept can be extended to two dimensions. In this case, the ratio between the accumulated energy up to a point (x,y) and the total energy of the shower is given by:

$$F(x,y) = \frac{1}{4} + \frac{1}{2\pi} \sum_i a_i \cdot \left(\arctan \frac{x}{b_i} + \arctan \frac{y}{b_i} + \arctan \frac{x \cdot y}{b_i \sqrt{b_i^2 + x^2 + y^2}} \right) . \tag{9}$$

The first two terms account for the ratio along x and y projections, while the third term adds an asymmetry along the diagonal.

Different sets of parameters are used for each module type. In ECAL1 the same profile with three contributions is used for all modules. The parameters were obtained for the GAMS-2000 spectrometer [62]. Since COMPASS makes use of the same lead glass modules, the parameters are unchanged.

In ECAL2, the profiles of both lead glass and radiation-hardened lead glass modules are described by two contributions, with parameters derived from the electron

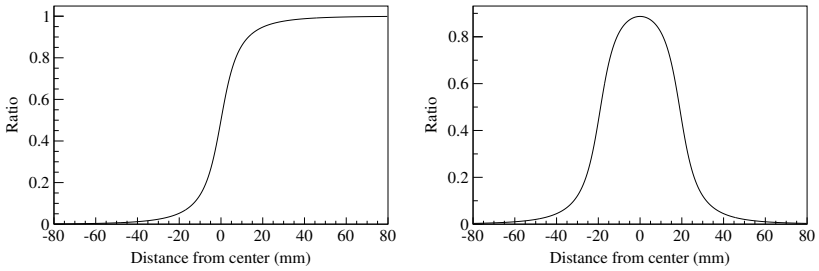

Figure 79: Shower reconstruction: (left) fraction of total shower energy collected from $-\infty$ up to a particular distance from the shower center (Eq. 8); (right) fraction of the total energy deposited in a column as a function of its distance from the shower center.

beam calibration. For the Shashlik modules, the profile consists of three contributions. The corresponding parameters are obtained from Primakoff data events that contain a single high-energy cluster. In both cases it has to be assumed that a cluster contains only one shower.

The two-dimensional ratio defined in Eq. 9 is used to calculate the relative energy deposited by a shower at the position (u_j, v_j) in each module:

$$\begin{aligned} G_j\,(x,y) &= F\,(u_j+\Delta, v_j+\Delta) - F\,(u_j+\Delta, v_j-\Delta) \\ &- F\,(u_j-\Delta, v_j+\Delta) + F\,(u_j-\Delta, v_j-\Delta)\ . \end{aligned} \tag{10}$$

Here $u_j = X_j - x$ and $v_j = Y_j - y$ are local coordinates relative to the centre (X_j,Y_j) of each module, j denotes an index over all modules and Δ is half the transverse size of a module.

9.7.3. Clustering and shower reconstruction

In a first step, signals from adjacent modules are combined to form a cluster. Starting from the first module not yet used in the cluster, each of the (vertical, horizontal, and diagonal) neighbours is checked for a measured energy above a threshold of $100\,\mathrm{MeV}$ for ECAL1, and of $200\,\mathrm{MeV}$ for ECAL2. For each new module added to the cluster, its neighbours are treated the same way.

In a second step, a fit of the shower profiles to the cluster data is performed. The fit improves the spatial resolution of the calorimeter and separates overlapping showers. The fit is first done with a single shower. Further showers are added one by one with a new fit being performed after each added shower. The parameters of the first shower are initialised to those of the module with the highest energy in the cluster and its neighbours. The energy is set to the sum of the energies of those modules, the position and time are set to the mean of the respective information weighted with the energy of each of those modules. When adding more showers, the module searched is the one with the largest relative discrepancy between its measured energy and the energy predicted to be deposited by all showers fitted to the data so far. The centre of the new shower

candidate must be located at a distance larger than $\sqrt{2}/2$ times the module width from the centre of the nearest shower. A difference in energies is also required: the central module of the new shower must contain at least 20% of the energy deposited by all other showers in this module. If such a module is found, the information it provides together with the information from the neighbouring modules is used to initialise the parameters of a new shower.

According to Eq. 10, the energy deposited by a shower of energy e_i at impact point (x_i,y_i) in a module at position (X_j,Y_j) can be calculated as:

$$E_{j,i}^{\text{pred}} = e_i \cdot G_j\left(x_i, y_i\right) \ . \tag{11}$$

As several showers might be fitted into the same cluster, the total energy of all showers in the module is given by:

$$E_j^{\text{pred}} = \sum_i E_{j,i}^{\text{pred}} = \sum_i e_i \cdot G_j\left(x_i, y_i\right) \ . \tag{12}$$

In addition to the energy, the time information is also used. The time t_i of a shower is defined as the mean value of the times of all modules contributing to the shower, weighted with the energy deposited in each module. Similarly to the predicted energy deposit in a block, the predicted time is calculated as:

$$T_j^{\text{pred}} = \sum_i e_i \cdot G_j\left(x_i, y_i\right) \frac{\sum_i e_i \cdot G_j\left(x_i, y_i\right) \cdot t_i}{\sum_i e_i \cdot G_j\left(x_i, y_i\right)} \ . \tag{13}$$

The predicted energy and time are compared to the measured energy E_j^{meas} and time T_j^{meas} in each module. The Minuit fitter from the ROOT package [58] is used to optimise the shower parameters to maximise the likelihood:

$$-\log L = \frac{1}{2} \sum_j \left(\frac{\left(E_j^{\text{meas}} - E_j^{\text{pred}}\right)^2}{\sigma_{j,E}^2} + \frac{\left(T_j^{\text{meas}} - T_j^{\text{pred}}\right)^2}{\sigma_{j,T}^2} \right) \ . \tag{14}$$

The errors on the measured energies $\sigma_{j,E}^2$ and times $\sigma_{j,T}^2$ (Fig. 49) are calculated from an energy dependent parametrisation that has been determined from data beforehand. With this procedure the fit distinguishes between in-time showers and pile-up events.

The procedure of trying to add a new shower is stopped if the fit describes the data well or if the maximum number of showers in a cluster has been reached. The decision, whether the last shower added improves the fit, is based on a comparison of the log-likelihood normalised to the number of degrees of freedom. It is also checked that all showers have energies above the energy threshold and that they fulfill the requirements on the distance between two showers described above.

This fitting procedure returns the energy e_i, the position (x_i, y_i) and the time t_i of each shower fitted into a cluster.

The number of modules contributing to the total shower energy reaches 5×5 for the highest energy photons. A cluster may contain from one to six showers, the distribution varying as a function of the beam intensity and the trigger conditions. Figure 80 (left)

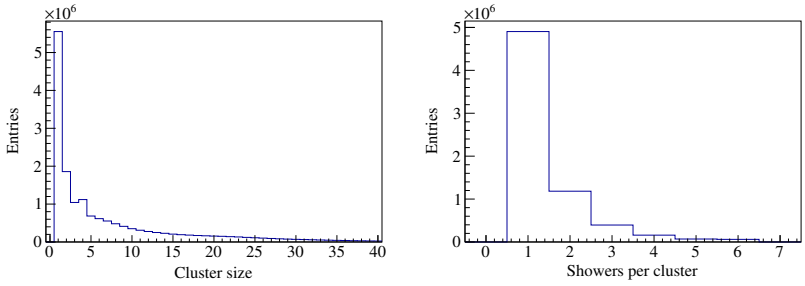

Figure 80: ECAL2 fit results for (left) number of modules per cluster and (right) number of fitted showers per cluster.

shows the distribution of the number of modules in one cluster (cluster size) in ECAL2 for the diffractive dissociation data. The number of reconstructed showers per cluster is shown in Fig. 80 (right).

For ECAL1 a simplified version of the procedure described above is employed. For the larger MAINZ and OLGA modules, an improvement of the performance by using shower profiles was not found. Each module with a deposit larger than that of any of its neighbours is used as a starting point for a new shower. Energy and position of this module are used to initialise the parameters of the shower. If larger than the energy threshold, the information contained in the neighbouring modules is then used to improve the position of the shower by calculating its centre of gravity.

9.7.4. Calibration with $\pi^0 \to \gamma\gamma$ decays

The π^0 calibration procedure is performed, prior to the final analysis, using a fraction (equivalent to 1 to 2 days of data taking) of the physics events. The reconstruction of the incident and outgoing particle tracks is required, with a definition of a primary interaction vertex. Only showers with energies E_γ larger than 1 GeV for ECAL1 and 3 GeV for ECAL2 are taken into account. Showers associated with charged tracks are discarded. In order to minimise combinatorial background, only events with less than 5 showers are used.

The two-photon invariant mass $M_{\gamma\gamma}$ is calculated for every pair of showers, assuming that both photons originate from the interaction vertex. Only pairs with invariant masses within $\pm 50\,\mathrm{MeV}/c^2$ around the nominal π^0 mass, M_{π^0}, are considered as valid π^0 candidates. For each of two showers, a two-dimensional histogram E_γ vs $(M_{\gamma\gamma} - M_{\pi^0})$ is filled, which is associated with the shower's central module. The central module is defined as the module which contains the highest fraction of the deposited energy. The values stored in the two-dimensional histograms are used as a starting point for the calibration procedure.

For most ECAL modules a slight energy dependence is observed, as illustrated in Fig. 81 (left). However, various types of unusual behaviours may also be present, e.g. as the one shown in Fig. 81 (right), which resuls from a saturated photomultiplier tube. The variations are accounted for by introducing correction factors that depend on the photon energy. The correction factors are calculated in energy slices of 2 GeV. In

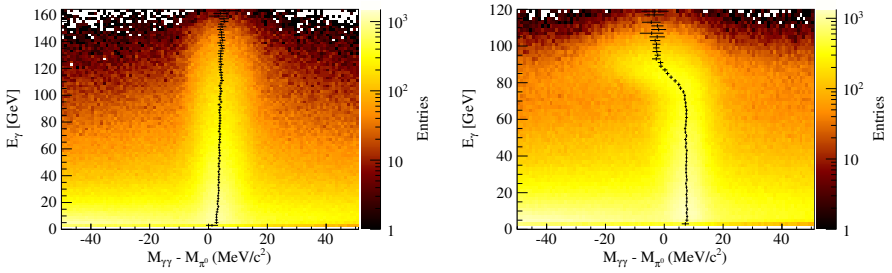

Figure 81: Energy deposition in two ECAL2 modules as a function of the difference between reconstructed and nominal π^0 mass for (left) a module with typical behaviour and (right) a module with an unusual behaviour.

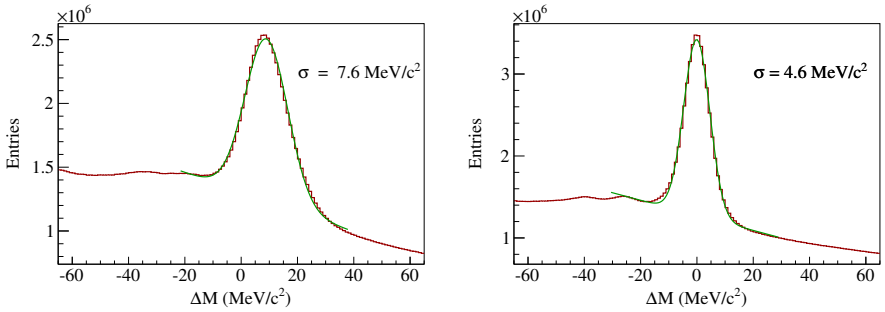

Figure 82: Difference ΔM between reconstructed and nominal π^0 masses in ECAL2 for (left) before calibration and (right) after calibration.

each slice the spectrum is fitted with a Gaussian for the π^0 peak and with a first order polynomial for the background, in an interval of $\pm 20\,\mathrm{MeV}/c^2$ around the π^0 peak. The results of the fits are displayed in Fig. 81 as black crosses; its horizontal and vertical tick marks represent the 3σ fit error and the bin size, respectively. The fitted mass differences are then used to calculate the correction factor α_i for each energy slice i,

$$\alpha_i = \frac{1}{(1 + \frac{\Delta M_i}{M_{\pi^0}})^2}, \tag{15}$$

where ΔM_i is the fitted mass offset. The correction factor for each module is calculated assuming that the energy of the second decay photon is measured precisely. Since this is not the case, the π^0 calibration is done iteratively, each iteration adding corrections to the result from the previous iteration. Typically, after 8 to 10 iterations the procedure converges. The result is a significant improvement of the π^0 mass resolution and of the π^0 mass offset, as shown in Fig. 82. After calibration, the mean value of the peak position shifts from $9.0\,\mathrm{MeV}/c^2$ to $0.0\,\mathrm{MeV}/c^2$. The mass resolution improves from $7.6\,\mathrm{MeV}/c^2$ to $4.6\,\mathrm{MeV}/c^2$.

The calibration significantly improves the response of the individual ECAL2 mod-

ules, as illustrated in Fig. 83. A similar improvement is observed for ECAL1. For most modules, the reconstructed pion mass after calibration agrees within less than $1\,\mathrm{MeV}/c^2$ with the nominal π^0 mass for π^0 energies up to $160\,\mathrm{GeV}$.

The resulting calibration is used to correct the individual module responses during the event reconstruction procedure. The precise value of the correction factor α, which corresponds to the actual energy deposited in each module, is determined by interpolation.

9.7.5. Additional corrections

Additional corrections, which are evaluated independently for the different data sets, are applied on top of the shower fit result. For the diffractive dissociation data, the reconstructed energy E as measured in a Shashlik module for an electron is compared with the corresponding charged track momentum p. A position dependence of the ratio p/E is then observed, as indicated in Fig. 84. This dependence reflects slight inefficiencies in the vicinity of the four central rods. It is accounted for by using the hit position as determined by the shower fit.

The photons detected in the calorimeters cover an energy domain that extends from less than 1 GeV for ECAL1 to more than 120 GeV for ECAL2. The measured cluster times for both ECAL1 and ECAL2 show a slight energy dependence, mainly for low photon energies. This dependence, which is always smaller than 1 ns, is fitted to the data and accounted for.

9.7.6. High-energy photons

For photon energies above 80 GeV, the kinematics of the Primakoff-Compton reaction, $\pi^- + (A, Z) \to \pi^- + \gamma + (A, Z)$, constrain the detected photons to the central 4×4 ECAL2 modules. The energy deposited in these modules must be accurately determined, even for values as large as 95 % of the beam energy. With the π^0 calibration alone this cannot be achieved. For higher energies a different method is applied. During the Primakoff data-taking period, muon beam data for systematic studies are periodically collected. These data also contain Primakoff-Compton events with photon energies nearly as high as the beam energy. Moreover, since the Beam Momentum Station (BMS) is present in the beam line, the muon incident momentum is known. Since the scattered muon momentum is also measured, the energy conservation (exclusivity) in the process provides an independent prediction of the energy of the emitted photon. The comparison with the actual ECAL2 measurement based on the π^0 mass calibration exhibits a slightly falling slope as a function of the photon energy, as shown in Fig. 85.

This trend does not only depend on the photon energy but also on the actual hit position within the Shashlik modules. The observed dependence is fitted with a three-dimensional function that includes both intra-cell coordinates and the shower energy. The correction reaches values of up to $+7\,\mathrm{GeV}$ and $-12\,\mathrm{GeV}$, as shown in Fig. 86. The major part of this correction is due to the steel rods that tie the Shashlik stack together, as previously explained in Section 9.7.5. During data taking with a pion beam, the BMS is removed and no measurement of the incident pion momentum can be performed. It is assumed that the corrections to the ECAL2 calibration for muon and pion beams are identical. This assumption is supported by the data itself; after applying the above intra-cell corrections, both the position and the standard deviation of the exclusivity

peak with a pion beam improve, similarly to the improvement achieved with a muon beam. Fig. 87 illustrates the effect of these corrections on the central modules of ECAL2.

9.7.7. Efficiency of photon detection

The efficiency for the reconstruction of single photons is defined as the fraction of photons that originate from the target reconstructed in one of the calorimeters. It thus includes effects of geometric acceptance for photons like dead material, and the intrinsic performance of the calorimeters related to thresholds, etc. The reconstruction efficiency is evaluated by a Monte-Carlo procedure using diffractive events for the $\pi^-\pi^0\pi^0$ channel (see Section 10.1) with $0.1 < t' < 1.0\,\mathrm{GeV}^2/c^2$. The thresholds applied correspond to those in the analysis of physics data ($0.6\,\mathrm{GeV}$ for ECAL1, $1.2\,\mathrm{GeV}$ for ECAL2).

Figure 88 shows the single-photon reconstruction efficiency as a function of photon energy, and as a function of the photon direction in the laboratory system. The single-photon reconstruction efficiency is rather uniform at a level of 60% for photon energies above approximately $5\,\mathrm{GeV}$. However, the acceptance strongly depends on the direction of the photon. In the centre a drop due to the beam hole in ECAL2 can be seen at $\Delta y/\Delta z = 0$ and $\Delta x/\Delta z = 0.005$. The circular shape overlapping with the hole is attributed to photons lost in the beam pipe of RICH-1. Further outside, at $\Delta y/\Delta z \approx \pm 0.02$, the shadow of HCAL1 and SM2 on ECAL2 is visible as a horizontal line, while the vertical lines at $\Delta x/\Delta z \approx \pm 0.04$ stem from a non-perfect overlap of ECAL1 and ECAL2. A general trend of lower acceptance towards outer regions is also visible, which is caused by the loss of photons with an energy below the ECAL1 threshold.

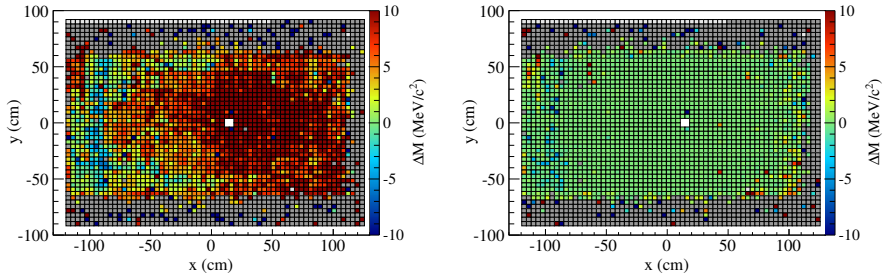

Figure 83: Difference between reconstructed and nominal π^0 masses as a function of the impact position for the ECAL2 modules for (left) before π^0 calibration and (right) after π^0 calibration. The difference is calculated using the mean value of the fitted (with a Gaussian) X-projection of E_γ vs $(M_{\gamma\gamma} - M_{\pi^0})$ histograms. The grey rows at the top and bottom ends and on the right side of ECAL2 are located beyond the angular acceptance for photons coming from the target (see Section 6.3.)

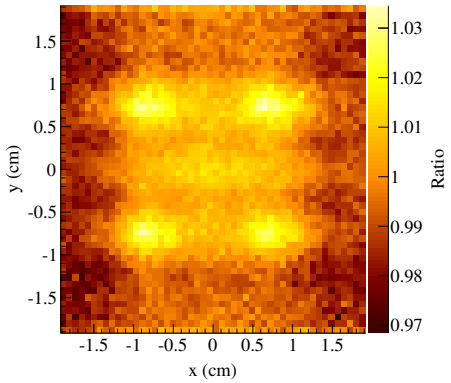

Figure 84: Ratio of track momentum over calorimeter energy as a function of the impact position in a Shashlik module relative to its centre. The four central spots with a ratio larger than one correspond to the four module rods.

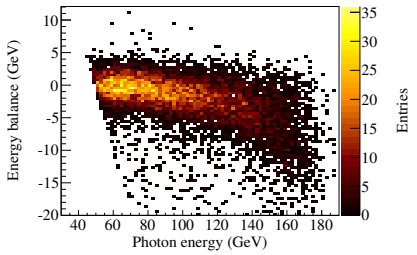

Figure 85: Difference between the beam energy and the total measured energy as a function of the photon energy.

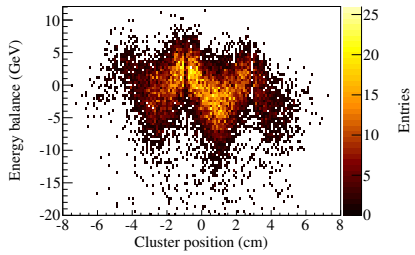

Figure 86: Intra-cell energy variation as a function of the distance to the cell centre.

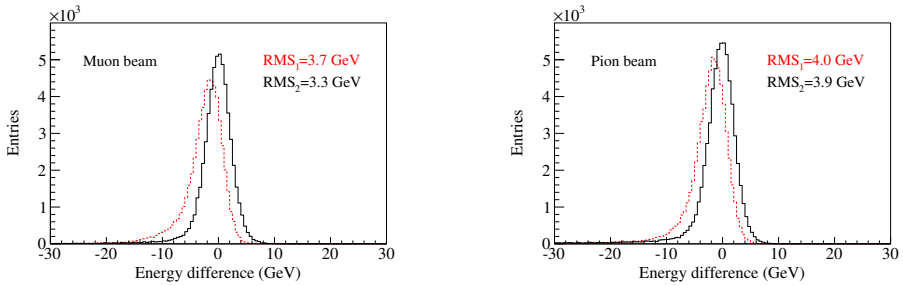

Figure 87: Difference between beam and measured energies (energy balance) for Primakoff-Compton scattering (left) with a muon beam and (right) with a pion beam. The distributions are displayed with the standard π^0 calibration only (dashed curve) and with linearity and intra-cell position corrections (solid curve); the corresponding RMS_1 and RMS_2 values are indicated.

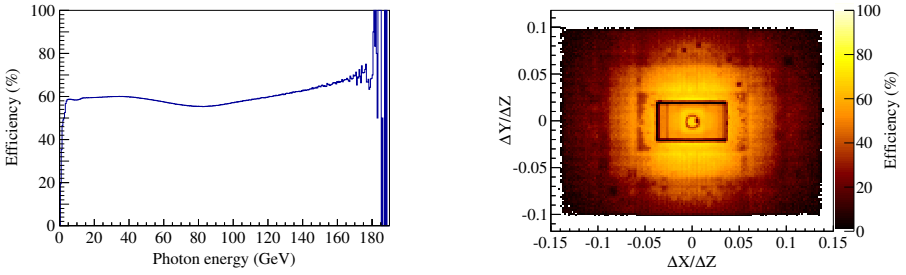

Figure 88: Simulated photon efficiency (left) as a function of the photon energy and (right) as a function of the photon direction in the laboratory system.

10. Monte Carlo simulation and performance of the setup

The interpretation of physics processes that involve hadron beams and several particles in the final-state particles requires a thorough understanding of the experimental setup. This requirement can only be achieved through a realistic simulation of the apparatus and a detailed knowledge of its acceptance as function of any of the kinematic variables that are relevant in a particular physics process. The Monte-Carlo code used to describe the setup and to determine its acceptance is described below. It is followed by a selection of characteristic experimental results, for each of the two beam polarities and for various particles in the final state. All results were obtained with the nominal hadron beam momentum of $190\,\mathrm{GeV}/c$.

10.1. Monte Carlo simulation and acceptance

The simulation of the COMPASS setup is performed using a dedicated Monte-Carlo (MC) code called COMGEANT. The code can be linked to external event generators specific to the reaction mechanism that is dominant in a given channel. Final-state particles are then propagated through the setup. The digitisation of the MC data and the subsequent reconstruction are carried out with the same software that is used for reconstructing the measured events.

Three different event generators are used to simulate diffractive reactions, central production, and Primakoff reactions. The partial-wave analysis method employed for diffractively and centrally produced n-body final states takes into account the acceptance of the apparatus using Monte-Carlo pseudo data, where the final-state hadrons are distributed isotropically in the n-body phase space. In addition to the decay phase space, the generators also simulate the production kinematics. Diffractive events are generated with a t' distribution that is tuned to the data. The central-production generator [63] simulates exponential t' distributions for both beam and target vertices. For Primakoff-Compton scattering, the generator calculates differential cross sections with contributions due to polarisability, first-order Compton vertex corrections, and soft photon emission [64].

For all generators, the beam phase space spanned by the positions and angles of the incoming particles is generated using parametrizations extracted from real data. Since the incident energy is not measured, it is reconstructed from the kinematics of fully exclusive events. Interactions in the target volume are distributed in the target material according to the target positions. Primary interactions of the beam particles in materials and detectors surrounding the target are not generated.

Scattered and secondary particles are propagated through the spectrometer by the simulation code COMGEANT, based on GEANT 3.21 [65]. Multiple scattering, energy loss, shower development, and secondary interactions are taken into account. This includes interactions of electrons and photons with detector material and creation of electromagnetic showers by these particles. Additional physics processes like hadron interactions and in-flight decays are also taken into account. Furthermore, pile-up events due to two or more particles occurring in the same time window can be generated.

The digitisation of the simulated events is performed in CORAL (see Section 9.1). Dead and active materials along the tracks are accounted for with the ROOT geome-

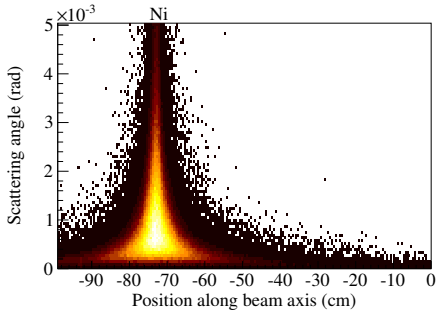

Figure 89: Monte Carlo simulation of the Primakoff-Compton reaction, showing the reconstructed position of the primary vertex along the beam direction as a function of the scattering angle of the outgoing pion. Note that interactions outside the target material are not simulated.

try package [59]. Charged-particle tracks are reconstructed from the simulated hits in the tracking detectors using the same procedure as for the real data (see Section 9.1). Detector properties such as efficiencies and resolutions are implemented in the reconstruction software using information from the experimental data. For RICH-1, the purity and efficiency of the detector are determined from the measured events and separately unfolded from the simulated data. For the electromagnetic calorimeters, shower profiles are extracted from the ECAL MC data, and a π^0 calibration is performed as for real data (see Section 9.7). The RPD information is passed directly to the PHAST physics analysis software.

An example of the good MC description achieved for the Primakoff-Compton reaction is shown in Fig. 89 for the reconstructed primary vertex as a function of the pion scattering angle. A qualitative comparison with Fig. 67 (see Section 9.3) shows that the agreement between MC and data is good. Background effects, e.g. from interactions with the detectors downstream of the target, are minimized by applying selection cuts identical to those used for the specific physics process.

Other observables relevant for the Primakoff-Compton reaction are discussed in Section 10.2. The momentum distributions of the electromagnetic component for pion and muon interactions with a solid target are well reproduced by the MC simulations (see Fig. 97). The $\pi^-\pi^+\pi^-$ decay of the K^- mesons in the beam, a process used for flux normalisation, is accurately simulated as illustrated by the momentum transfer distributions in Fig. 96.

The MC simulation of the photon reconstruction efficiency for channels with final-state photons is validated by comparing the acceptance-corrected particle decay yields for different decay channels. For example, the resulting branching ratios of $\omega \rightarrow \pi^-\pi^+\pi^0$ and $\omega \rightarrow \pi^0\gamma$ agree within 5% with the PDG values.

The acceptance of the apparatus is determined by comparing the reconstructed and generated MC events. In the Partial Wave Analysis (PWA) formalism employed for diffractive scattering, the full multidimensional acceptance for a given final state is used. For example, in three-body analyses (like $\pi^-\pi^+\pi^-$) for fixed four-momentum transfer and three-body mass the acceptance depends on five kinematic variables. The

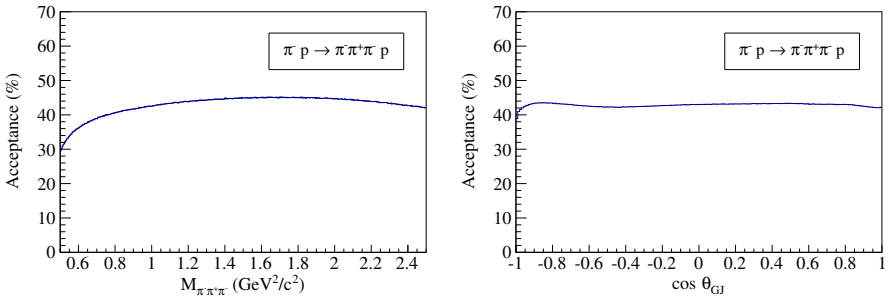

Figure 90: Acceptance for the diffractively produced $\pi^-\pi^+\pi^-$ final state (left) as a function of the 3π invariant mass and (right) as a function of the polar angle of the $\pi^+\pi^-$ isobar in the Gottfried-Jackson frame.

acceptance determined by the simulated phase-space events is then used as an input to the fits performed in the PWA formalism.

For the purpose of illustration, the acceptance for a particular variable can be determined by projecting the multi-dimensional acceptance onto this variable. In Fig. 90, the acceptance for the $\pi^-\pi^+\pi^-$ final state of diffractive dissociation is evaluated in the t' range between 0.1 and $1\,\mathrm{GeV}^2/c^2$. It is a fairly flat function of the invariant three-pion mass from near threshold up to $2.5\,\mathrm{GeV}/c^2$ and of the polar angle of the $\pi^+\pi^-$ isobar in the Gottfried-Jackson frame (see definition in Section 1).

More pronounced modulations of the acceptance are observed for channels where one or several final-state particles are identified by the RICH-1 detector. The impact of the particle identification on the acceptance in the $K^-\pi^+\pi^-$ channel is depicted in Fig. 91 for both the $K\pi\pi$ invariant mass distribution and the Gottfried-Jackson angle of the π^+K^- isobar. The reduction of the acceptance is mainly due to the limited momentum range available for kaon identification (see Section 9.5).

Figure 92 shows the corresponding acceptance plots for the $\pi^-\pi^0\pi^0$ final state.

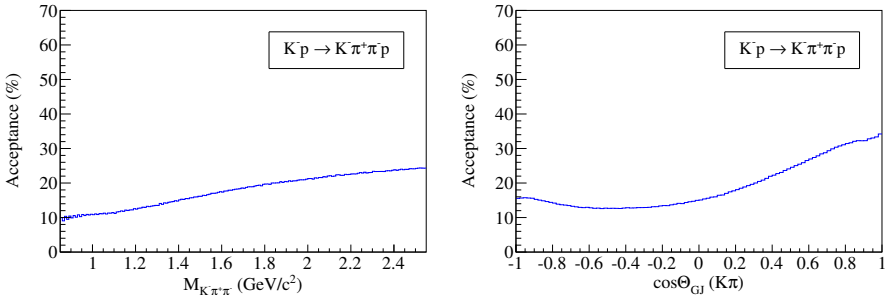

Figure 91: Acceptance for the diffractively produced $K^-\pi^+\pi^-$ final state (left) as a function of the $K\pi\pi$ invariant mass, and (right) as a function of the polar angle of the π^+K^- isobar in the Gottfried-Jackson frame.

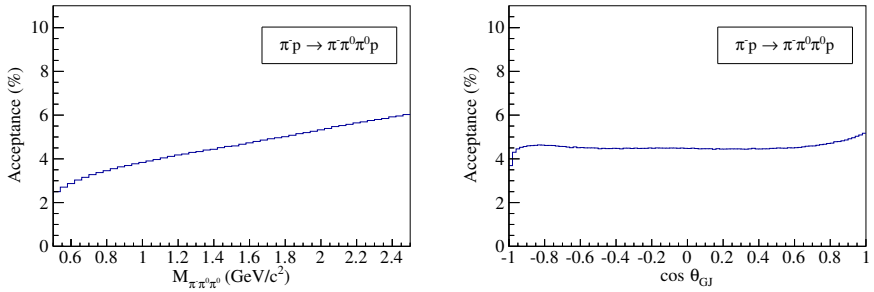

Figure 92: Acceptance for the diffractively produced $\pi^-\pi^0\pi^0$ final state (left) as a function of the 3π invariant mass and (right) as a function of the polar angle of the $\pi^0\pi^0$ isobar in the Gottfried-Jackson frame.

Compared to the charged-pion channel, the acceptance for the channel containing neutral pions is smaller and its dependence on the three-pion mass is more pronounced. The decrease of the acceptance is mainly due to the photon detection efficiency, which is lower than that for charged particles as photons may get absorbed in passive materials before reaching the calorimeters. The largest absorption is caused by the beam pipe of the RICH-1 detector (see Section 6.1), an effect which is mainly important for forward-going photons. Nevertheless, the detection of four photons smears the effect, so that the angular modulation of the acceptance remains weak and similar to that of the charged-pion case.

10.2. Performance of the hadron setup

The performances of the individual detectors and of the reconstruction software were presented in the previous sections. Here, the main characteristics of the setup are presented with examples from various physics processes.

10.2.1. Kinematic distributions

The selection of exclusive events with a primary vertex inside the target is a prerequisite for most analyses performed on the data with hadron beams. Exclusive events are selected by requiring energy conservation and transverse momentum balance between incoming and outgoing particles. Figure 93 shows the distributions of the difference between the energy of the outgoing particles and of the incoming beam particle, for the diffractive dissociation into three charged pions and for the Primakoff pion Compton scattering. The beam momentum station, which is used to determine the momentum of each incoming beam particle when operating the muon beam, is removed for hadron beams in order to reduce the amount of material in the beam. Therefore, the beam energy is set to the value determined by the beam line settings. In the diffractive process, the energy of the outgoing pions is combined with the recoil proton energy measured by the RPD. In the Primakoff reaction, the incident pion energy is shared between the scattered pion and the emitted photon, whereby the contribution of the target recoil remains negligible. The widths of the energy balance distributions shown in Fig. 93 are dominated by the momentum spread of the beam particles (see Section 3.1), with

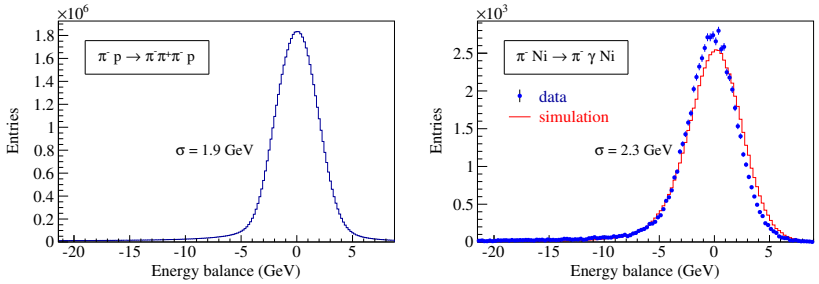

Figure 93: Energy balance between outgoing and incoming particles for (left) diffractive dissociation with three charged pions in the final state and (right) for Primakoff scattering.

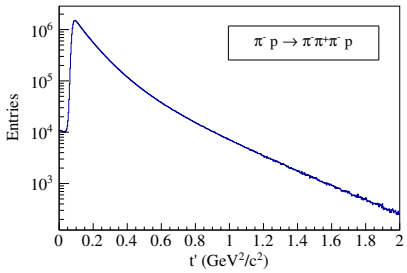

Figure 94: Squared four-momentum transfer for $\pi^-\pi^+\pi^-$ events produced by a pion beam impinging on a liquid hydrogen target, and selected by the DT0 trigger.

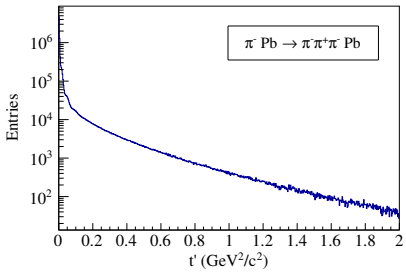

Figure 95: Squared four-momentum transfer for $\pi^-\pi^+\pi^-$ events produced by pions hitting a lead target, and selected by the multiplicity trigger.

a smaller contribution from the finite momentum resolution for charged particles and also from the finite energy resolution for photons in the case of the Primakoff reaction.

The physics processes studied in COMPASS can be identified via their characteristic dependence on the reduced squared four-momentum transfer t', which is calculated from the four-momenta of the incoming beam particle and the outgoing particles according to the equations given in Section 1. While Primakoff reactions proceeding through the exchange of quasi-real photons dominate the cross section at $t' < 0.001\,\mathrm{GeV}^2/c^2$, diffractive and central production reactions prevail at larger values of t'. Here we show measured t' distributions for the different physics triggers mentioned in Section 7.6.

Figure 94 shows the t' distribution recorded with the diffractive trigger DT0, determined from events with three charged pions in the final state. The cut at $t' \approx 0.07\,\mathrm{GeV}^2/c^2$ is due to the requirement of a signal in the RPD. The DT0 trigger thus enhances events with high t'. The small leakage of events with $t' < 0.07\,\mathrm{GeV}^2/c^2$ presumably originates from δ electrons or pions accidentally firing the RPD.

The multiplicity triggers LT1 and LT2 are used to also include events with lower values of t', since no recoil proton is required. The corresponding t' distribution measured with a pion beam and solid nuclear targets (Section 4.2), shown in Fig. 95, ex-

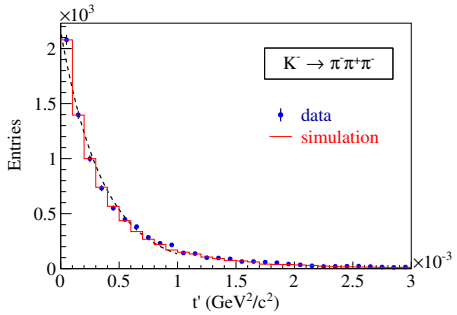

Figure 96: Squared four-momentum transfer of reconstructed beam kaons (data points) compared to the Monte Carlo simulation of purely electromagnetic interaction (solid lines). The dashed line is an exponential fit, used to determine the resolution.

hibits an exponential increase of the number of events towards low values of t'. In the first few bins also Primakoff events contribute, in addition to those generated by strong interaction.

A good resolution on the measurement of t' is important in order to distinguish between Primakoff and diffractive scattering. The resolution at very small values of t' is determined using the decay of beam kaons into two or three charged pions. For free-particle decays, t' is by definition zero, and the measured width of the t' distribution, shown in Fig. 96, gives a direct estimate of the resolution. A width of $3.6 \cdot 10^{-4}\,\mathrm{GeV}^2/c^2$ is obtained from the data, in good agreement with the resolution from Monte Carlo simulations. At higher values of t', the resolution can only be determined from Monte Carlo simulations. A value of $7 \cdot 10^{-3}\,\mathrm{GeV}^2/c^2$ is obtained for $0.1\,\mathrm{GeV}^2/c^2 < t' < 1.0\,\mathrm{GeV}^2/c^2$, from the simulation of diffractive production of three charged pions.

For the measurement of the pion polarisability, exclusive $\pi^-\gamma$ events are selected from the data sample collected with the calorimeter trigger (see Section 7.5). The left panel of Figure 97 shows the distribution of the four-momentum transfer $|Q| = \sqrt{t'}$, chosen here to emphasize its shape at small values. The peak at $|Q| \approx 0.02\,\mathrm{GeV}/c$ mainly contains quasi-real photoproduction events. The fact that the interaction is purely electromagnetic at very low values of t', which correspond to large impact parameters, becomes clear when comparing it to the right panel of Figure 97 that shows the corresponding distribution taken under the same conditions, but with a μ^- beam instead of a π^- beam. For the pion beam, the strong interaction dominates at $|Q|$ values above $0.05\,\mathrm{GeV}^2/c^2$, resulting in typical diffractive structures. The Monte Carlo simulation, superimposed as solid line in both panels, describes both cases very well.

10.2.2. Mass resolution

The mass resolution of the spectrometer is determined using known narrow states that are reconstructed in the spectrometer via their decay into neutral and/or charged particles. Here we show distributions for two-photon decays (π^0, η), for decays into final states with charged particles only (K^0_S, ϕ, Λ, Ξ), and for decays into final states containing both charged and neutral particles (η, ω, η', f_1).

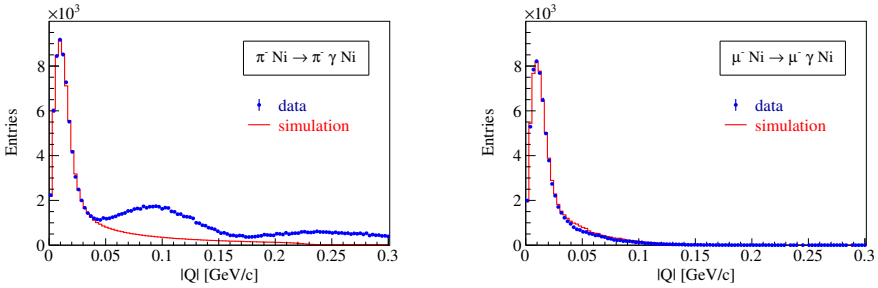

Figure 97: Momentum transfer distributions for exclusive (left) $\pi^-\gamma$ and (right) $\mu^-\gamma$ events. The data (dotted lines) are compared to the MC simulation (solid lines).

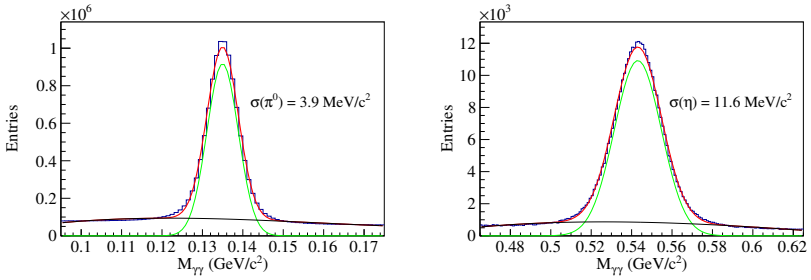

Figure 98: Two-photon invariant mass distribution as measured in ECAL2, in the (left) π^0 mass region and (right) η mass region. The solid curves are fits to the signal and to the background. The values of the resolution achieved are indicated in each plot.

The invariant mass distributions of photon pairs in the π^0 and η mass regions, as measured by ECAL1 and ECAL2, are shown in Fig. 98. The distributions are obtained from diffractive interactions of a 190 GeV negative hadron beam impinging on a liquid hydrogen target. Apart from the standard event selection mentioned in Section 10.2.1, only clusters with energies larger than 0.6 GeV in ECAL1 and 1.2 GeV in ECAL2 are selected. Energy resolution values of $7.8\,\mathrm{MeV}/c^2$ and $3.9\,\mathrm{MeV}/c^2$ are obtained for the two-photon π^0 peaks detected in ECAL1 and in ECAL2, respectively. The corresponding values for the η meson are $19.5\,\mathrm{MeV}/c^2$ and $11.7\,\mathrm{MeV}/c^2$.

Hadrons reconstructed from decay modes that contain only charged particles are shown in Fig. 99. In an inclusive selection, the following resolutions are obtained: $5.90\,\mathrm{MeV}/c^2$ for the K^0_S, $1.9\,\mathrm{MeV}/c^2$ for the $\phi(1020)$, $1.99\,\mathrm{MeV}/c^2$ for the Λ and $\bar{\Lambda}$ and $2.80\,\mathrm{MeV}/c^2$ for the $\Xi^{\pm}$.

Complex resonance decays with more than three particles in the final state are reconstructed e.g. by combining a π^0 or η in the $\gamma\gamma$ channel with a neutral pair of pions ($\pi^+\pi^-$) leaving the primary vertex. The left panel of Fig. 100 shows the invariant mass spectrum of the $\pi^-\pi^+\pi^0$ final state in the $\omega(782)$ mass region from central production reactions of a proton beam with the liquid hydrogen target. As shown in the right panel of Fig. 100, selecting the η instead of the π^0 gives access to the decays $\eta'(958) \to \pi^-\pi^+\eta$ and $f_1(1285) \to \pi^-\pi^+\eta$, which are reconstructed from diffractive

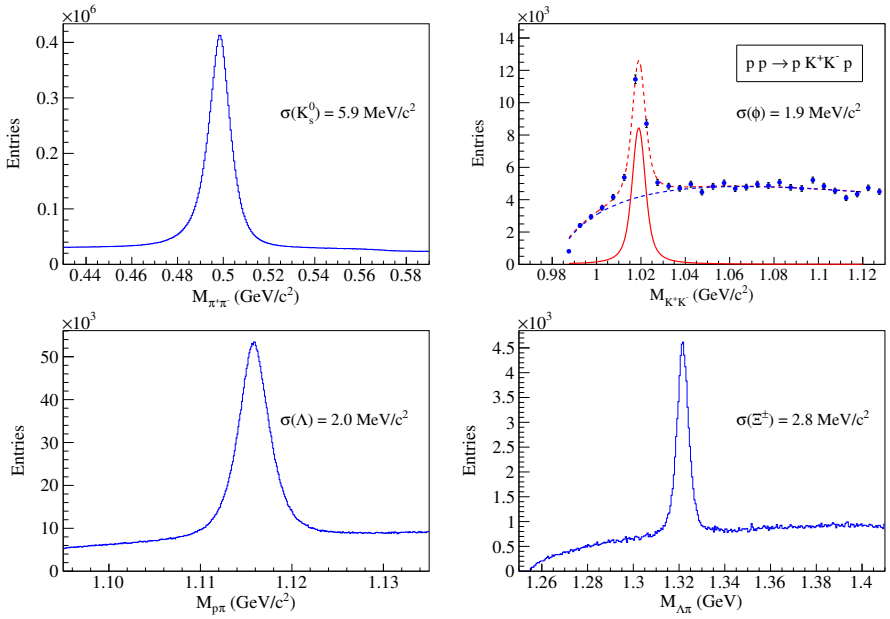

Figure 99: Reconstructed invariant masses for charged particles in the final state. The peaks shown are for (top left) $K^0_S(498)$, (top right) $\phi(1020)$, (bottom left) $\Lambda(1115)$, and (bottom right) $\Xi^{\pm}$. The K^0_S, Λ, and $\Xi^{\pm}$ particles are produced in inclusive reactions. The dashed curve in the $\phi(1020)$ plot is a fit to the background.

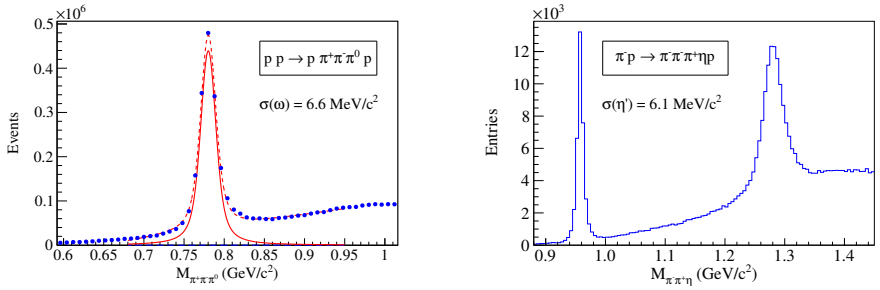

Figure 100: Invariant mass spectra for (left) $\pi^-\pi^+\pi^0$ and (right) $\pi^-\pi^+\eta$ systems. The full line in the left panel is a fit to the ω peak only; the dashed line includes also the background.

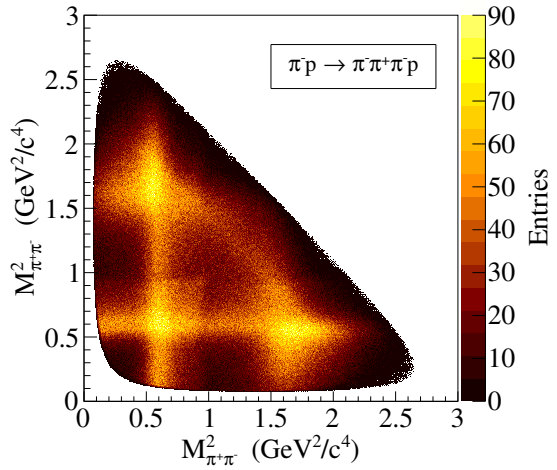

Figure 101: Dalitz plot for three diffractively produced charged pions after a cut of $\pm 130\,\mathrm{MeV}/c^2$ around the $\pi_2(1670)$ mass.

$\pi^- p \to \pi^-\pi^+\pi^- p\gamma\gamma$ events. Deconvoluting the natural width of the ω, a resolution of the spectrometer of $6.6\,\mathrm{MeV}/c^2$ is obtained. The natural width of the η' is negligible, so the width of the peak directly gives a resolution of $6.1\,\mathrm{MeV}/c^2$ in this mass range.

Three-body decays of short-lived resonances with correspondingly larger widths can be studied in Dalitz plots or by using the technique of PWA. A high-statistics Dalitz plot for the $\pi^-\pi^+\pi^-$ final state ($5 \cdot 10^7$ events) is depicted in Fig. 101, where the invariant mass of the 3π system was required to be within $\pm 130\,\mathrm{MeV}/c^2$ around the nominal mass of the $\pi_2(1670)$ resonance. The bands correspond to the decays $\pi_2(1670) \to \rho\pi$ and $\pi_2(1670) \to f_2(1270)\pi$.

11. Summary

In this paper, a detailed description of the COMPASS experimental setup as used for the physics programme with hadron beams is given. Operational since 2002, the

setup was designed for both hadron structure and hadron spectroscopy studies. It makes use of the various beams available at the CERN M2 beam line, namely positive and negative hadrons, positive and negative muons, and electrons. The apparatus operates with beams in the energy range of 100 to 200 GeV and is able to detect charged and neutral hadrons in the final state. Two large-aperture dipole magnets provide wide angular and momentum acceptances. While the major part of the setup remains essentially unchanged, its target region is reconfigurable as a function of the specific experimental programme.

For several years, the COMPASS setup was successfully used with muon beams and with a large-size polarised target for spin structure studies. After a week of exploratory data taking period in 2004, an important part of the COMPASS hadron programme was conducted in 2008 and 2009. Over the years, several new components were added to the setup, according to the requirements of the hadron physics programme and also to improve the overall performance of the apparatus.

Immediately upstream of the COMPASS setup, two CEDAR detectors were installed into the M2 beam line. Based on the Cherenkov effect, the CEDARs identify the hadron beam particle, separating kaons, pions and protons. A new target system, consisting of either a solid-state target holder or a liquid hydrogen target was built. A Recoil Proton Detector, surrounding the target, provides access to exclusive measurements. An accurate vertex resolution was achieved by adding nitrogen-cooled Silicon microstrip detectors upstream and downstream of the target.

Several new PixelGEM detectors were positioned along the setup for particle tracking at very small angles. Modified Micromegas detectors were used for tracking immediately downstream of the target in the presence of high hadron fluxes. Two additional large-size drift chamber detectors were also installed in order to improve the detection at large polar angles.

Both charged and neutral particle identifications were considerably improved. An important upgrade of the RICH-1 detector was carried out, resulting in higher efficiency and increased rate capability. The ECAL1 calorimeter was completed and added to the setup, while ECAL2 was modified to withstand the high flux in the case of hadron beams.

The main part of the trigger system was rebuilt for use with hadron beams. Several new trigger and veto elements such as recoil proton detector, multiplicity counter, and sandwich veto were added, thereby optimizing the system for diffractive scattering. A new digital calorimeter trigger was developed for selecting Primakoff reactions. The data acquisition system was further tuned in order to stand high trigger rates with low dead time. The detector control system was adapted to include the new detectors and upgraded with new monitoring features.

All new detectors were successfully included in the full software analysis chain. The tracking, reconstruction, simulation, and analysis tools were updated and adapted to the use with hadron beams. The acceptance of the apparatus covers large angular and momentum ranges and is nearly uniform for all kinematical variables. The overall characteristics of the setup illustrate its important potential for hadron spectroscopy studies. Invariant masses of up to 3 GeV$/c^2$ are covered with statistical accuracies significantly better than in previous experiments. The good energy resolutions achieved allow access to a large number of meson and baryon resonances. In summary, the

upgraded COMPASS setup is fully operational for use with the various hadron beams available at CERN.

Acknowledgements

We gratefully acknowledge the CERN laboratory and the CERN BE, EN, IT, TE and PH departments for providing constant and efficient support during the upgrade phase of our experimental setup and during data taking. We express our gratitude to the numerous engineers and technicians from our home institutions, who have contributed to the construction and later to the maintenance of our detectors and equipment. We are also grateful to A. Altingün for help in the preparation of the numerous figures.

We acknowledge support from MEYS Grants ME492 and LA242 (Czech Republic), CEA (France), Bundesministerium für Bildung und Forschung, DFG cluster of excellence "Origin and Structure of the Universe" and DFG Research Training Group Programme 1102 "Physics at Hadron Accelerators" (Germany), CERN-RFBR Grants 08-02-91009 and 12-02-91500, Israel Science Foundation, founded by the Israel Academy of Sciences and Humanities (Israel), INFN and MIUR (Italy), MEXT and JSPS Grants Nos. 18002006, 20540299 and 18540281, Daiko Foundation and Yamada Foundation (Japan), SAIL (CSR) (Government of India), NCN Grant DEC-2011/01/M/ST2/02350 (Poland), Fundação para a Ciência e Tecnologia, COMPETE and QREN, Grants CERN/-FP/109323/2009, CERN/FP/116376/2010 and CERN/FP/123600/2011 (Portugal) and from European Union FP7 (HadronPhysics3, Grant Agreement number 283286).

References

[1] COMPASS Collaboration, P. Abbon, et al., Nucl. Instr. and Meth. A 577 (2007) 455.

[2] COMPASS Collaboration, M. Alekseev, et al., Phys. Rev. Lett. 104 (2010) 241803.

[3] COMPASS Collaboration, C. Adolph, et al., Phys.Rev.Lett. 108 (2012) 192001.

[4] P. Abbon, et al., Nucl. Instr. and Meth. A 567 (2006) 114.

[5] H. Atherton, et al., Precise measurements of particle production by 400 GeV/c protons on beryllium targets, CERN Yellow Report, CERN 80-07 (1980).

[6] C. Bovet, et al., The CEDAR counters for particle identification in the SPS secondary beams, CERN Yellow Report, CERN 82-13 (1982).

[7] GAMS NA-12/2 Collaboration, D. Alde, et al., Nucl. Instr. and Meth. A 342 (1994) 389.

[8] T. Alimova, et al., IFVE-86-35 .

[9] J. Bernhard, Aufbau des inneren Rings eines Recoildetektors am COMPASS Experiment, p. 36-38, Master's thesis, Johannes-Gutenberg Universität Mainz (2007).

[10] T. Schlüter, et al., Nucl. Instr. and Meth. A 654 (2011) 219.

[11] M. J. French, et al., Nucl. Instr. and Meth. A 466 (2001) 359.

[12] MUSCADE(r), μS.C.A.D.A for Embedded System and PC, http://irfu.cea.fr/Sis/products/www/muscade/.

[13] S. Grabmüller, Cryogenic silicon detectors and analysis of primakoff contributions to the reaction π^- pb $\rightarrow \pi^-\pi^-\pi^+$ pb at COMPASS, Ph.D. thesis, Technische Universität München (2012).

[14] F. Sauli, Nucl. Instr. and Meth. A 386 (1997) 531.

[15] B. Ketzer, et al., Nucl. Instr. and Meth. A 535 (2004) 314.

[16] B. Ketzer, et al., A triple GEM detector with pixel readout for high-rate beam tracking in COMPASS, in: Nuclear Science Symposium Conference Record, 2007. NSS '07. IEEE, Vol. 1, IEEE, Piscataway, NJ, 2007, pp. 242–244.

[17] M. C. Altunbas, et al., Nucl. Instr. and Meth. A 490 (2002) 177.

[18] Xilinx programmable logic devices, Xilinx, San Jose, California, USA, http://www.xilinx.com/.

[19] M. Krämer, et al., First results of the PixelGEM central tracking system of COMPASS, in: Nuclear Science Symposium Conference Record, 2008. NSS '08. IEEE, IEEE, Piscataway, NJ, 2008, pp. 2920–2925.

[20] A. Austregesilo, et al., Nucl. Phys. B (Proc. Suppl.) 197 (2009) 113, 11th Topical Seminar on Innovative Particle and Radiation Detectors (IPRD08).

[21] F. M. Newcomer, et al., IEEE Trans. Nucl. Sci. 40 (1993) 630.

[22] F. Gonella, et al., The MAD, a full custom ASIC for the CMS barrel muon chambers front end electronics, CERN/LHCC 2001-034, 7th Workshop on Electronics for LHC Experiments, Stockholm, Sweden, 10-14 Sep 2001 (2001).

[23] H. Fischer, et al., Nucl. Instr. and Meth. A 461 (2001) 507.

[24] E. Albrecht, et al., Nucl. Instr. and Meth. A 553 (2005) 215, and references therein.

[25] E. Albrecht, et al., Nucl. Instr. and Meth. A 502 (2003) 266.

[26] E. Albrecht, et al., Nucl. Instr. and Meth. A 502 (2003) 236.

[27] J. C. Santiard, et al., GASSIPLEX: a low noise analog signal processor for readout of gaseous detectors, presented at the 6th Pisa Meeting on Advanced Detectors, La Biodola, Isola d'Elba, Italy (1994).

[28] P. Abbon, et al., Nucl. Instr. and Meth. A 567 (2006) 104.

[29] P. Abbon, et al., Nucl. Instr. and Meth. A 587 (2008) 371.

[30] P. Abbon, et al., Nucl. Instr. and Meth. A 616 (2010) 21.

[31] P. Abbon, et al., Nucl. Instr. and Meth. A 631 (2011) 26.

[32] F. Binon, et al., Nucl. Instr. and Meth. A 248 (1986) 86.

[33] BEATRICE Collaboration, M. Adamovich, et al., Nucl. Instrum. Meth. A379 (1996) 252.

[34] NA14 Collaboration, P. Astbury, et al., Phys. Lett. B152 (1985) 419.

[35] M. Anfreville, et al. CERN/CMS Note 2007-028.

[36] Continuum, Santa Clara CA 95051, USA, http://www.continuumlasers.com/.

[37] M. Kobayashi, et al., Nucl. Instr. and Meth. A 345 (1994) 210.

[38] A. Mann, et al., 15th IEEE-NPSS Real-Time Conference (2007) 1.

[39] C. Bernet, et al., Nucl. Instr. and Meth. A 550 (2005) 217.

[40] CYPRESS Semiconductor Corporation, CY7B923/33 HOTLink Transmitter/Receiver Data Sheet.

[41] H. Fischer, et al., IEEE Trans. Nucl. Sci. 49 (June 2002) 443.

[42] H. C. van der Bij, et al., IEEE Trans. Nucl. Sci. 44 (1997) 398.

[43] F. Carena, et al., ALICE DAQ and ECS user's guide, CERN-ALICE-INT-2005-015.

[44] J.-P. Baud, et al., CASTOR status and evolution, in: Computing in high energy and nuclear physics (CHEP03), La Jolla, CA, USA, 2003, arXiv:cs/0305047v1.

[45] MySQL AB, 753 20 Uppsala, Sweden, http://www.mysql.com.

[46] Oracle, Oracle Coropration, Santa Clara, California, USA, http://http://www.oracle.com.

[47] V. Jarý, Compass database upgrade, workshop doktorandské dny 2010, Master's thesis, Czech Technical University, Prague (2010).

[48] Apache software foundation, http server project, http://httpd.apache.org/.

[49] Nagios - the industry standard in open source monitoring, http://nagios.org/.

[50] P. Bordalo, et al., Control systems: An application to a high energy physics experiment (COMPASS), in: Proceedings of the 2012 IEEE International Conference on Automation Quality and Testing Robotics (AQTR), Cluj-Napoca, 24-27 May 2012, DOI: 10.1109/AQTR.2012.6237669.

[51] ETM professional control GmbH, Eisenstadt, Austria, http://www.pvss.com.

[52] JCOP Framework, http://j2eeps.cern.ch/wikis/display/EN/JCOP+ Framework.

[53] The OPC Foundation, http://www.opcfoundation.org.

[54] C. Gaspar, et al., Computer Physics Communications 140 (2001) 102.

[55] CAEN, Viareggio (LU), Italy, http://www.caen.it.

[56] DIP, http://en-dep.web.cern.ch/en-dep/Groups/ICE/Services/DIP/.

[57] ModBus, http://www.modbus.org.

[58] R. Brun, et al., Nucl. Instr. and Meth. A 389 (1997) 81, http://root.cern.ch.

[59] R. Brun, et al., Nucl. Instr. and Meth. A 502 (2003) 676.

[60] R. Frühwirth, Nucl. Instr. and Meth. A 262 (1987) 444.

[61] V. Blobel, et al., A new method for the high-precision alignment of track detectors, in: Proc. PHYSTAT2002, 2002, hep-ex/0208021.

[62] A. A. Lednev, Nucl. Instr. and Meth. A 366 (1995) 292.

[63] I. Uman, et al., Chinese Physics C 34 (2010) 1375.

[64] J. M. Friedrich, Chiral Dynamics in Pion-Photon Reactions, Habilitation thesis, Technische Universität München, Physik-Department E18, CERN-THESIS-2012-333 (2012).

[65] GEANT - detector description and simulation tool, CERN Program Library Long Writeup W5013, http://wwwasdoc.web.cern.ch/wwwasdoc /geant_html3/geantall.html.

Dear Editors,

Please find attached a corrected version of our paper. The corrected version includes all the typos mentioned by Referee 3, as well as some modifications, following his question about the CEDARs.

We also take the opportunity to correct two minor mistakes, in Sections 3.1 and 3.3.1, explained below.

Here are the answers to Referee 3:

Suggested corrections:

The vertical scale of Fig. 45 is not normalized to the measured value in the beginning ofthe period (of one week), as stated in the caption;

-> ANSWER: Figure 45 has been corrected.

The sentence in page 81, lines 1824-1825 is inappropriate since both the purity and the efficiency cannot be maximized at the same time.

-> ANSWER: The sentence on page 81 has been changed to avoid ambiguity.

Several typos were also found. Most of them are, however, expected to be corrected in the

type-setting process.

For examples,

page 15 line 250: "a a",
page 16 line 295: "protons",
page 24 line 491: "are are",
page 46 line 1017: "the types of PMTs",
page 49 line 1114: "i.e.",
page 72 line 1654: " a separate",
page 82 line 1848: "method method",
page 101 line 2288: ",or" -> "for"?
-> ANSWER: Typos have been corrected.

In addition, I have some minor questions/comments on the newly added detectors.

1) CEDAR

In Fig. 11, the background due most likely to pions is flat, whereas I naively expect some structure around 34.2 mbar/K as seen in Fig. 9, even if off-axis pions have already been preferentially selected by CEDAR1.

-> ANSWER: The background below the kaon peak could come from several sources, not only pions. The paragraph 3.3.3 that includes Fig.11 was modified accordingly.

2) PixelGEM

The boundaries between the sectors in the GEM electrode cause efficiency drops as shown in Fig. 29. In addition, the boundaries could make the track coordinate measurements nearby degraded, and possibly biased. In particular, those in the first GEM's electrode, facing the active volume, distort the drift field. Is it definitely necessary to divide the GEM electrodes into five segments for protection against discharges? The central sector in the third GEM's electrode, powered separately for reduced gain, could also affect the coordinate measurements near its boundary.

-> ANSWER: The sector boundaries indeed cause inefficiencies and local distortions of position information due to the bending of field lines, as the referee correctly remarks. In order to minimize the effect, the boundaries have a width of 150 um between conductive Cu surfaces and 350 um between holes. The central sector requires a separate line between two longitudinal sectors, increasing the gap between holes to 550 um. The reduced position resolution is taken into account in the recontruction by increasing the uncertainty for hits in the vicinity of sector boundaries. For the residual distribution shown in Fig. 27, these effects are included in the second Gaussian distribution with larger width, and are thus averaged over. The segmentation of the 10x10 cm2 active area into 5 sectors was mainly motivated by the goal to minimize the inefficient region in case of a permanent short circuit in one of the sectors. In addition, the reduced energy stored in a smaller sector helps to further suppress discharges [S. Bachmann et al., NIM A 479, 294 (2002)], although no dedicated studies have been performed for the PixelGEM detectors in the particular environment in COMPASS. During beam operation, no discharges were observed.

The text has been modified accordingly (see attached TeX file):

3) RICH1

Is it feasible to replace the photocathode of the multi-anode PMT with ultra or super bialkali for further improvement of photo-electron statistics? Micro-channel plate PMT could be another choice. It has excellent timing resolution and is rather insensitive to magnetic fields, though expensive. In addition, it has a simple response to single photons, in contrast with the double-peak pulse height spectrum characteristic of R7600.

-> ANSWER: The MAPMTs can, in principle, be replaced with ultra or super bialkali ones. Nevertheless, the number of detected photoelectrons is already very large and an improved statistics would have a marginal effect both concerning the measurement resolution and the efficiency of the reconstruction algorithm. At the same time, already in the present configuration, the probability that two photoelectrons impinging onto the same pad is not completely negligible; when two photoelectrons are detected by the same cell there is no statistical advantage: the digital electronics in use do not distinguish between 1 and 2 photoelectrons.

A higher quantum efficiency would increase this effect further and, as a consequence, a larger fraction of the detected photoelectrons would not be of use.

MCP-PMTs are, of course, an other option, even if (as suggested by the reviewer himself) very expensive. This detector type was not mature enough when the RICH-1 upgrade was implemented (2005-06).

As proven by us in the paper "P. Abbon et al., Nucl. Instr. and Meth. A 616 (2010) 21", the MAPMT double-peak pulse height is not a problem at the gain at which we operate the MAPMTs and using the read-out electronic chain in operation at COMPASS RICH-1.

Concluding, the MAPMT system performs very well and, even if other options can be adequate or even provide better performance, the present MAPMT-based photon detection system is fully satisfactory.

LaTeX Source Files

Click here to download LaTeX Source Files: phep-2014-247-nim-v2.tgz